Hybrid Method for Full-wave Simulations of Vegetation

by

Weihui Gu

A dissertation submitted in partial fulfillment
of the requirements for the degree of
Doctor of Philosophy
(Electrical and Computer Engineering)
in the University of Michigan
2022

Doctoral Committee:

Professor Leung Tsang, Chair
Professor Anthony Grbic
Professor Xianglei Huang
Professor Eric Michielssen

Weihui Gu

whgu@umich.edu

ORCID iD: 0000-0002-1189-9483

DEDICATION

To my family and all my friends.

ACKNOWLEDGMENTS

First, I would like to thank my advisor, Professor Leung Tsang. His passion and critical thinking on research has motivated me to approach problem from the first principle and challenge myself to make difference. I appreciate his support and guidance during my Ph.D. study. I would also thank Prof. Anthony Grbic, Prof. Eric Michielssen, and Prof. Xianglei Huang for serving my thesis committee and providing valuable suggestion to improve the thesis. I would also like to acknowledge the funding support received from the University of Michigan and the research projects from NASA Soil Moisture Active Passive mission. Special thanks go to Dr. Andreas Colliander and Dr. Simon Yueh from NASA JPL for their constructive feedback on my research. I would also like to thank all the professors and faculties from RadLab for providing the excellent electromagnetic courses and help me appreciate the beauty of Maxwell equations.

I appreciate the insightful thought and support from my colleague Shurun Tan, Jiyue Zhu, Tai Qiao, Huanting Huang, Ruoxing Gao, and JongWoo Jeong. Their helps have made the complicate equations looks much more friendly to me. The meaningful discussions with them have shaped my idea and motivate me to explore in research. My sincere thanks also go to the fellow RadLabors: Chenhui Qu, Zhanni Wu, Ruiying Cai, Han Guo, Weitian Sheng, Xiuzhang Cai, Menglou Rao, Tianlin Wang, Mostafa Zaky, Omar Abdelatty, Amanda Couch, Brian Raeker, Luke Szymanski, Cody Scarboroguh, Max Bright, Qunwen Lin and so on. I have gained invaluable encouragements and suggestions from them and will never forgot the teamwork we have done together to pass the homework dues and survive the exams. I will also cherish the fun time we had together. My great thanks also be given to my friends Yihao Tang, Renqi Xu, Jiayuan Xiao, Chenkai Su, Jiansi Tan, Yuliang Zhu, Xiaheng Huang, Tunan Wang, Minghao Chen, and so on. I appreciate all the support and helps I have received from all my friends which has made the journey be more enjoyable.

Finally, I give my deepest and most sincere gratitude to my parents, sister and all my beloved family. Their unconditional love and endless support have helped me made my way to here today. I especially like to share the great news with my grandfather who has inspired me to be curious to the world. It is not doubt that he will be the happiest one to know this in the sky.

Weihui Gu

University of Michigan, Ann Arbor

August 2022

TABLE OF CONTENTS

LIST OF FIGURES

LIST OF TABLES

ABSTRACT

In this dissertation, a hybrid method combing both the analytical and the numerical solutions is developed for full-wave simulations of vegetation. A realistic field setup is introduced to consider the plant structures and gaps within the vegetation canopy. The scattering of the whole vegetation field is then decomposed and solved in the following two steps. In the first step, the numerical solver is utilized to perform full-wave simulations of one single plant, from which the corresponding T-matrix is extracted based on the near-field using the Huygens principle and vector cylindrical wave (VCW) expansions. The full-wave based T-matrix characterizes the scattering of one single plant and captures the multiple scattering effects caused by the plant structure. In the second step, the T-matrix is combined with Foldy-Lax (FL) multiple scattering equations to consider the interactions among different plants within the vegetation field. The resulting closed-form equations are solved analytically using the VCW expansions and the translational addition theorem. The convergence and the accuracy of the hybrid method are verified with the High Frequency Structure Simulator (HFSS) by comparing the solutions of scatterings from four wheat plants. After that, the hybrid method is applied to investigate the frequency dependence of the vegetation effects by performing full-wave simulations of wheat fields at L-, S-, and C-band. A physical-iterative approach is implemented together with Message Passing Interface (MPI) parallel computing to facilitate the Monte Carlo simulations. The results obtained from the hybrid method are compared with those of the classical radiative transfer equation (RTE) model to illustrate the importance of full-wave simulations.

In the second part, the full-wave simulation of forest is realized using the hybrid method after two critical issues are successfully resolved. To overcome the challenge in calculating the tree T-matrix, the general relation between the T-matrix and the scattered field coefficient is first revealed

and a far-field based T-matrix extraction method applicable for plants of arbitrary size and structure is thus developed. Second, the memory challenge of hybrid method is eliminated by adopting the iterative solutions for solving the FL equations. The proposed methods are validated with FEKO by comparing the field solutions of scattering from three eight meters tall trees. The full-wave Monte Carlo simulations of forest are performed to investigate the tree effects on microwave propagation and the potential of using L-band signal to retrieve soil moisture over the forested area.

CHAPTER 1

Introduction

1.1 Background and Motivation

The research of full-wave simulation of vegetation is motivated by the microwave remote sensing of soil moisture. The soil moisture is the amount of the water stored in the soil, which makes up only about 0.001% of total water found on Earth. Although the volume of the soil moisture is small compared to the other components of the water cycle, it yet plays an important role in many hydrological and biological process. It not only controls the heat and mass transfer between the atmosphere and the Earth, but also determines the amount of water that contributes to the surface runoff versus the amount that infiltrates into soil (Fig. 1.1). For instance, a wet soil can prevent the Earth from being overheated through evaporation, and consequently affect the distribution of cloud and generation of precipitation. In addition, the soil moisture is the direct water source of the agriculture and natural vegetation, and thus monitoring of its variation can be very helpful for irrigation scheduling and corp yield forecasting. Moreover, the continuous observation of soil moisture in a large scale, over a long period of time, can provide a profound insight on the climate change as well. Consequently, knowledge of soil moisture distribution in global scale is of great importance in a variety of applications, including agricultural management, flood assessment, and climate change prediction, etc.

As a consequence of all these needs and importance of soil moisture, many approaches have been explored to measure the soil moisture, ranging from the in-situ measurement methods to

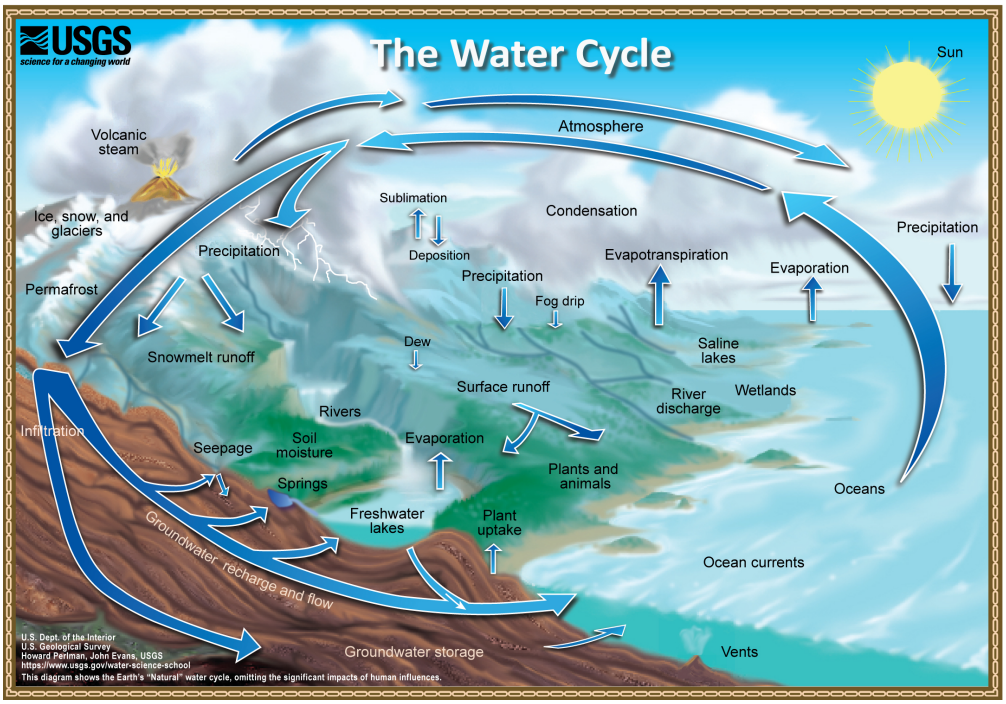

Figure 1.1: Water-cycle diagrams (copy from reference [1])

spaceborne satellite systems. The in-situ methods, including simple gravimetric technique and complex electronic instrument, are low cost and excellent for small scale monitoring. However, they are usually labor-intensive and has a very sparse spatial resolution in global scale and thus can hardly be applied to the global circulation ($<$ 50-100 km) and hydrologic models ($<$ 10-20 km) for climate prediction and weather forecast [2]. The alternative for obtaining soil moisture are the remote sensing technology such as the aerial photography, thermal infrared, and the microwave technique. Among them, the microwave is the only one that is transparent to cloud and rain, able to penetrate through vegetation, and capable of operating at night. All these unique properties make it possible to use microwave system to monitor the Earth independent of the time of day and under all weather conditions. Consequently, the spaceborne microwave remote sensing system has been the best option for obtaining global soil moisture distribution with the spatial and temporal frequency that can satisfy the science and application needs for hydrology.

The microwave remote sensing instruments can be classified into two classes, which are the active radar and the passive radiometer [3]. The radar, consisting of both transmitter and receiver,

retrieves the information by first sending out the microwave to land surface and then measuring the corresponding reflected signal. While the radiometer detects the soil moisture by measuring the emission form the earth, which only requires receiver and thus is cheaper than the radar system (Fig. 1.2). The most poplar active approach is the synthetic aperture radar (SAR) system as they can offer the best spatial resolution (˜1km). However, they are suffered with the low temporal frequency and is constrained by the coherent nature of signal which make it highly sensitive to the geometrical distribution of the scatterers including the leaves, branches, and trunks as well as the soil surface. The radiometers, on the other hand, provide an trade off between the spatial and temporal resolution. While the spatial resolution is coarser at the scale of 10s kilometers, it achieves a better temporal resolution (every 2-3 days) with a much wider swath. The passive system is also less sensitive to the surface roughness as the brightness temperature is measured incoherently. Moreover, the brightness temperature has a better sensitivity to soil moisture compared with backscattor measured from SAR. For example, the emissivity at L-band can vary form 0.5 for a wet soil to almost 1 for a very dry one at L-band [4].

Table 1.1: Spaceborne microwave satellite system.

Satellites	Agency	Passive/ Active	Frequency (GHz)	Spatial Resolution	Temporal Resolution	Time
SMOS	ESA	Passive	L:1.40	50 km	3-7 days	2009-2021
SMAP	NASA	Passive/ Active	L:1.41/1.26	40/3 km	7 days	2015-present
NISAR	NASA-India	Active	L:1.26, S:3.20	3-10 km	12 days	2023
CIMR	ESA	Passive	L:1.41, C:6.90	5-15 km	sub-daily	2028

Knowing the features of the microwave techniques, experimental systems and platforms for detecting the soil moisture has been proposed and implemented since the 1980s including tower-based, airborne, and spaceborne system (Table 1.1). In 2009, the first dedicated satellite mission Soil Moisture and Ocean Salinity (SMOS) was launched by European Space Agency (ESA) to provide high quality measurement of surface soil moisture based on a L-band radiometer with a 50km spatial resolution [5]. In 2015, the National Aeronautics and Space Administration (NASA)

carried out the Soil Moisture Active and Passive (SMAP) mission which combined both the L-band SAR and radiometer to achieve a better spatial resolution of 9 km [6]. The higher frequency data obtained from other missions have also been used to enhance the spatial resolution of soil moisture, such as the C-band observation of RADARSAT-2 satellite [7], and the C- and X-band channel of AMSR-E [8]. In the future, the NASA-ISRO SAR (NISAR) will utilize the L- and S-bands [9] and the Conical Imaging Microwave Radiometer (CIMR) satellite has multiple operating frequencies including L-, C-, X-, Ku-, and Ka-bands [10]. The increasing availability of spaceborne microwave system provides a great opportunity for further improving the L-band soil moisture retrieval by combining frequencies at different bands.

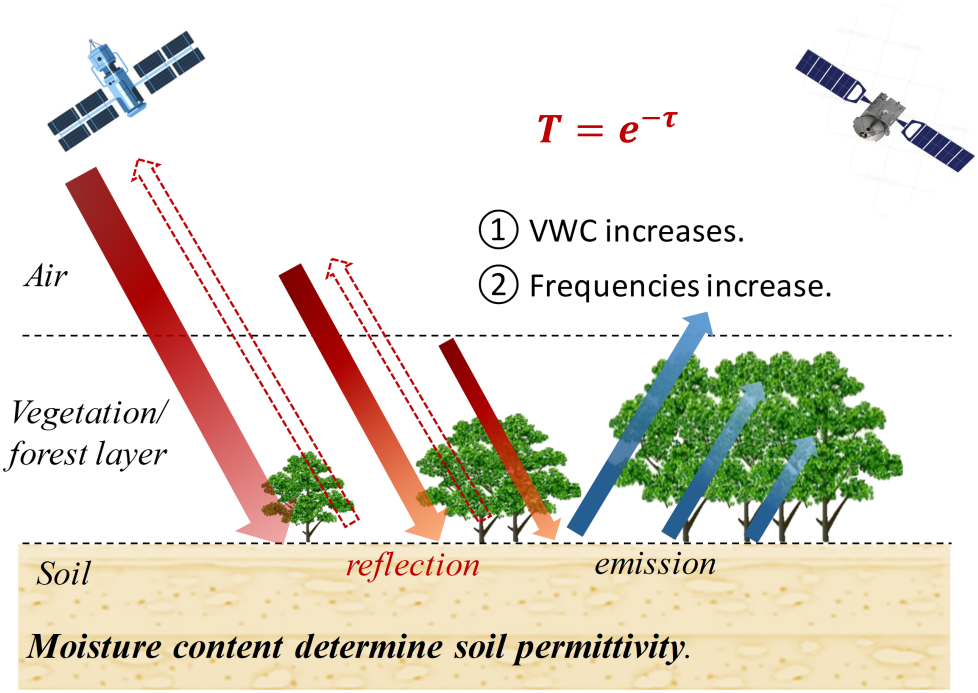

Figure 1.2: Microwave remote sensing of soil moisture.

The underline physics of retrieving the soil moisture from the microwave is that the dielectric permittivity of soil is predominately determined by its moisture content. An increase in the soil moisture results in a larger soil permittivity such that it causes a greater reflection of the incident wave in the active case. At the same time, it would reduce the emission due to the less transmission of energy into the soil for the passive case. In both scenarios, the signal should penetrate through

the vegetation layer before being received by the receiver, as most of the land surface are covered by the vegetation canopy. The microwave would be scattered, absorbed and depolarized by the vegetation when passing through the canopy. The absorption are mainly due to the water stored in the vegetation layer which is characterized by the vegetation water content (VWC). The VWC of crop are within $0.1 - 5kg/m^2$ and the VWC of forest range from $6.0kg/m^2$ to $18.0kg/m^2$ depending on the tree height and tree density. The vegetation effects on the microwave also depend on the physical and electrical properties of the scatterer, including the size, shape and the spatial distribution of the scatterer, as well as the attributes of the incident wave such as the frequency, polarization and the incident angle. Due to the complex nature of the random scattering, the successful soil moisture retrieval relies on an accurate modeling of the wave propagation in the vegetation. The focus of the dissertation is to construct a method that can perform full-wave simulation of vegetation to quantify the vegetation effects on the microwave.

1.2 Literature Review

A wide range of methods have been developed for modeling the vegetation effects on microwave in the last few decades. They can be generally classified into measurement based empirical models [11] and physical based theoretical models. The empirical model is built based on the measurement data obtained from a specific location, thus generally have a small domain of validity compared with those of theoretical approaches. The theoretical model can be further categorized into analytical and numerical models. The analytical approach can always be expressed in a simple closed-form by introducing limiting assumptions and thus has a higher efficiency compared with the numerical model. But their applications are constrained by the assumptions that have been made. The numerical models which require direct solutions of Maxwell equations are the most general and accurate methods but their capability is restricted by the tremendous computation cost.

The analytical approaches of random media that have been widely used for modelling wave propagation in vegetation, includes the effective medium approximation [12], the radiative transfer

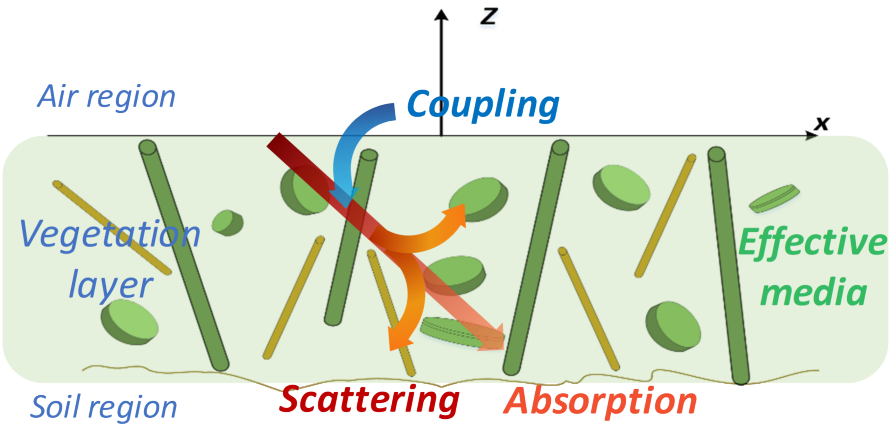

Figure 1.3: Radiative transfer model.

equation (RTE) [13], the distorted Born approximation (DBA) [14]. These models treat the vegetation canopy as a random media and assumes that the vegetation is statistically homogeneous in 3-dimensional space, so that it can be represented by a layered medium (Fig. 1.3) with an effective propagation constant or an effective permittivity leading to an effective attenuation rate and an effective mean field [15–17]. The common approximations used for calculating the effective propagation constant are the Maxwell Garnett mixing formula [15] or the Foldy's approximation [16]. The result of the effective medium model is that the microwave transmission through the vegetation field is characterized by $\exp(-\tau)$, where τ is the product of the effective attenuation rate and the thickness of the vegetation layer. The scattering of vegetation is then subsequently calculated by a single scattering of the mean field from the scatterer.

The RTE method, first proposed in [18] for describing light transmission through foggy atmosphere, has became a classical approach for modeling wave propagation in vegetation since 1980s. The RTE is derived heuristically based on the law of energy conservation without considering the interaction among scatterers. It has been investigated for decades and several efforts have been made to improve the accuracy of the RTE [19–23]. The phase matrix was used to consider the multiple scattering of intensities and the effects of the plant structure were considered through the coherent addition of branch scattering [19, 20]. Different solution methods, including the eigen-expansions, iterative method with and without backscattering enhancement [23], have also been

applied to improve the RTE. Despite these improvements made in the past, the RTE are still limited by several inherent approximations when applied to vegetation and forests: (i) The positions of the scatterers are assumed to be uniformly random. However such description is not consistent with the clustering of scatterers in a tree or plant and it also fails to model the gaps among plants and trees. (ii) The scatterers such as branches are assumed to be independent so that the scattered intensities are added incoherently. Thus the frequency dependence of scattering is that of the individual cylinder which leads to a strong frequency dependence for scattering by vegetation. The collective scattering and attenuation effects within a plant are ignored. (iii) Far field assumptions are made between the scatterers, and between the scatterers and the underlying soils. While the typical separation distance of crops grown in a vegetation field is a few centimeters, the far field distance requiring $R > D^2/\lambda$ is on the order of several meters, where D is the largest dimension of the scatterer.

With the advancement in digital computers, the standard numerical methods including finite element method (FEM), method of moments (MOM), and the finite-difference time-domain (FDTD) have been applied to perform full-wave simulations of vegetation [24–27]. However, the practical modelling capability of the numerical methods has been limited to several plants due to the enormous demand on CPU and memory. The few plants cannot be used to represent a vegetation field that consists of a large number of plants with scatterers randomly placed in clusters. Full-wave simulations of scatterings from vegetation field have been used to more rigorously account for the gap effects and the wave interactions among plants. In [28], the scatterings from a layer of 500 small cylinders were solved based on the Foldy-Lax (FL) multiple scattering equations and the body of revolution using MOM. The study shows that the transmission through a collection of vertical cylinders are several times larger than that predicted by the classical RTE model. This indicates the effective layered medium is inappropriate for representing a vegetation field with clustered scatterers. The scatterings by a collection of tall cylinders at L-band was treated in [29]. The height of the cylinder was 20 meters corresponding to 94 wavelengths at 1.41 GHz, which is used for microwave radiometry. [29] applied the infinite cylinder approximation to calculate the

T-matrix of a single cylinder that can be used to compute both the near fields and the far fields. Then, the T-matrix was applied to perform full-wave simulations of a forest represented by a layer of 194 randomly distributed cylinders. The results show that the transmission computed from the full-wave simulation is 1.9 times of that calculated from the analytical RTE model. However, the simulation methods reported in these two articles are limited to predict scattering from cylinders and not applicable for most vegetation types consisting of components with irregular shapes.

1.3 Thesis Objective and Overview

The objective of this dissertation is to develop a method that can perform full-wave simulations of vegetation and accurately model vegetation effects on the microwave. The full-wave simulation of a vegetation field is a large scale problem that can not be solved directly using the numerical method such as MOM, finite difference method, and finite element method due to the unaffordable computation cost and the tremendous memory demand. Neither can it be solved by the analytical methods due to their limitations on handling the scattering of complex structures. To tackle these challenges, a hybrid method combing both numerical and analytical solutions is developed by decomopsing the large scale problem in the following two steps. In the first step, the T-matrix of one single plant is extracted based on the full-wave solutions obtained from the numerical solver. This step leverages the modeling capability of the numerical method so that it is able to simulate plant with realistic structures of arbitrary shapes. The full-wave based T-matrix characterizes the scattering of one single plant and captures the multiple scattering effects caused by the plant structure. In the second step, the T-matrix is combined with the Foldy-Lax multiple scattering equations to consider the interactions among different plants. The resulting closed-form equations are solved analytically using the vector cylindrical wave (VCW) expansion and the translational addition theorem. The adoption of the analytical solutions significantly reduce computation demand for simulating a large vegetation field. By leveraging the advantages of both the numerical and analytical solutions, the full-wave simulation of a large vegetation field have been realized for

the first time using the proposed hybrid method.

In addition to the introduction and the conclusion chapters, the dissertation consists of three main chapters which are summarized as follow.

Chapter 2: A detailed discussion of the hybrid method is presented in this chapter. First, a near-field based T-matrix extraction method is developed based on the Huygens principle and VCW expansion of the Dyadic Green's function. Second, the formulation of the Foldy-Lax equations with T-matrix is presented together with the corresponding solutions obtained from VCW expansion and translational addition theorem. Finally, the convergence tests on the T-matrix are performed and the hybrid method is validated with HFSS by solving scattering from 4 wheat plants.

Chapter 3: The hybrid method is applied to perform full-wave simulations of wheat field at multiple frequencies including L-, S-, and C-bands to investigate the frequency dependence of the transmission. A physical-iterative method together with MPI parallel computing are implemented to facilitate the Monte Carlo simulations of wave propagation in the vegetation. The impacts of the plant structure and gaps on the microwave propagation are demonstrated by the comparing the transmission at different regions. The results obtained from the hybrid method are also compared with those of the classical RTE model to illustrate the importance of full-wave simulations.

Chapter 4: The hybrid method is applied to perform full-wave simulations of forest at L-band. The new challenges encountered by the hybrid method in simulating the forest is first discussed. To overcome the issue in calculating the tree T-matrix, the general relation between the T-matrix elements and the scattered field coefficients is revealed and a far-field based T-matrix extraction method is thus developed. The memory challenge in solving the Foldy-Lax equation is tackled by adopting the physical iterative solution. The new approaches are validated with FEKO by solving scattering from three 8 meters tall trees. Full-wave simulations of forest with different tree density and height are carried out to investigate the potential of retrieving soil moisture in the forest area using L-band microwave.

CHAPTER 2

Two-step Hybrid Method

The detailed discussions of the hybrid method for full-wave simulations of vegetation are presented in this chapter. First, we introduce a new geometry setup to account for the gap effects and the plant structures within the vegetation canopy. Based on the new geometrical configuration, the numerical solver of Ansys High Frequency Structure Simulator (HFSS) is used to simulate the scatterings of a single wheat plant, from which the corresponding T-matrix is extracted based on the near-field using the Huygens principle and the vector cylindrical waves (VCW) expansions of the Dyadic Green's function. The full-wave based T-matrix, capturing all the structural and clustering effects on scatterings, characterizes the response of one single plant. The multiple scatterings between different plants are considered through the Foldy-Lax (FL) equations using the extracted T-matrices in the second step. The resulting closed-from equations are then solved analytically using the VCW expansions and the translational addition theorem. The procedure of extracting the inner field using the wave transformation will also be discussed as it is crucial for calculating the microwave transmission. Finally, the proposed hybrid method is validated with HFSS by comparing the field solutions of scatterings from four wheat plants.

2.1 Introduction

During the last few decades, a variety of methods have been developed for modelling the wave propagation in the vegetation [13, 14, 19–23, 30, 31]. The most widely used model is the radiative transfer equation (RTE) model and the model of distorted Born approximation (DBA) where the

vegetation canopy is considered as a layer of randomly distributed scatterers. Specifically, the branches and leaves are modelled respectively by cylinders and disks. The random positions of the scatterer are assumed to be statistically homogeneous in space. Consequently, the vegetation canopy is approximated as a layered medium with an effective attenuation rate calculated based on the independent scattering approximation. While these approximations significantly reduce the modelling complexity of the RTE, the validity of these approximations for vegetation and forests have never been proven. A realistic examination shows that different vegetation types, in particular tree, frequently have unique structure governing the distribution of its stems and leaves. For example, a wheat plant is formed by a cluster of stems that are closely bound together, and they are grown in rows in a field with substantial gaps between plants (see Fig. 2.1).

The RTE approach has been investigated for decades. Improvements have been made on the solution methods and the calculation of the constituents such as absorption coefficients, phase matrices, etc. The effects of the plant structure have been considered through the coherent addition of the branch scattering in [19–22], where the geometry were modelled using the stochastic Lindenmayer system and the fractal tree. The results show that the coherent interactions play an important role in collective scatterings by scatterers. The row structures in the vegetation field are studied in [32–34]. A periodic slab is used to capture the row structure in a corn field and the multiple scattering within the row was considered using the phase matrix based on the far-field approximations [33]. However, the far-field assumption requiring that $R \geq 2D^2/\lambda$ is not valid for plants in a vegetation field, where R is the separation distance between scatterers, D is the largest dimension of scatterers and λ is the wavelength. For example, the wavelength is $\lambda = 25cm$ at L-band, and if the height of a plant is $D = 50cm$, then the far-field assumption requires $R \geq 2m$, whereas the typical separation distance for crops grown in a field is a few centimeters. Another improvement on the RTE is the dRET method [35], in which the vegetation layer are divided into cubic cells of different parameters. This makes it possible to calculate scatterings of the isolated vegetation structure by using ray tracing with RET. This approach works for scattering problem of high frequency, such as in millimeter waves, which the wavelengths are much smaller than the gap

size. In [36], a mean field solution for scattering from a collection of effective scatterers located in disjoint regions are derived. It results a nonuniform transmission rate that varies with position caused by the inhomogeneities of the vegetation. A numerical solution based on the method of moments (MOM) for grassland was reported in [24], however the solution was confined to a single grass plant due to the limitation on computation resources. None of these approaches treat the coherent interactions among the plants.

Full-wave simulations of scatterings from vegetation have been used to more rigorously account for the gap effects and the wave interactions among plants. In [28], the scatterings from a layer of 500 small cylinders were solved based on the Foldy-Lax (FL) multiple scattering equations and the body of revolution using MOM. The study shows that the transmission through a collection of vertical cylinders are several times larger than that predicted by the classical RTE model. This indicates the effective layered medium is inappropriate for representing a vegetation field with clustered scatterers. The scatterings by a collection of tall cylinders at L-band was treated in [29]. The height of the cylinder was 20 meters corresponding to 94 wavelengths at 1.41 GHz, which is used for microwave radiometry. [29] applied the infinite cylinder approximation to calculate the T-matrix of a single cylinder that can be used to compute both the near-field and the far-field. Then, the T-matrix was applied to perform full-wave simulations of a forest represented by a layer of 194 randomly distributed cylinders. The results show that the transmission computed from the full-wave simulation is 1.9 times of that calculated from the analytical RTE model. However, the simulation methods reported in these two articles are limited to predict scattering from cylinders and not applicable for most vegetation types consisting of components with irregular shapes.

In this chapter, a hybrid method combining both the numerical and analytical solutions is developed for full-wave simulations of the vegetation. A realistic geometrical setup is first introduced to consider the structures of the plant and the gaps within the vegetation. Then the large scale problem is decomposed and solved in two-step. First, the scattering of a single plant is characterized by the T-matrix which captures all the structural and clustering effects on scatterings. The T-matrix is extracted based on the full-wave solutions obtained from the HFSS using the Huygens

principle and the VCW expansion of the Dyadic Green's function. Second, the multiple scatterings between different plants are considered through the FL equations using the extracted T-matrices. The resulting closed-from equations are then solved analytically using the VCW expansion and the translation addition theorem. The hybrid method makes the full-wave simulation of a large vegetation field be possible by leveraging the advantage of both the numerical and analytical solutions. The detailed derivations are shown in the following section.

2.2 Vegetation Field Configuration

The hybrid method is based on a configuration that can model the plant structure and the gaps in the vegetation canopy. Here, we choose wheat as an example to illustrate the field concept which can be easily generalized to other vegetation types. As shown in Fig. 2.1, wheat plants are placed in rows and columns with gaps in a field. The row and column spacing are both random variables and are assumed to follow the Gaussian distribution with the mean value and standard deviation be estimated from the ground truth. In this chapter, a uniform spacing is used in the testing case to validate the accuracy of the method. The impacts of the variation of the gap spacing will be tested in the next chapter. Each wheat plant has its own structure and could be enclosed by a cylinder. This enable the hybrid method to decompose and solve the large scale problem in two steps, which each single plant is treated as a single scatterer in the first step and the interactions between different plants are considers in the second step. A realistic wheat plant that includes leaves, stems and spikes could be used in the hybrid method, as the numerical solver is employed to perform full-wave simulations of one single plant which allows us to model plant of arbitrary shapes. However, a simplified wheat plant model is used in order to make the results comparable with the RTE method, which will be presented in Chapter 3. Specifically, each wheat plant is modelled by a cluster of cylinders with randomly generated orientation angles. Based on this geometry setup, a two-step hybrid method for full-wave simulation of a vegetation field is developed.

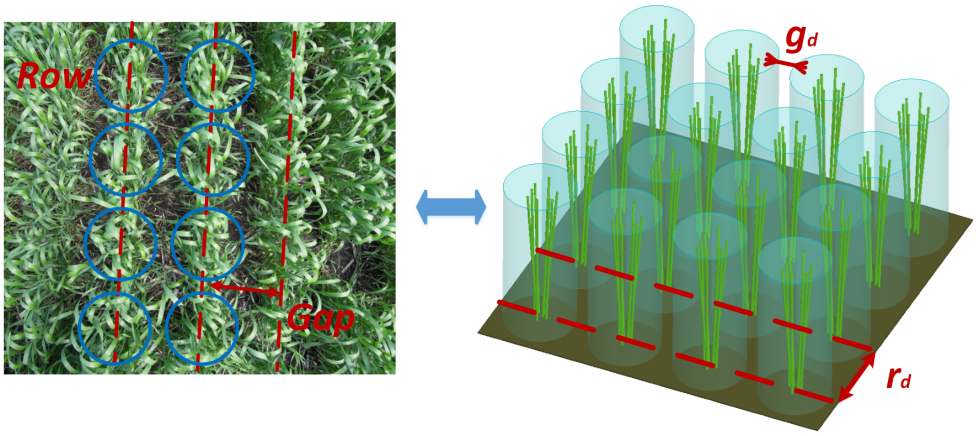

Figure 2.1: Real wheat field (left) and vegetation field configuration including gaps and plant structures for the hybrid method simulation (right).

2.3 Hybrid Method

2.3.1 Near-field Based T-matrix Extraction

The first step of the hybrid method is to extract the T-matrix of a single wheat plant. The purpose of the T-matrix is to relate the exciting fields to the scattered fields of an arbitrary object based on the analytic basis functions. To construct the T-matrix, an infinite cylindrical circumscribing surface is used to enclose the object of interest as shown in Fig. 2.2. The reasons are (i) there are no overlaps among plants (see Fig. 2.1), (ii) 3D VCW are used to represent the T-matrix, and (iii) the multiple scatterings between different plants are treated through VCW. The scattered fields due to a single plant outside the cylindrical surface can be characterized by using the T-matrix based on the 3D VCW expansion, which are detailed as follows.

Let the exciting fields be a plane wave given as

$$\bar{E}^{ex}(\bar{r}) = (\hat{v}_i E_{vi} + \hat{h}_i E_{hi}) \exp(i\bar{k}_i \cdot \bar{r}) \tag{2.1}$$

where $\hat{v}_i$ and $\hat{h}_i$, respectively, are the vertical and horizontal polarization vectors of the incident direction (θ_i, ϕ_i), E_{vi} and E_{hi} are their corresponding amplitudes, $\bar{k}_i = k(\hat{x}\sin\theta_i\cos\phi_i + \hat{y}\sin\theta_i\sin\phi_i + \hat{z}\cos\theta_i)$ is the incident propagation vector, and $\bar{r}$ is the position vector. From

model expansion theory, we know any fields in a cylindrical coordinate can be expressed as a linear combination of the VCW. With the VCW expansion, the exciting fields can be expressed as [37]

$$\bar{E}^{ex}(\bar{r}) = \sum_n \int_{-\infty}^{\infty} dk_z \Big[Rg\bar{M}_n(k_z, \bar{r}) a_n^{EM}(k_z) + Rg\bar{N}_n(k_z, \bar{r}) a_n^{EN}(k_z) \Big] \tag{2.2}$$

where $Rg\bar{M}_n(k_z, \bar{r})$ and $Rg\bar{N}_n(k_z, \bar{r})$ are the incoming VCW, $a_n^{EM}(k_z)$ and $a_n^{EN}(k_z)$ are the corresponding expansion coefficients of the exciting fields. The expressions of the incoming VCW are [37]

$$Rg\bar{M}_n(k_\rho, k_z, \bar{r}) = \Big[\hat{\rho} \frac{in}{\rho} J_n(k_\rho \rho) - \hat{\phi} k_\rho J_n'(k_\rho \rho) \Big] \exp(ik_z z) \exp(in\phi) \tag{2.3}$$

$$Rg\bar{N}_n(k_\rho, k_z, \bar{r}) = \Big[\hat{\rho} \frac{ik_\rho k_z}{k} J_n'(k_\rho \rho) - \hat{\phi} \frac{nk_z}{k\rho} J_n(k_\rho \rho) + \hat{z} \frac{k_\rho^2}{k} J_n(k_\rho \rho) \Big] \exp(ik_z z) \exp(in\phi) \tag{2.4}$$

where n is the order of harmonic in ϕ direction, $k_\rho = \sqrt{k^2 - k_z^2}$ is propagation constant in ρ direction, $\bar{r} = \rho\hat{\rho} + z\hat{z}$ is the position vector in cylindrical coordinate, J_n is the bessel function and J_n' is the first order derivative of J_n. The VCW expansion coefficients of a plane wave are known as [37]

$$\begin{aligned} a_n^{EM}(k_z) &= \frac{i^{n+1} \exp(-in\phi_i)}{k_{i\rho}} E_{hi} \delta(k_z - k_{iz}) \\ a_n^{EN}(k_z) &= -\frac{i^n \exp(-in\phi_i)}{k_{i\rho}} E_{vi} \delta(k_z - k_{iz}) \end{aligned} \tag{2.5}$$

where k_{iz} is the z component of $\bar{k}_i$. Note that in a general multiple scattering situation, we use the general expression of the exciting fields rather than that of an incident plane wave.

According to the Huygens principle [37], the scattered fields outside the circumscribing cylindrical surface can be calculated from

$$\bar{E}^s(\bar{r}) = \int_{S'} dS' \Big\{ ik\eta \overline{\overline{G}}(\bar{r}, \bar{r}') \cdot \big[\hat{n}' \times \bar{H}(\bar{r}') \big] + \nabla \times \overline{\overline{G}}(\bar{r}, \bar{r}') \cdot \big[\hat{n}' \times \bar{E}(\bar{r}') \big] \Big\} \tag{2.6}$$

where $\overline{\overline{G}}(\bar{r}, \bar{r}')$ is the Dyadic Green's function, S' are the surfaces of a cylinder enclosing the whole plant which include the side, top and bottom surfaces as shown in Fig. 2.2. $\bar{H}$ and $\bar{E}$, respectively,

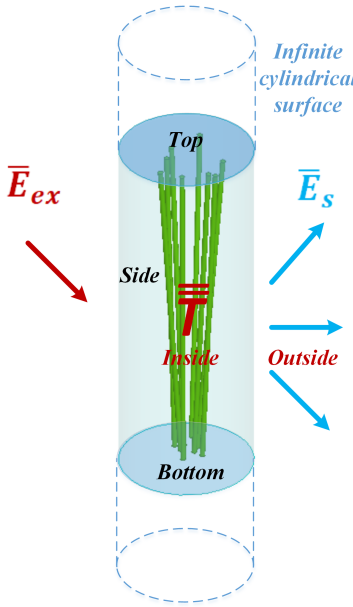

Figure 2.2: A single wheat plant is enclosed by an infinite cylindrical circumscribing surface, the scattered fields outside the surfaces are related to the exciting fields through the T-matrix of the wheat plant

are the magnetic and electric fields on S'. The VCW expansion of the Dyadic Green's function for $\rho > \rho'$ are [37]

$$\bar{\bar{G}}(\bar{r},\bar{r}') = \frac{i}{8\pi}\sum_n (-1)^n \int_{-\infty}^{\infty} dk_z \frac{1}{k_\rho^2}\left[\bar{M}_n\left(k_z,\bar{r}\right) Rg\bar{M}_{-n}\left(-k_z,\bar{r}'\right) + \bar{N}_n\left(k_z,\bar{r}\right) Rg\bar{N}_{-n}\left(-k_z,\bar{r}'\right)\right] \tag{2.7}$$

$$\nabla\times\bar{\bar{G}}(\bar{r},\bar{r}') = \frac{ik}{8\pi}\sum_n (-1)^n \int_{-\infty}^{\infty} dk_z \frac{1}{k_\rho^2}\left[\bar{N}_n(k_z,\bar{r}) Rg\bar{M}_{-n}\left(-k_z,\bar{r}'\right) + \bar{M}_n\left(k_z,\bar{r}\right) Rg\bar{N}_{-n}(-k_z,\bar{r}')\right] \tag{2.8}$$

where $\bar{M}_n(k_z,\bar{r})$ and $\bar{N}_n(k_z,\bar{r})$ are the outgoing VCW, and their expressions are obtained, respectively, by replacing the bessel function J_n in (2.3) and (2.4) with the Hankel function of first kind $H_n^{(1)}$. Substitution of (2.7), (2.8) into (2.6), the scattered fields outside the cylindrical surface can be written in the model expansion form as

$$\bar{E}^s\left(\bar{r}\right) = \sum_n \int_{-\infty}^{\infty} dk_z \left[\bar{M}_n(k_z,\bar{r}) a_n^{SM}(k_z) + \bar{N}_n(k_z,\bar{r}) a_n^{SN}(k_z)\right] \tag{2.9}$$

where $a_n^{SM}(k_z)$ and $a_n^{SN}(k_z)$ are the expansion coefficients of the scattered fields, and their ex-

pressions are in (2.12) and (2.13). Based on the VCW expansion coefficients of the exciting and scattered fields given in (2.2) and (2.9), the T-matrix is defined as

$$a_n^{S\beta}(k_z) = \sum_{n'} \int_{-\infty}^{\infty} dk_z' \left[T_{nn'}^{(\beta,M)}\left(k_z, k_z'\right) a_{n'}^{EM}\left(k_z'\right) + T_{nn',p}^{(\beta,N)}\left(k_z, k_z'\right) a_{n'}^{EN}\left(k_z'\right) \right] \tag{2.10}$$

where $\beta = M, N$ corresponds to the two polarizations of VCW. The same notations are used in the rest of the dissertation. The T-matrix is a general description of the scattered fields outside the enclosing cylindrical surface.

The VCW basis functions have two variables, n and k_z, which both range form $-\infty$ to $+\infty$ in theory. In practise, they are truncated at a maximum value that makes the scattered fields converged, which respectively are $\pm N_n$ and $\pm K_z^{\max}$. The continuous integration over k_z is replaced by a discrete summation of N_m samplings, $\int dk_z \approx \sum_m k_{zm} \Delta k_z$. The double summation over $n \in [-N_n, N_n]$ and $m \in [1, N_m]$ can be replaced by a combined index $(n, m) = l$, then $l = 1, 2, ..., L$, with $L = (2N_n + 1)N_m$. If we also count the two polarizations $\bar{M}_n$ and $\bar{N}_n$, then the combined index is $\alpha = 1, 2, ..., 2L$ with a total of $2L$ VCW basis functions. If we put the exciting and the scattered field coefficients, respectively, into a column vector, the matrix form of (2.10) is

$$\bar{a}_S\left(k_i\right) = \overline{\overline{T}} \bar{a}_E\left(k_i\right) \tag{2.11}$$

where $\bar{a}_E(k_i)$ and $\bar{a}_S(k_i)$ are, respectively, the exciting and the scattered field coefficient vector of size $2L \times 1$, and

$$\overline{\overline{T}} = \begin{bmatrix} T_{MM} & T_{MN} \\ T_{NM} & T_{NN} \end{bmatrix}$$

is of dimension $2L \times 2L$. To determine the $(2L)^2$ elements in the T-matrix, we perform full-wave simulations of a single plant using the HFSS with $2L$ different plane waves. For each incident plane wave, we calculate one pair of $\bar{a}_E(k_i)$ and $\bar{a}_S(k_i)$. Then by matrix inversion, $(2L)^2$ elements of T-matrix are determined.

For one incident plane wave, the scattered fields on the enclosing cylinder surfaces S' (See

Fig. 2.2) due to one single plant can be solved from HFSS. As described earlier, the scattered field coefficients then can be calculated using the Huygens principle and the VCW expansion of Dyadic Green's function through

$$a_n^{SM}(k_z) = \frac{(-1)^n ik}{8\pi k_\rho^2} \int_{S'} dS' \Big\{ i\eta Rg\bar{M}_{-n}(-k_z, \bar{r}') \cdot [\hat{n}' \times \bar{H}(\bar{r}')]_{HFSS} + Rg\bar{N}_{-n}(-k_z, \bar{r}') \cdot [\hat{n}' \times \bar{E}(\bar{r}')]_{HFSS} \Big\} \quad (2.12)$$

$$a_n^{SN}(k_z) = \frac{(-1)^n ik}{8\pi k_\rho^2} \int_{S'} dS' \Big\{ i\eta Rg\bar{N}_{-n}(-k_z, \bar{r}') \cdot [\hat{n}' \times \bar{H}(\bar{r}')]_{HFSS} + Rg\bar{M}_{-n}(-k_z, \bar{r}') \cdot [\hat{n}' \times \bar{E}(\bar{r}')]_{HFSS} \Big\} \quad (2.13)$$

where $[\cdot]_{HFSS}$ means the surface fields that are computed from HFSS. This gives the VCW coefficient vector of the scattered fields

$$\bar{a}_S(k_i) = \left[a_1^{SM}, \cdots, a_L^{SM}, a_1^{SN}, \cdots, a_L^{SN} \right]^T. \quad (2.14)$$

With the VCW expansion of the incident plane wave given in (2.5), the VCW coefficient vector of the exciting fields is

$$\bar{a}_E(k_i) = \left[a_1^{EM}, \cdots, a_L^{EM}, a_1^{EN}, \cdots, a_L^{EN} \right]^T. \quad (2.15)$$

In the above, a pair of $\bar{a}_E(k_i)$ and $\bar{a}_S(k_i)$ are computed for a single incident plane wave. The procedure is repeated $2L$ times for 2 different polarized plane waves from L different incident angles. With the $2L$ pairs of the calculated scattered and exciting field coefficients, the scattering and the exciting coefficient matrices are formed

$$\overline{\overline{A}}_\gamma = \left[\bar{a}_\gamma(k_1), \cdots, \bar{a}_\gamma(k_{2L}) \right] \quad (2.16)$$

where $\gamma = E, S$ corresponds to the exciting and the scattered field respectively. As each pair of $\bar{a}_E(k_i)$ and $\bar{a}_S(k_i)$ satisfy (2.11), we have $\overline{\overline{A}}_S = \overline{\overline{T}}\,\overline{\overline{A}}_E$. Then the T-matrix is obtained by

$$\overline{\overline{T}} = \overline{\overline{A}}_S \overline{\overline{A}}_E^{-1}. \tag{2.17}$$

In the first step of the hybrid method, the T-matrix is calculated based on the numerical full-wave solutions, which are applicable for a plant with arbitrary shape. The coherent multiple scattering effects within a single plant are captured by the T-matrix. The multiple scatterings between different plants are then considered in the second step using the calculated T-matrix and the FL equations.

2.3.2 Foldy-Lax Multiple Scattering Equations

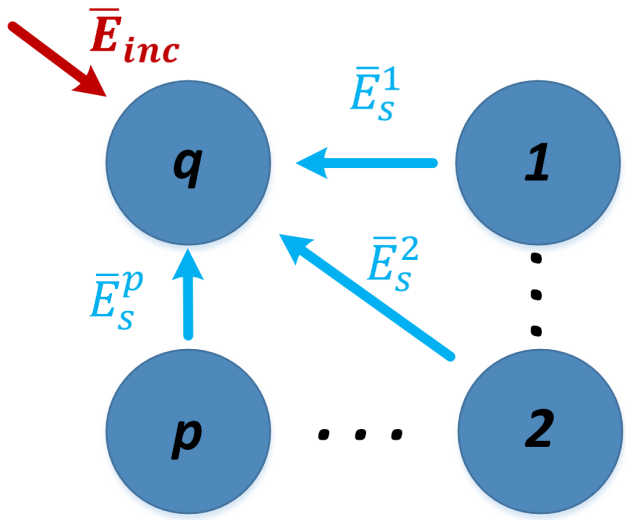

Figure 2.3: Illustration of Foldy-Lax multiple scattering equations.

For multiple scattering problem as shown in Fig. 2.3, the final exciting fields acting on one scatterer are the sum of incident fields and the scattered fields from all other scatterers except itself. This leads to the FL multiple scattering equations

$$\bar{E}_q^{ex}(\bar{r}) = \bar{E}^{inc}(\bar{r}) + \sum_{p=1, p\neq q}^{N} \bar{E}_{qp}^{s}(\bar{r}) \tag{2.18}$$

where N is the number of scatterers, $\bar{E}^{inc}$ is the incident fields, $\bar{E}^{ex}_q$ is the final exciting fields of scatterer q, and $\bar{E}^{s}_{qp}$ is the scattered fields from scatterer p to q. In (2.18), the summation of p is over all scatterers except itself, where $p = 1, 2, ..., N$, with $p \neq q$. In cylindrical coordinate system, the center location of the qth scatterer is $\bar{r}_q = \bar{\rho}_q + z_q\hat{z}$, where z_q is a convenient location of the scatterer. It can be used when the plants are of different heights. In this paper, the plant are of the same height. Let the qth scatterer be enclosed by a infinite cylinder centered at $\bar{r}_q$, then $\bar{E}^{ex}_q$ is expanded using VCW as

$$\bar{E}^{ex}_q(\bar{r}) = \sum_m \int dk_z \Big[Rg\bar{M}_m(k_z, \overline{rr_q}) a^{EM}_{m,q}(k_z) + Rg\bar{N}_m(k_z, \overline{rr_q}) a^{EN}_{m,q}(k_z) \Big] \tag{2.19}$$

where $a^{E\beta}_{m,q}(k_z)$ are the unknown final exciting field coefficients, the VCW are centered at $\bar{r}_q$, and $\overline{rr_q} = \bar{r} - \bar{r_q}$. To solve (2.18), we next expand $\bar{E}^{inc}$ and $\bar{E}^{s}_{qp}$ using VCW with center at $\bar{r}_q$. The expansion of the incident fields is

$$\bar{E}^{inc}_q(\bar{r}) = \exp(i\bar{k}_i \cdot \bar{r}_q) \sum_m \int dk_z \delta(k_z - k_{iz}) \frac{\exp(-im\phi_i)}{k_{i\rho}} i^m \times \Big[iE_{hi} Rg\bar{M}_m(k_{i\rho}, k_{iz}, \overline{rr_q}) - E_{vi} Rg\bar{N}_m(k_{i\rho}, k_{iz}, \overline{rr_q}) \Big] \tag{2.20}$$

where a phase shift term $\exp(i\bar{k}_i \cdot \bar{r}_q)$ results when we put the center of the VCW to $\bar{r}_q$. The dirac delta function $\delta(k_z - k_{iz})$ indicates that the incident wave is with $k_z = k_{iz}$ in the integration $\int dk_z$. Since the scattered fields from p to q originate from scatterer p, the outgoing VCW are initially expressed with origin at $\bar{r}_p$ as

$$\bar{E}^{s}_{qp}(\bar{r}) = \sum_n \int_{-\infty}^{\infty} dk_z \Big[\bar{M}_n(k_z, \overline{rr_p}) a^{SM}_{n,p}(k_z) + \bar{N}_n(k_z, \overline{rr_p}) a^{SN}_{n,p}(k_z) \Big] \tag{2.21}$$

where $a^{S\beta}_{n,p}(k_z)$ are the final scattered field coefficients of scatterer p. To balance the term in (2.18), we need to transform the outgoing VCW in (2.21) into the the incoming VCW centered at $\bar{r}_q$ by

using the translational addition theorem [17]

$$\bar{\beta}_n(k_z, \overline{rr_p}) = \sum_m Rg\bar{\beta}_m(k_z, \overline{rr_q}) H^{(1)}_{m-n}\left(k_\rho \left|\overline{\rho_p\rho_q}\right|\right) \exp(-i(m-n)\phi_{\overline{\rho_p\rho_q}}) \exp(-ik_z z_{pq}) \quad (2.22)$$

where $\overline{\rho_p\rho_q} = \bar{\rho}_p - \bar{\rho}_q$, $\phi_{\overline{\rho_p\rho_q}} = tan^{-1}[(y_p - y_q)/(x_p - x_q)]$ is the angle that $\overline{\rho_p\rho_q}$ makes with the x axis, and $z_{pq} = z_p - z_q$. The detail derivation of (2.22) can be found in the Appendix 2.A. By combining (2.21) and (2.22), we get

$$\bar{E}^s_{qp}(\bar{r}) = \sum_{\beta=M,N} \sum_n \int_{-\infty}^{\infty} dk_z \sum_m \exp(-i(m-n)\phi_{\overline{\rho_p\rho_q}}) \times Rg\bar{\beta}_m\left(k_z, \overline{rr_p}\right) H^{(1)}_{m-n}(k_\rho \left|\overline{\rho_p\rho_q}\right|) \exp(-ik_z z_{pq}) a^{S\beta}_{n,p}(k_z). \quad (2.23)$$

After substituting (2.19), (2.20), and (2.23) into (2.18), we have all the terms in the FL equations expanded with the incoming VCW center at $\bar{r}_q$. Then (2.18) is simplified by balancing the coefficient of VCW to

$$a^{E\beta}_{m,q}(k_z) = \exp(i\bar{k}_i \cdot \bar{r}_q) \frac{i^m \exp(-im\phi_i)}{k_{i\rho}} I_\beta \delta(k_z - k_{iz}) + \sum_{p=1, p\neq q} \sum_n \exp(-i(m-n)\phi_{\overline{\rho_p\rho_q}}) H^{(1)}_{m-n}(k_\rho \left|\overline{\rho_p\rho_q}\right|) \exp\left(-ik_z z_{pq}\right) a^{S\beta}_{n,p}(k_z) \quad (2.24)$$

where $I_\beta = iE_{hi}$ for $\beta = M$, and $I_\beta = -E_{vi}$ for $\beta = N$. The multiple scattering equations (2.24) relate the exciting field coefficients $a^{E\beta}_{m,q}(k_z)$ and the scattering field coefficients $a^{S\beta}_{n,p}(k_z)$ among the scatterers, which can be further simplified using the T-matrix. By substituting (2.10) into (2.24), the equations with $a^{E\beta}_m(k_z)$ as the only unknowns are obtained

$$a^{E\beta}_{m,q}(k_z) = \exp(i\bar{k}_i \cdot \bar{r}_q) \frac{i^m \exp(-im\phi_i)}{k_{i\rho}} I_\beta \delta(k_z - k_{iz}) + \sum_{p=1, p\neq q} \sum_n \exp(-i(m-n)\phi_{\overline{\rho_p\rho_q}}) \times H^{(1)}_{m-n}(k_\rho \left|\overline{\rho_p\rho_q}\right|) \exp\left(-ik_z z_{pq}\right) \sum_{n'} \sum_{\beta'} \int dk'_z T^{(\beta,\beta')}_{nn',p}(k_z, k'_z) a^{E\beta'}_{n',p}(k'_z) \quad (2.25)$$

where $q = 1, 2, ..., N$. This is the excitation field formulation of the FLE. The FLE can also be formulated using the scattered field and the derivation can be found in Appendix 2.B. Equation (2.25) can written in matrix form as $\bar{a}_E = \bar{f} + \overline{\overline{K}}\bar{a}_E$ using the transformation described in the Sec. 2.3.1. The final exciting field coefficients then can be solved from $\bar{a}_E = (\overline{\overline{I}} - \overline{\overline{K}})^{-1}\bar{f}$. The final scattered field coefficients $\bar{a}_S$ can be obtained by substituting $\bar{a}_E$ into (2.10). After that the scattered fields of the whole vegetation field can be obtained through the summation of scattering from each individual plant

$$\bar{E}^s(\bar{r}) = \sum_{p=1}^{N}\sum_{n}\int_{-\infty}^{\infty} dk_z \Big[\bar{M}_n(k_z, \overline{rr_p})\, a_{n,p}^{SM}(k_z) + \bar{N}_n(k_z, \overline{rr_p})\, a_{n,p}^{SN}(k_z)\Big]. \tag{2.26}$$

As mentioned before, the VCW expansion of Dyadic's Green's function is for $\rho > \rho'$, so (2.9) is only valid when observation point $\bar{r}$ is outside the enclosing cylindrical surface. If $\bar{r}$ in (2.26) is inside the circumscribing cylinder of plant p, then the scattered fields due to itself should be extracted in the next step.

2.3.3 Inner-field Extraction

Let $\bar{a}_E^{pl}$ be a column coefficient vector representing a linear combination of exciting plane waves

$$\bar{a}_E^{pl}(k_i) = \Big[a_E^{pl}(k_1),\, \ldots,\, a_E^{pl}(k_{2L})\Big]^T \tag{2.27}$$

where $a_E^{pl}(k_i)$ is the coefficient of the ith plane wave. We can obtain the corresponding VCW expansion through

$$\bar{a}_E = \overline{\overline{A}}_E \bar{a}_E^{pl}(k_i) \tag{2.28}$$

where $\overline{\overline{A}}_E$ is the coefficient matrix defined in (2.16). In other words, (2.28) is the transformation between plane wave and VCW. The final exciting field coefficients of plant q solved from the FL multiple scattering equations is $\bar{a}_E^q$, which is the VCW expansion of $\bar{E}_q^{ex}$. Using (2.28) the plane

wave expansion of $\bar{E}_q^{ex}$ can be calculated from

$$\bar{a}_E^{q,pl} = \overline{\overline{A}}_E^{-1} \bar{a}_E^q. \tag{2.29}$$

As the full-wave simulations of a single wheat plant illuminated by plane waves from different incident angles have been done using the HFSS in step 1, the final scattered fields due to plant p inside its enclosing cylinder can be obtained based on the superposition principle through

$$\bar{E}_{q,in}^s(\bar{r}) = \sum_{i=1} a_E^{q,pl}(k_i) \bar{E}_q^s(k_i) \tag{2.30}$$

where $\bar{E}_q^s(k_i)$ is the inner region scattered fields of plant q excited by the ith plane wave. With (2.26) and (2.30), the solutions of the fields for multiple scatterings in the vegetation layer including both the outside and the inside of the enclosing cylinders are calculated.

2.4 Method Validation

For the simulations presented in this section, we consider vertically (V-pol) and horizontal (H-pol) polarized plane wave from the direction, $\phi_i = 0^o, \theta_i = 40^o$, at L-band 1.41 GHz with $\lambda = 21.3cm$, which is the operation frequency and incident angle of NASA Soil Moisture Active Passive (SMAP) mission [6]. Most of the results, unless otherwise stated, are for V-pol incident plane wave. Each wheat plant is modelled by 8 thin cylinders with randomly generated orientation angles (θ_c, α_c). The inclination angle θ_c follows a normal distribution within $[0^o, 6^o]$ and the azimuthal angle α_c is uniformly distributed within $[0, 360^o]$. The radius of the cylinder is $r_c = 2mm$ and its length l_c is linearly proportional to the VWC of wheat. In the calculation of the T-matrix, the enclosing cylinder has radius $C_r = 6.5cm$ and height $C_h = l_c + 2cm$, which is $2cm$ higher than the thin cylinder. We validate the results for a single wheat plant and for 4 wheat plants by comparing the results of the two-step hybrid method with direct field solutions of the HFSS.

2.4.1 Convergence Test of T-matrix

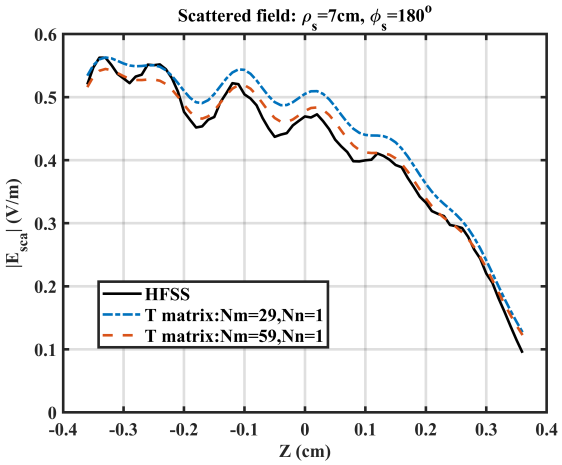

Figure 2.4: Scattered $\bar{E}$ fields on a vertical line parallel to z axis calculated from T-matrix with different number of modes are compared with those solved form the HFSS.

In the hybrid method, the scattered fields of a single plant are related to the exciting fields through the T-matrix, whose accuracy is determined by the number of modes $\alpha = 2(2N_n + 1)N_m$ used in the representation of T-matrix. In general, α is determined by the electrical size of the enclosing cylinder and the enclosed target, and more modes are needed for a more complicated target as it can produce more complicated scattered fields. The T-matrix of a single wheat plant with $l_c = 70cm$ is calculated following the procedure described in Sec 2.3.1 with k_z being truncated at $K_z^{max} = k_0$. Only the propagation waves are considered outside the cylinder by the T-matrix, as the evanescent waves decay exponentially away from the cylinder and are hence negligible. The scattered fields calculated from the T-matrix with two different numbers of modes are plotted in Fig. 2.4 along with fields directly solved from the HFSS. The observation points are in the near field which is $0.5cm$ outside the circumscribing cylinder, and lie along a vertical line parallel to z axis. The results show that the differences between the scattered fields calculated from the HFSS and those from the T-matrix decrease as the number of modes increases. For the wheat plant of the example, a T-matrix with $N_m = 29$, $N_n = 1$ is sufficient to characterize its scattered fields.

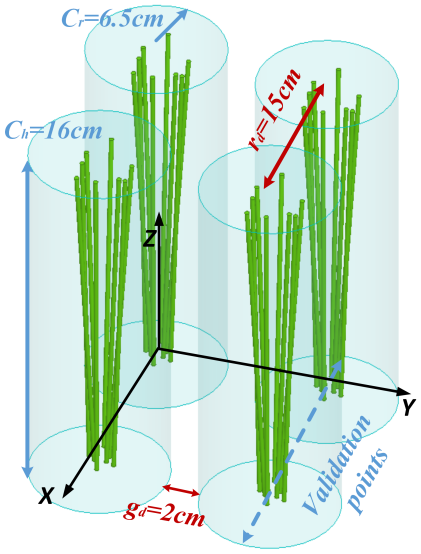

Figure 2.5: Scattering from four wheat plants are solved using the hybrid method and the HFSS, the radius of the circumscribing cylinder $C_r = 6.5cm$, distance between the centers of 2 circumscribing cylinders $r_d = 15cm$, the closest distance between 2 circumscribing cylinders $g_d = 2cm$.

2.4.2 Full-wave Simulation of Four Wheat Plants at L-band

Next, the two-step hybrid method is validated with HFSS by solving wave scattering among 4 wheat plants. As shown in Fig. 2.5(b), four identical wheat plants with $l_c = 14cm$ are placed in a 2×2 array with the row and the gap spacing being $r_d = 15cm$ and $g_d = 2cm$, respectively. This problem can be solved directly using the HFSS and also the proposed hybrid method. By combining the calculated T-matrix of an individual plant with the FL equations, the final scattered field coefficients are obtained. Then the scattered fields are calculated using (2.26) and (2.30). The scattered fields due to the V-pol and the H-pol incident plane wave are shown in Fig. 2.6. The observation points, $1cm$ below the four wheat plants, are parallel to the x axis passing through both the gap and the inner region as denoted by the dash line in Fig. 2.5. Since the cylinders are thin and the orientations are close to the vertical direction, the scattered fields due to a H-pol excitation is much weaker than that of the V-pol. Consequently, the relative error of the H-pol is larger than that of the V-pol. Overall, the results of the hybrid method agree well with those directly solved from the HFSS except the small jumps on the boundary between the inner and the gap regions. The truncation of modes when extracting the T-matrix cause the discontinuity of the fields. The

magnitude of the discontinuity could be reduced by including more modes in the T-matrix. In Fig. 2.7, the total $\bar{E}$-fields on a plane, $1cm$ below the wheat field, obtained from the hybrid method are compared with those directly solved from the HFSS. The results are in good agreement.

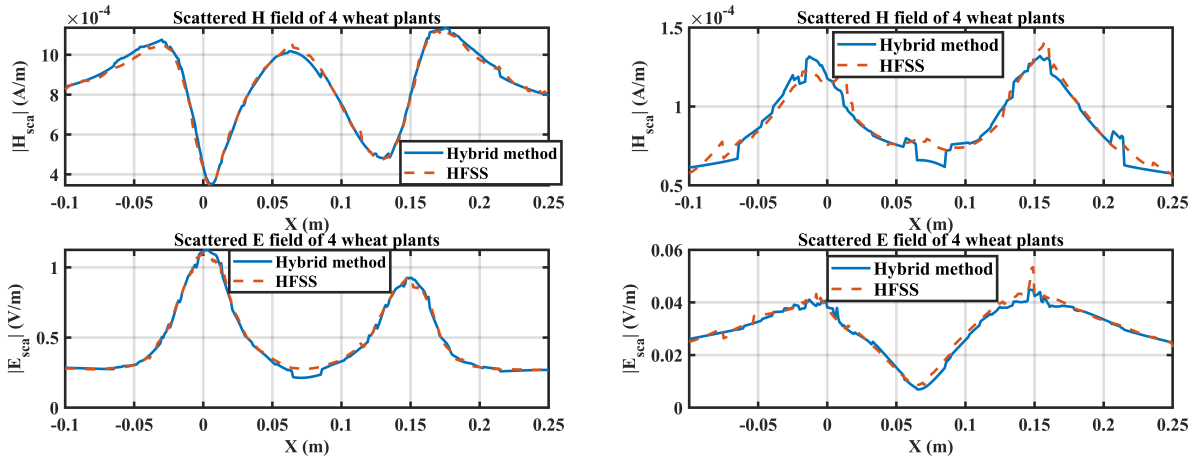

(a) (b)

Figure 2.6: Scattered fields vary with x at the bottom of the 4 wheat plants with $z = -1cm$ and $y = 0cm$, (a) excited by vertical polarized incident plane wave, and (b) excited by horizontal polarized incident plane wave.

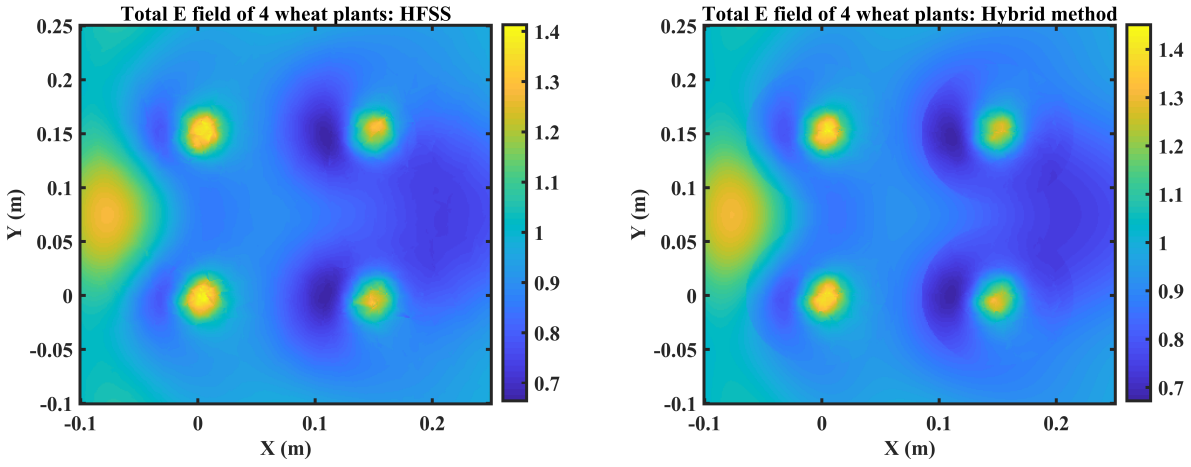

(a) (b)

Figure 2.7: Total $\bar{E}$ fields excited by a vertical polarized incident plane wave on a plane $1cm$ below the four wheat plants solved from (a) HFSS and (b) the hybrid method.

2.5 Summary

The hybrid method for full-wave simulation of vegetation field are presented in this chapter. A realistic geometry setup that can account for the gap effects and the plant structures is introduced. Based on the geometrical configuration, the large scale scattering problem is decomposed and solved in two steps. In the first step, the numerical solver is employed to simulate the scatterings of a single wheat plant, capturing all the structural and clustering effects on scatterings. Then, we use the near-field to calculate the T-matrix that relates the exciting fields to the scattered fields of a single plant based on the Huygens principle and the VCW expansion. In the second step, the multiple scatterings between different plants are considered through the FL equations using the extracted T-matrices and the translation addition theorem of the VCW. The hybrid method are validated with HFSS by comparing the field solutions of scatterings from 4 wheat plants.

Appendix

In this appendix, the detailed derivation of the translational addition (TA) theorem including both the scalar and vector case are provided. The physical and mathematical understanding of the TA theorem together with its convergence are also discussed. The TA theorem is an important tool for solving the FLE analytically as they can relate the responses of scatterers centered at different locations. Specifically, the TA theorem expresses the outgoing cylindrical wave centered at $\bar{\rho}_p$ in terms of the incoming cylindrical wave centered at $\bar{\rho}_q$. The transformation enables the hybrid method to obtain a set of closed-form equations for solving the FLE.

2.A Translational Addition Theorem

Scalar Translational Addition Theorem

Suppose there is a cylindrical wave is centered at $\bar{\rho}_p$, and we want to transform as cylindrical wave centered at $\bar{\rho}_q$ as shown in Fig. 2.A.1. Let $\overline{\rho_p\rho_q} = \bar{\rho}_p - \bar{\rho}_q$ be the vector pointing from $\bar{\rho}_q$ to $\bar{\rho}_p$ and $\phi_{\overline{\rho_p\rho_q}}$ be the azimuthal angle it makes with x-axis. Following the same convention, we denote the other two vectors, $\bar{\rho} - \bar{\rho}_p$ and $\bar{\rho} - \bar{\rho}_q$, respectively, as $\overline{\rho\rho_p},\ \phi_{\overline{\rho\rho_p}}$ and $\overline{\rho\rho_q},\ \phi_{\overline{\rho\rho_q}}$. From the vector algebra, we know

$$\bar{\rho} - \bar{\rho}_p = \bar{\rho} - \bar{\rho}_q - (\bar{\rho}_p - \bar{\rho}_q) \tag{2.31}$$

which decomposes $\bar{\rho} - \bar{\rho}_p$ into two parts. The TA theorem states that if $|\bar{\rho} - \bar{\rho}_q| < |\bar{\rho}_p - \bar{\rho}_q|$, then the $H_n^{(1)}(k|\bar{\rho} - \bar{\rho}_p|)$ representing the outgoing wave centered at $\bar{\rho}_p$ can be expressed as the linear

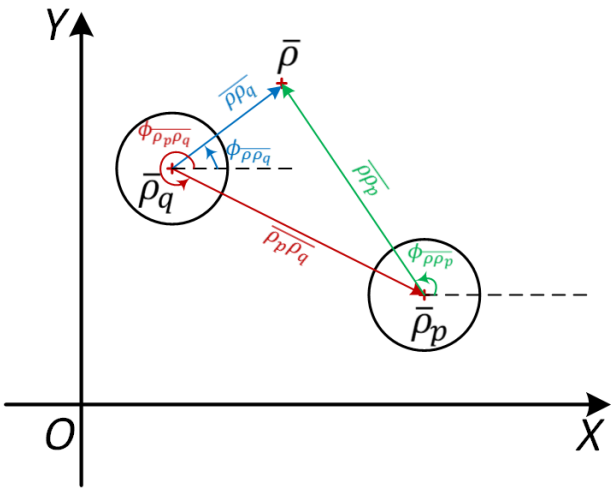

Figure 2.A.1: Translational addition theorem in the cylindrical coordinate system.

combination of $J_m(k|\bar{\rho}-\bar{\rho}_q|)$ which is the incoming wave centered at $\bar{\rho}_q$ through

$$H_n^{(1)}(k|\bar{\rho}-\bar{\rho}_p|)e^{in\phi_{\overline{\rho\rho_p}}} = \sum_m J_m(k|\bar{\rho}-\bar{\rho}_q|)e^{im\phi_{\overline{\rho\rho_q}}} H_{m-n}(k|\bar{\rho}_p-\bar{\rho}_q|)e^{-i(m-n)\phi_{\overline{\rho_p\rho_q}}}. \tag{2.32}$$

If $|\bar{\rho}-\bar{\rho}_q| > |\bar{\rho}_p-\bar{\rho}_q|$, then $H_n^{(1)}\left(k\,|\bar{\rho}-\bar{\rho}_p|\right)$ is expressed as outgoing wave centered at $\bar{\rho}_q$ through

$$H_n^{(1)}(k|\bar{\rho}-\bar{\rho}_p|)e^{in\phi_{\overline{\rho\rho_p}}} = \sum_m H_m(k|\bar{\rho}-\bar{\rho}_q|)e^{im\phi_{\overline{\rho\rho_q}}} J_{m-n}(k|\bar{\rho}_p-\bar{\rho}_q|)e^{-i(m-n)\phi_{\overline{\rho_p\rho_q}}}. \tag{2.33}$$

For Bessel function of $J_n\left(k\,|\bar{\rho}-\bar{\rho}_p|\right)$, there is no inequality requirement in terms of the position. The incoming wave centered at $\bar{\rho}_p$ can always be expressed as the incoming wave centered at $\bar{\rho}_q$ through

$$J_n\left(k\,|\bar{\rho}-\bar{\rho}_p|\right)e^{in\phi_{\overline{\rho\rho_p}}} = \sum_m J_m(k|\bar{\rho}-\bar{\rho}_q|)e^{im\phi_{\overline{\rho\rho_q}}} J_{m-n}\left(k\,|\bar{\rho}_p-\bar{\rho}_q|\right)e^{-i(m-n)\phi_{\overline{\rho_p\rho_q}}} \tag{2.34}$$

These are the scalar translational addition theorem which relate the outgoing (incoming) wave centered at $\bar{\rho}_p$ to the outgoing (incoming) wave centered at $\bar{\rho}_q$.

Convergence of Translational Addition Theorem

We can observe that in (2.32) and (2.33) the Bessel function $J_n(w)$ always has the smaller argument, while the Hankel function $H_n^{(1)}(w)$ has the larger one. The mathematical understanding is follow. The left hand side (LHS) of the identity is a finite value of $H_n^(1)(k|\bar{\rho} - \bar{\rho}_p|)$ and the right hand side (RHS) is the summation of Bessel and Hankel function over m. To make the transformation be valid, the RHS should converges as m increase. Given the distance $\bar{\rho} - \bar{\rho}_q$ or with a fixed argument w, the large order asymptotic expansion of the Bessel and Hankel function are known as

$$\lim_{n\to\infty} J_n(w) \approx \frac{1}{\sqrt{2\pi n}} \left(\frac{ew}{2n}\right)^n \tag{2.35}$$

$$\lim_{n\to\infty} Y_n(w) \approx -\sqrt{\frac{2}{\pi n}} \left(\frac{ew}{2n}\right)^{-n} \tag{2.36}$$

$$\lim_{n\to\infty} H_n(w) \approx \frac{1}{\sqrt{2\pi n}} \left(\frac{ew}{2n}\right)^n - i\sqrt{\frac{2}{\pi n}} \left(\frac{ew}{2n}\right)^{-n} \tag{2.37}$$

It is noticed that the $J_n(w)$ decreases with n, while $H_n(w)$ increases with n. The convergence of the summation requires that the term in the series should decrease with n. Thus the transformation relies on the decrease of J_n to be faster than the increase of H_n in order to make the summation converge. This is reason why the argument of $J_n(w)$ is always larger than that of $H_n(w)$.

In theory, the range of the transformation series is from $-\infty$ to ∞. In practice, the summation is truncated when the result is converged. Then the following question is what is the sufficient order we should consider so that the transformation is valid. The number of term in the summation or the maximum $N_{\max}$ is determined by the argument

$$w = k_\rho |\bar{\rho} - \bar{\rho}_q| = k \sin\theta |\bar{\rho} - \bar{\rho}_q| \tag{2.38}$$

The dominant factor in the large order approximation is

$$\lim_{n\to\infty} J_n(w) \propto \left(\frac{ew}{2n}\right)^n \tag{2.39}$$

The Bessel function $J_n(w)$ starts to decrease when $ew/2n < 1$, then $N_{\max}$ the maximum n should satisfy

$$N_{\max} > \frac{ew}{2\eta} \tag{2.40}$$

where $\eta \in (0,1)$. If $\eta = 0.5$, then $N_{\max} = ew$. This is the rule for truncating the transformation series.

Vector Translational Addition Theorem

By applying the scalar wave transformation to the vector wave, we can obtain the 2D vector wave transformation which is given in the page 477 of [17]

$$\bar{M}_m(k_z, \bar{\rho} - \bar{\rho}_p) = \sum_n Rg\bar{M}_n(k_z, \bar{\rho} - \bar{\rho}_q) H^{(1)}_{n-m}(k_\rho|\bar{\rho}_p - \bar{\rho}_q|) \exp(-i(n-m)\phi_{\overline{\rho_p\rho_q}}), \quad if\ |\bar{\rho} - \bar{\rho}_q| < |\bar{\rho}_p - \bar{\rho}_q| \tag{2.41}$$

$$\bar{M}_m(k_z, \bar{\rho} - \bar{\rho}_p) = \sum_n Rg\bar{M}_n(k_z, \bar{\rho}_p - \bar{\rho}_q) H^{(1)}_{n-m}(k_\rho|\bar{\rho} - \bar{\rho}_q|) \exp(-i(n-m)\phi_{\overline{\rho\rho_q}}), \quad if\ |\bar{\rho} - \bar{\rho}_q| > |\bar{\rho}_p - \bar{\rho}_q| \tag{2.42}$$

where $\bar{M}_m(k_z, \bar{\rho} - \bar{\rho}_p)$ is the outgoing cylindrical wave centered at $\bar{\rho}_p$ and $Rg\bar{M}_m(k_z, \bar{\rho} - \bar{\rho}_q)$ is the incoming cylindrical wave centered at $\bar{\rho}_q$. The 3D vector cylindrical wave are related to the 2D vector cylindrical wave through an exponential term considering the phase in z direction

$$\bar{M}_m(k_z, \bar{r} - \bar{r}_p) = \bar{M}_m(k_z, \bar{\rho} - \bar{\rho}_p) \exp(ik_z(z - z_p)) \tag{2.43}$$

$$\bar{M}_m(k_z, \bar{r} - \bar{r}_q) = \bar{M}_m(k_z, \bar{\rho} - \bar{\rho}_q) \exp(ik_z(z - z_q)) \tag{2.44}$$

which include the $\bar{\rho}$ and z dependent. Substitution of $\bar{M}_m(k_z, \bar{\rho} - \bar{\rho}_p)$ in (2.44), we get

$$\bar{M}_m(k_z, \bar{r} - \bar{r}_p) = \sum_n Rg\bar{M}_n(k_z, \bar{\rho} - \bar{\rho}_q) H^{(1)}_{n-m}(k_\rho|\bar{\rho}_p - \bar{\rho}_q|) \exp(-i(n-m)\phi_{\overline{\rho_p\rho_q}}) \times \exp(ik_z(z - z_p)) \tag{2.45}$$

By adding the exponential term $\exp(ik_z(z-z_q))$ to the RHS

$$\begin{aligned}\bar{M}_m\left(k_z,\bar{r}-\bar{r}_p\right)=\sum_n Rg\bar{M}_n\left(k_z,\bar{\rho}-\bar{\rho}_q\right)\exp\left(ik_z\left(z-z_q\right)\right)H^{(1)}_{n-m}\left(k_\rho\left|\bar{\rho}_p-\bar{\rho}_q\right|\right)\\ \times\exp\left(-i\left(n-m\right)\phi_{\overline{\rho_p\rho_q}}\right)\exp\left(ik_z\left(z-z_p\right)\right)\exp(-ik_z(z-z_q))\end{aligned} \tag{2.46}$$

we construct the $Rg\bar{M}_n\left(k_z,\bar{r}-\bar{r}_q\right)$ and by simplifying the z dependent term, we get

$$\begin{aligned}\bar{M}_m\left(k_z,\bar{r}-\bar{r}_p\right)=\sum_n Rg\bar{M}_n\left(k_z,\bar{r}-\bar{r}_q\right)H^{(1)}_{n-m}\left(k_\rho\left|\bar{\rho}_p-\bar{\rho}_q\right|\right)\exp\left(-i\left(n-m\right)\phi_{\overline{\rho_p\rho_q}}\right)\\ \times\exp\left(-ik_z\left(z_p-z_q\right)\right)\end{aligned} \tag{2.47}$$

Following the similar process, another 3D TA transformation can be obtained and they are summerized as

$$\bar{M}_m\left(k_z,\bar{r}-\bar{r}_p\right)=\begin{cases}\sum_n Rg\bar{M}_n\left(k_z,\bar{r}-\bar{r}_q\right)H^{(1)}_{n-m}\left(k_\rho\left|\bar{\rho}_p-\bar{\rho}_q\right|\right)\exp\left(-i\left(n-m\right)\phi_{\overline{\rho_p\rho_q}}\right)\\ \exp\left(-ik_z\left(z_p-z_q\right)\right),\ if\ \left|\bar{\rho}-\bar{\rho}_q\right|<\left|\bar{\rho}_p-\bar{\rho}_q\right|\\ \sum_n R_g\bar{M}_n\left(k_z,\bar{r}_p-\bar{r}_q\right)H^{(1)}_{n-m}(k_\rho|\bar{\rho}-\bar{\rho}_q|)\exp(-i(n-m)\phi_{\overline{\rho\rho_q}})\\ \times\exp\left(-ik_z(z_p-z_q)\right),\ if\ \left|\bar{\rho}-\bar{\rho}_q\right|>\left|\bar{\rho}_p-\bar{\rho}_q\right|\end{cases} \tag{2.48}$$

In compact form, it can be written as

$$\begin{aligned}\bar{\beta}_m\left(k_z,\bar{r}-\bar{r}_p\right)=\sum_n Rg\bar{\beta}_n\left(k_z,\bar{r}-\bar{r}_q\right)H^{(1)}_{n-m}\left(k_\rho\left|\bar{\rho}_p-\bar{\rho}_q\right|\right)\exp\left(-i\left(n-m\right)\phi_{\overline{rr_p}}\right)\\ \times\exp\left(-ik_z\left(z_p-z_q\right)\right)\end{aligned} \tag{2.49}$$

where $\beta=M,N$. The 3D vector translational addition theorem can be used to consider interaction of scatterer centered at different locations and thus the FLE can be solved analytically.

2.B Foldy-Lax Multiple Scattering Equations

The FLE can be formulated either using the final exciting field or the final scattered field. The final excitation field formulation has been presented in Sec. 2.3.2. The scattered field formulation is given in this appendix. Using the VCW expansions, the final scattered field of particle q is expressed in terms of VCW centered at $\bar{r}_q$

$$\bar{E}_{s,q}(\bar{r}) = \sum_m \int dk_z \left[\bar{M}_m(k_z, \overline{rr_q})\, a^{SM}_{m,q}(k_z) + \bar{N}_m(k_z, \overline{rr_q})\, a^{SN}_{m,q}(k_z) \right] \tag{2.50}$$

where $a^{S\beta}_{m,q}(k_z)$ are the total final scattered field coefficient of particle q. The final scattered field can be decomposed into two parts based on their excitation

$$\bar{E}_{s,q}(\bar{r}) = \bar{E}^{inc}_{s,q}(\bar{r}) + \bar{E}^{other}_{s,q}(\bar{r}) \tag{2.51}$$

The first part in is $\bar{E}^{inc}_{s,q}(\bar{r})$ which is the scattered field caused by the direct incident field shining on particle q

$$\bar{E}^{inc}_{s,q}(\bar{r}) = \sum_m \int dk_z \left[\bar{M}_m(k_z, \overline{rr_q})\, a^{SM}_{m,q(inc)}(k_z) + \bar{N}_m(k_z, \overline{rr_q})\, a^{SN}_{m,q(inc)}(k_z) \right] \tag{2.52}$$

The second part is $\bar{E}^{other}_{s,q}(\bar{r})$ which is the scattered field caused by all other scatterers

$$\bar{E}^{other}_{s,q}(\bar{r}) = \sum_{p,p\neq q} \sum_m \int dk_z \left[\bar{M}_m(k_z, \overline{rr_q})\, a^{SM}_{m,p}(k_z) + \bar{N}_m(k_z, \overline{rr_q})\, a^{SN}_{m,p}(k_z) \right] \tag{2.53}$$

Substitute (2.52) and (2.53) into the scattering field formulation (2.51), we get

$$\begin{aligned} \sum_m \sum_\beta \int dk_z \bar{\beta}_m(k_z, \overline{rr_q})\, a^{S\beta}_{m,q}(k_z) = &\sum_m \sum_\beta \int dk_z \bar{\beta}_m(k_z, \overline{rr_q})\, a^{SM}_{m,q(inc)}(k_z) \\ &+ \sum_{p,p\neq q} \sum_m \int dk_z \left[\bar{\beta}_m(k_z, \overline{rr_q})\, a^{S\beta}_{m,p}(k_z) \right] \end{aligned} \tag{2.54}$$

Balancing the coefficient of the VCW by canceling $\sum_m \int dk_z \bar{\beta}_m (k_z, \bar{r} - \bar{r}_q)$ in both side of 2.54, we obtain

$$a_{m,q}^{S\beta(r_q)}(k_z) = a_{m,q(inc)}^{S\beta(r_q)}(k_z) + \sum_{p,p\neq q} a_{m,p}^{S\beta(r_q)}(k_z) \tag{2.55}$$

where the center of the corresponding VCW in (2.55) are denoted in the supper script. It should be noticed that the T-matrix of qth scatterer is defined based on the VCW centered at $\bar{r}_q$. Thus the $a_{m,q(inc)}^{S\beta(r_q)}$ in (2.55) is consistent with those defined in the T-matrix of qth scatterer. However, the $a_{m,p}^{S\beta(r_q)}(k_z)$ in (2.55) are associated with the VCW centered at $\bar{r}_q$ and thus different from $a_{m,p}^{S\beta(r_p)}(k_z)$ which are associated with the VCW centered at $\bar{r}_p$. The $a_{m,p}^{S\beta(r_p)}(k_z)$ and $a_{m,p}^{S\beta(r_q)}(k_z)$ are different and can be related through the translational addition theorem.

The scattering field coefficients of $a_{m,q(inc)}^{S\beta(r_q)}$ excited by the incident field are obtained from the T-matrix of qth scatterer through

$$a_{m,q(inc)}^{S\beta(r_q)}(k_z) = \sum_{m'} \int dk_z' \left[\bar{T}_{mm',q}^{\beta M}(k_z, k_z')\, a_{m',q}^{IM(r_q)}(k_z') + \bar{T}_{mm',q}^{\beta N}(k_z, k_z')\, a_{m',q}^{IN(r_q)}(k_z')\right] \delta(k_z' - k_{zi}) \tag{2.56}$$

where $a_{m',q}^{I\beta(r_q)}(k_z')$ are the VCW expansion coefficient of the incident plane wave. The scattered field coefficients $a_{m,p}^{S\beta(r_q)}(k_z)$ due to particle p is obtained from

$$a_{m,p}^{S\beta(r_q)}(k_z) = \sum_{m'} \int dk_z' \left[\bar{T}_{mm',q}^{\beta M}(k_z, k_z')\, a_{m',p}^{EM(r_q)}(k_z') + \bar{T}_{mm',q}^{\beta N}(k_z, k_z')\, a_{m',p}^{EN(r_q)}(k_z')\right] \tag{2.57}$$

where $a_{m',p}^{E\beta(r_q)}(k_z')$ are the exciting field caused by scattered p. The exciting field from particle p is the scattered field of p propagate from $\bar{r}_p$ to $\bar{r}_q$. Using the translational addition theorem (2.49), we have

$$\begin{aligned} \bar{\beta}_{m'}(k_z', \overline{rr_p})\, a_{m',p}^{S\beta(r_p)}(k_z') = \sum_n Rg\bar{\beta}_n(k_z', \overline{rr_q})\, H_{n-m'}^{(1)}\left(k_\rho' |\overline{\rho_p\rho_q}|\right) \\ \times \exp\left(-i(n-m')\phi_{\overline{\rho_p\rho_q}}\right) \exp(-ik_z' z_{pq})\, a_{m',p}^{S\beta(r_p)}(k_z') \end{aligned} \tag{2.58}$$

Let $m' = m, n = m'$, then

$$\begin{aligned}\bar{\beta}_m\left(k'_z, \overline{rr_p}\right) a_{m,p}^{S\beta(r_p)}\left(k'_z\right) = \sum_{m'} Rg\bar{\beta}_{m'}\left(k'_z, \overline{rr_q}\right) H_{m'-m}^{(1)}\left(k'_\rho \left|\overline{\rho_p\rho_q}\right|\right) \\ \times \exp\left(-i\left(m'-m\right)\phi_{\overline{\rho_p\rho_q}}\right) \exp\left(-ik'_z z_{pq}\right) a_{m,p}^{S\beta(r_p)}\left(k'_z\right)\end{aligned} \tag{2.59}$$

This indicates that the order m scattered field from pth scatterer $\bar{\beta}_m\left(k'_z, \overline{rr_p}\right)$ contributes to the order m' excitating field centered at $\bar{r}_q$

$$a_{m',p(m)}^{E\beta(r_q)}\left(k'_z\right) = H_{m'-m}^{(1)}\left(k'_\rho \left|\overline{\rho_p\rho_q}\right|\right) \exp\left(-i\left(m'-m\right)\phi_{\overline{\rho_p\rho_q}}\right) \exp\left(-ik'_z z_{pq}\right) a_{m,p}^{S\beta(r_p)}\left(k'_z\right) \tag{2.60}$$

Summation over m, we get the exciting field coefficient of order m' incoming VCW centered at $\bar{r}_q$

$$a_{m',p}^{E\beta(r_q)}\left(k'_z\right) = \sum_{m} H_{m'-m}^{(1)}\left(k'_\rho \left|\overline{\rho_p\rho_q}\right|\right) \exp\left(-i\left(n-m\right)\phi_{\overline{\rho_p\rho_q}}\right) \exp\left(-ik'_z z_{pq}\right) a_{m,p}^{S\beta(r_p)}\left(k'_z\right) \tag{2.61}$$

Then using the T-matrix of qth scatterer and 2.57, the $a_{m'',p}^{S\beta(r_q)}\left(k_z\right)$ are related to $a_{m,p}^{S\beta'(r_p)}\left(k_z\right)$ through

$$\begin{aligned}a_{m'',p}^{S\beta(r_q)}\left(k_z\right) = \sum_{\beta'}\sum_{m'}\int dk'_z \sum_{m} H_{m'-m}^{(1)}\left(k'_\rho \left|\overline{\rho_p\rho_q}\right|\right) \exp\left(-i\left(m'-m\right)\phi_{\overline{\rho_p\rho_q}}\right) \\ \times \exp\left(-ik'_z z_{pq}\right) \bar{T}_{m''m',q}^{\beta\beta'}\left(k_z, k'_z\right) a_{m,p}^{S\beta'(r_p)}\left(k'_z\right)\end{aligned} \tag{2.62}$$

By substituting (2.56) and (2.62) into (2.55), we obtain the scattered field formulation of the FLE

$$\begin{aligned}a_{m'',q}^{S\beta(r_q)}(k_z) = \sum_{\beta'}\sum_{m'}\int dk'_z \bar{T}_{m'm',q}^{\beta\beta'}\left(k_z, k'_z\right) a_{m',q(inc)}^{I\beta'(r_q)}(k'_z)\delta(k'_z - k_{zi}) + \sum_{p,p\neq q}\sum_{\beta'}\sum_{m'}\int dk'_z \sum_{m} \\ \times H_{m'-m}^{(1)}\left(k'_\rho \left|\overline{\rho_p\rho_q}\right|\right) \exp\left(-i\left(m'-m\right)\phi_{\overline{\rho_p\rho_q}}\right) \exp\left(-ik'_z z_{pq}\right) \bar{T}_{m''m',q}^{MM}\left(k_z, k'_z\right) a_{m,p}^{S\beta'(r_p)}\left(k'_z\right)\end{aligned} \tag{2.63}$$

which can be used to solve for the unknown final scattered field coefficients.

CHAPTER 3

Full-wave Simulation of Wheat Field

In this chapter, the hybrid method is applied to perform full-wave simulations of wheat field at multiple frequencies including L-, S-, and C-bands to investigate the frequency dependence of the microwave transmissivity. A physical-iterative method together with Message Passing Interface (MPI) parallel computing are implemented to facilitate the Monte Carlo simulations of wave propagation in the vegetation. The impacts of the plant structures and gaps on the microwave propagation are demonstrated by the comparing the transmissivities of different regions. The results obtained from the hybrid method are also compared with those of the classical radiative transfer equation (RTE) model to illustrate the importance of full-wave simulations.

3.1 Introduction

The interest of using multi-channel microwave measurements for remote sensing of soil moisture has been stimulated by the increasing availability of spaceborn radars and radiometers with different frequencies. In the past, the C- and X-bands of the AMSR-E instrument was used with a dual-frequency method for retrieving soil moisture [38, 39]. In the future, the NASA-ISRO SAR (NISAR) will utilize the L- and S-bands [9] and the Conical Imaging Microwave Radiometer (CIMR) satellite has multiple operating frequencies including L-, C-, X-, Ku-, and Ka-bands [10]. This provides a great opportunity for further improving the L-band soil moisture retrieval by combining frequencies at different bands. The accurate modeling of wave propagation at multiple

frequencies in the vegetation above the soil is crucial for evaluating the feasibility of the multi-frequency approach.

In this chapter, the two-step hybrid method [40] is employed to investigate the frequency dependence of transmissivity by performing full-wave simulations of vegetation at the L-, S-, and C-bands. In the first step, the full-wave solutions of a single plant are calculated using the High-Frequency Structure Simulator (HFSS). The HFSS solutions are then used to obtain the T-matrix of a single plant based on the Huygens principle and the vector cylindrical waves (VCW) expansion of the Dyadic Green's function. The number of modes used in the T-matrices at different frequencies are determined through the convergence tests. The hybrid method treats the entire plant as a single scatterer using the T-matrix which captures the multiple scattering within a single plant caused by its structure. This is different from the RTE which the scatterer is a single cylinder and the plant structure is not considered. In the second step, the multiple scattering among different plants are considered analytically using the multiple scattering theory of Foldy-Lax equations (FLE) and the calculated T-matrices based on the VCW expansion. The accuracy of the hybrid method is validated with HFSS by solving scattering from night wheat plants for a single realization. The hybrid method is implemented with parallel computing using MPI to meet the large memory demand for full-wave simulations at S- and C-bands. Based on the averaging over area for calculating the transmission and the inherent averaging of multiple realizations required for Monte Carlo simulations of multiple scattering in random media, the FLE are solved using a physical iterative method which makes the simulations at least 20 times faster. The scattered fields in the plane below the wheat plants are calculated to illustrate the impact of the plant structure and gaps on the microwave propagation. The transmission in the gap and the inner regions are calculated to demonstrate the effects of coherent multiple scattering. Wheat fields with different row spacing and randomly generated gaps are also simulated to investigate the gap effects on the transmission. Finally, the transmission of microwave through a wheat field obtained from the hybrid method are compared with those calculated from the classical RTE model.

3.2 Parallel Computing of Hybrid Method

The full-wave simulation of vegetation field is a complex large scale problem. In order to include the multiple scattering of plants in the Monte Carlo simulations of random media, a large number of plants is required in a single realization. In the numerical results section, we calculate multiple scattering among 169 plants. The large scale problem cannot be solved directly using the numerical methods as the required computation demand is unaffordable. Neither can it be solved by the analytical approaches due to their limitations on handling the scattering of complex structure. To overcome these challenges, the scattering problem is partitioned into two steps in the hybrid method where the scattering of a single plant with complicate structure are solved numerically in the first step, and the large scale modelling challenges are handled analytically in the second step by using the FLE and the T-matrix based on the VCW expansion. Despite the significant reduction in the computation cost by utilizing the analytical method, the hybrid method still has a high memory demand especially with increasing frequency (see Table 3.2.1).

Table 3.2.1: The number of modes used in T-matrix and the number of plants simulated at the L-, S-, and C-bands.

Freq (GHz)	λ (cm)	N_ϕ	N_θ	N_m	N_p	Mem (GB)
L : 1.41	21.26	3	29	174	169	12
S : 3.20	9.37	5	59	590	169	150
C : 6.90	4.34	9	59	1062	81	101

3.2.1 Complexity Analysis

In general, the number of modes, equaling to the number of angular directions times the number of polarizations, used in the representation of T-matrix increases with frequency as the multiple scattering get stronger at the higher frequency. As shown in Table 3.2.1, the total number of modes used in the C-band T-matrix is about 6 times of that used in the L-band one. Such increase in number of modes will significantly increase the computation demand for solving the FLE, which is explained by the following comparison between the RTE and the FLE. In the RTE, the wave

propagation in the vegetation is governed by

$$-\frac{dI(\hat{s})}{dS} = \kappa_e I(\hat{s}) + \int d\Omega' P(\hat{s}, \hat{s}') \tag{3.1}$$

where I is the intensity of the wave, κ_e is the effective attenuation rate, and P is the phase matrix describing the incoherent multiple scattering. The computation complexity of the two methods is the product of five factors

$$N = N_\phi N_\theta N_{pol} N_p N_c \tag{3.2}$$

where N is the total number of unknowns, N_ϕ and N_θ respectively are the number of angles sampled in the ϕ and θ directions, N_{pol} is the polarization factor, N_p is the number of plants, and N_c is the coherency factor. The first three factors usually are the same for the two methods, but the last two are different. While the RTE is independent of N_p based on the uniform distribution assumption, the FLE is linearly proportional to N_p as it considers each plant individually through the T-matrix. The coherency factor of RTE is 1 because it only uses intensity to describe the wave. However, the FLE includes both the phase and amplitude of the fields using the complex number, which gives $N_c = 2$. The extra information covered in the FLE enable it to model the effect of gaps between different plants. As a result, the memory demand for solving the FLE, on the order of $\mathcal{O}(N^2)$, will increase rapidly with the number of plants and frequency as shown in Fig. 3.2.1.

This requires a parallel implementation of the hybrid method to meet the huge memory demand for solving the FLE especially at the S- and C-bands. In addition, the wave approach requires Monte Carlo simulations of random media because of random phases due to random positions of the scatterers. In Monte Carlo simulations, many realizations of the sample are generated to represent the random positions of the scatterers and the FLE are solved for each realization. The physical results of absorption, transmission and scattering are obtained by averaging over the solutions of the realizations. In practice, the required number of realizations vary depending on the final results of interest. Emissivity and transmission require fewer realizations, while backscattering requires more realizations. In the next section, the hybrid method is further accelerated using

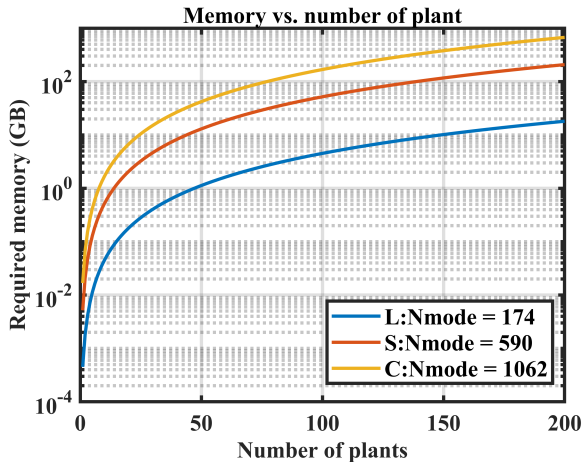

Figure 3.2.1: Memory demand of the hybrid method changes with the number of plants at L-, S- and C-bands.

a physical iterative approach when calculating the transmission.

3.2.2 MPI Parallel Computing

The interaction among different plants are considered by using the Foldy-Lax equations in the second step of the hybrid method. The resulting the matrix equations is solved using the generalized minimal residual method (GMRES) and is implemented with MPI to facilitate the full-wave simulations of wave propagation in the vegetation.

Suppose the resulting linear system obtained from the FLE is

$$Ax = b \tag{3.3}$$

where m is the number of unknowns, $A \in C^{m\times m}$, and $x, b \in C^{m\times 1}$. The goal of iterative method is to solve the matrix by $O\left(m^2\right)$ operations. The classical iterative method such as the conjugate gradient was limited to either positive definite or diagonally dominant matrices. The GMRES method can be applied to solve linear systems $Ax = b$ with arbitrary square matrices. The iterative method is built based on the idea of projecting an m-dimensional problem into a lower dimensional Krylov subspace. In each step of the GMRES, we solve a least square problem to approximate the

exact solution $x^* = A^{-1}b$ by a vector $x_n \in K_n$ such that

$$\min_{x_n} \|Ax_n - b\|_2 \tag{3.4}$$

The process is terminated when it achieves the desired accuracy or reach to a preset maximum iteration.

Let $A \in C^{m\times m}$ be a square matrix and $b \in C^{m\times 1}$ be a vector and the Krylov subspace at step n is known as

$$K_n = \left\{b,\ Ab,\ ...,\ A^{n-1}b\right\} \in C^{m\times n} \tag{3.5}$$

The goal is to find an vector $x_n \in K_n$ that can minimize the norm of the residual as defined in (3.4). The desired vector can be written as

$$x_n = K_n c \tag{3.6}$$

where $c \in C^{m\times 1}$ is the unknown vector. Thus the residual minimization becomes

$$\min_{c} \|AK_n c - b\|_2 \tag{3.7}$$

This can be done by means of a QR factorization of AK_n such that

$$\|AK_n c - b\|_2 = \|QRc - b\|_2 = \left\|Rc - Q^H b\right\|_2 \Rightarrow c = R^{-1}Q^H b. \tag{3.8}$$

However, it is unstable and expensive. Instead, we can use Arnoldi iteration to find the orthonormal basis Q_n of the Krylov subspace K_n. Suppose $Q_n = [q_1,\ ...,\ q_n]$ and

$$Q_n \in K_n = span\left\{b,\ Ab,\ ...,\ A^{n-1}b\right\} \tag{3.9}$$

Then we rewrite

$$x_n = K_n c = Q_n y \tag{3.10}$$

where y is projection vector of x_n on Q_n. Then the equivalent problem is

$$\min_y \|AQ_n y - b\|_2 \tag{3.11}$$

Since the Arnoldi iteration is based on the partial similarity transform of

$$AQ_n = Q_{n+1}\tilde{H}_n \tag{3.12}$$

where $\tilde{H}_n$ is the upper Hessenberg matrix which is a matrix with zeros below the first subdiagnoal. Then

$$\min_y \left\| Q_{n+1}\tilde{H}_n y - b \right\|_2 \tag{3.13}$$

Note that the multiplication by a unitary matrix does not change the 2-norm, then we get

$$\min_y \left\| Q_{n+1}\tilde{H}_n y - b \right\|_2 = \min_y \left\| \tilde{H}_n y - Q_{n+1}^H b \right\|_2 \tag{3.14}$$

Note that the linear system in (3.11) is of size $m \times n$, while the $\tilde{H}_n$ is an $(n+1) \times n$ matrix of smaller size. Thus it is more efficient to solve (3.14).

The second term in (3.14) is

$$Q_{n+1}^H b = \left[q_1^H b, q_2^H b, ...q_{n+1}^H b\right]^T \tag{3.15}$$

Note that the Krylov subspaces are given as $K_1 = span\{b\}, K_2 = span\{b, Ab\}, ...$ and the column vector q_j of Q_n form an orthonormal basis for K_n. Then we have

$$q_1 = \frac{b}{\|b\|},\ q_j^H b = 0,\ for\ j > 1 \tag{3.16}$$

Therefore we have

$$Q_{n+1}^{H} b = \|b\| \, e_1 \tag{3.17}$$

Thus the least square minimization problem at step n is

$$\min_{y} \left\| \tilde{H}_n y - \|b\|_2 \, e_1 \right\|_2 \tag{3.18}$$

and $x_n = Q_n y$. The process of GMRES is described in Algorithm 1.

Algorithm 1 GMRES

$q_1 = b/||b||$

for $n = 1, 2, 3, ...$ **do**

Perform step n of Arnoldi iteration (see Alg.2 in Appendix 3.A)

Find y that mimimizes $||\tilde{H}_n y - ||b||e_1||_2$

Set $x_n = Q_n y$

end for

The computational cost for the GMRES algorithm depends on the cost of solving the least square problem and Arnoldi iteration. As we discussed before, the bottleneck of solving the linear system is the memory required for storing the FLE matrix and is resolved by using the MPI parallel computing technique. To validate the convergence performance of the GMRES method and the parallel efficiency, a wheat field with 81 plants of height $l = 42$ cm is simulated at L-band. The number of mode used in the T-matrix is $N_m = 174$ and the total number of unknowns is $N_{un} = 14094$. It requires 3GB for storing the FLE matrix. The linear system is solved using both the Conjugate Gradient method and the GMRES method. Fig.3.2.2(a) plots the convergence of the solution versus the iteration. The result shows that the GMRES has a much faster convergence rate.

To test the parallel performance, the problem is solved using different number of CPUs and the time of solving the problem is plotted in Fig.3.2.2(b). We can see the time request is significantly reduced due to the employment of multi-CPUs. The speedup of the parallel computing is defined

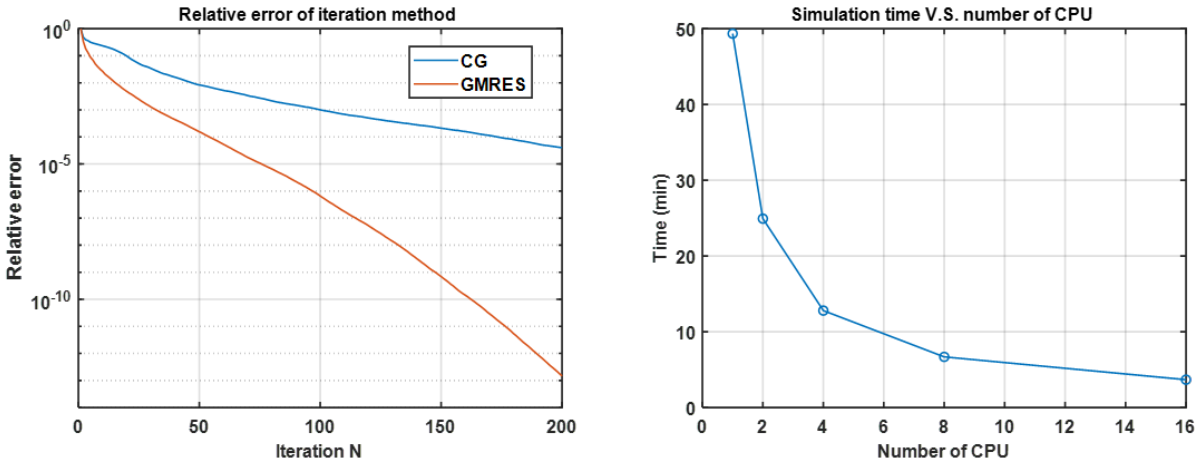

(a) (b)

Figure 3.2.2: (a) Convergence of GMRES method vs. iteration, (b) MPI parallel performance.

as

$$S = \frac{T_s}{T_p} \tag{3.19}$$

where T_s and T_p respectively are the time of using 1 and multiple CPUs to solve the problem. The parallel efficiency is defined as

$$E = \frac{S}{N} = \frac{T_s}{NT_p}. \tag{3.20}$$

The two parameters are calculated and shown in Table 7 to quantify the performance of the parallel computing. We can see due to the extra communication cost between different CPUs, both the parallel efficiency and the speedup decrease with the number of CUP. Overall, it maintains a efficiency greater than 80%.

Table 3.2.2: Efficiency and speedup as a function of number of processors for full-wave simulation of vegetation.

# of CPU.	Time (min)	Efficiency	Speedup
1	49.35	100%	1.00
2	24.93	98.98%	1.98
4	12.80	86.41%	3.86
8	6.69	82.22%	7.34

3.3 Method Validation

Table 3.3.1: Length of cylinder for different VWC.

VWC (kg/m^2)	0.58	1.72	2.87
$l_c\,(cm)$	14	42	70

In this section, we validate the accuracy of the hybrid method by studying the results of one plant and nine plants at the L-, S-, and C-bands. The results are compared with direct solutions of HFSS. The excitation is a vertical polarized (V-pol) plane wave form the direction $\theta_i = 40^o, \phi_i = 0^o$ and the frequencies used in the three different bands are listed in Table 3.2.1. The stem of the wheat is represented by a dielectric cylinder with radius $r_c = 2\ mm$ and its length l_c is linearly proportional to vegetation water content (VWC) as shown in Table 3.3.1. A single wheat plant is modeled by a cluster of 8 cylinders with randomly generated orientation angles (θ_c, ϕ_c). While ϕ_c has a uniform distribution over $[0, 360^o]$, θ_c follows a normal distribution over $[0, 6^o]$. The hybrid method is validated with HFSS at three frequencies by solving scattering from nine wheat plants as shown in Fig. 3.3.2, where they are placed in a 3×3 array with row and column spacing equaling to $14\ cm$ and the corresponding gap spacing is $1\ cm$.

3.3.1 Convergence Test C-band T-matrix

The T-matrix of one single wheat plant is calculated using the full-wave solutions obtained from the HFSS based on the VCW expansion. The two variables in the VCW, k_z and n, have a theoretical range, which is from $-\infty$ to $+\infty$. In practice, they are truncated at a maximum value that ensures the convergence of the scattered fields. Specifically, the continuous integration over k_z is approximated by a discrete summation of N_θ samplings over $[-k_z^{max}, k_z^{max}]$. When $k_z > k_0$, the propagation constant in the $\hat{\rho}$ direction become a imaginary The evanescent waves are excluded in the T-matrix and the maximum propagation constant in z directions is chose to be $k_z^{max} = k_0$. The summation over n is truncated at N_n^{max} making the total number of modes in ϕ direction be $N_\phi = 2(N_n^{max} + 1)$. The N_ϕ and N_θ are determined through the convergence tests. The accuracy

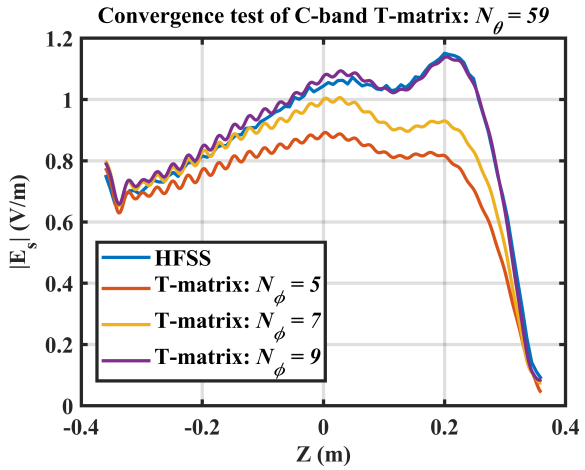

Figure 3.3.1: Amplitude of scattered E-field on a vertical line parallel to z axis calculated from T-matrix with different number of modes are compared with those solved form the HFSS.

of the truncation is validated in the following simulations. As shown in Fig. 3.3.1, the scattered fields of a wheat plant at C-band calculated from T-matrix with different number of modes are compared with the HFSS solutions. The observation points are on one vertical line of the circumscribing surface where $\rho = 6.5\ cm$ and $\phi = 180^o$. The T-matrix solutions of the fields are in good agreement with the fields obtained from the HFSS as N_ϕ increases form 5 to 9. A similar test is also carried out to find the optimal N_θ and usually a higher wheat plant requires a larger N_θ. The same procedures are repeated for the three frequencies to determine the optimal choices of N_θ and N_ϕ, and they are listed in table 3.3.1.

3.3.2 Full-wave Simulation of Night Wheat Plants at C-band

With the calculated T-matrices, we use the FLE to consider the scattering among different plants. For the night wheat plants simulations at L- and S-bands, the wheat height is $44\ cm$ and the scattered fields on one line (Fig. 3.3.2) at the bottom of the wheat field solved from the HFSS and the hybrid method are plotted in Fig. 3.3.3. We can see the scattered fields calculated from the hybrid method, including both inside and outside of the enclosing cylinder, are in good agreement with the HFSS solutions. The agreement validate the truncation of k_z and n made in the T-matrix. However, if the frequency is lower or the plant has a more complicated structure, a wider range of

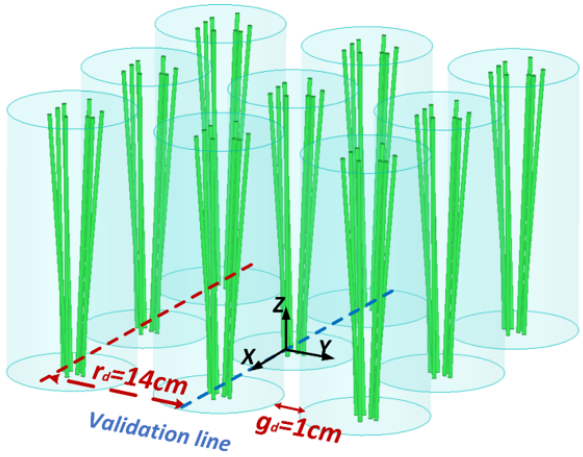

Figure 3.3.2: Scattering from nine wheat plants are solved using the hybrid method and the HFSS, the radius of the circumscribing cylinder $R = 6.5cm$, distance between the centers of 2 circumscribing cylinders $r_d = 14cm$, the closest distance between 2 circumscribing cylinders $g_d = 1cm$.

k_z should be covered in the T-matrix to include the evanescent waves. The wheat height is reduced to $14\ cm$ for the night wheat plants C-band simulation, because this is the maximum height that the HFSS can simulate with the available computation resources. The amplitude of the scattered fields on a plane, which is $1\ cm$ below the wheat field, solved by the two methods are shown in Fig. 3.3.4. We can see a strong field variation caused by the plant structure at the center of each wheat plant. The good agreement of the field solutions verified the accuracy of the hybrid method. Nine plants is the maximum number of plants that can be used in direct HFSS simulations. In the next section, we will use the hybrid method alone to simulate results for the multiple scattering of 169 plants.

3.4 Multi-frequency Simulations of Wheat Field

In this section, the hybrid method is applied to perform full-wave simulations of wheat field at multiple frequencies including L-, S-, and C-bands to investigate the frequency dependence of the transmission. The excitation is a vertical polarized (V-pol) plane wave form the direction $\theta_i = 40^o, \phi_i = 0^o$ and the frequencies used in the three different bands are listed in Table 3.2.1.

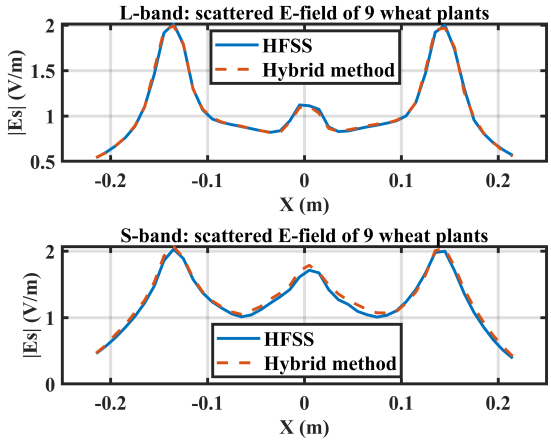

Figure 3.3.3: Amplitude of scattered E-field vary with x at the bottom of the 9 wheat plants with $z = -1cm$ and $y = 0cm$, L-band (top) and S-band (bottom).

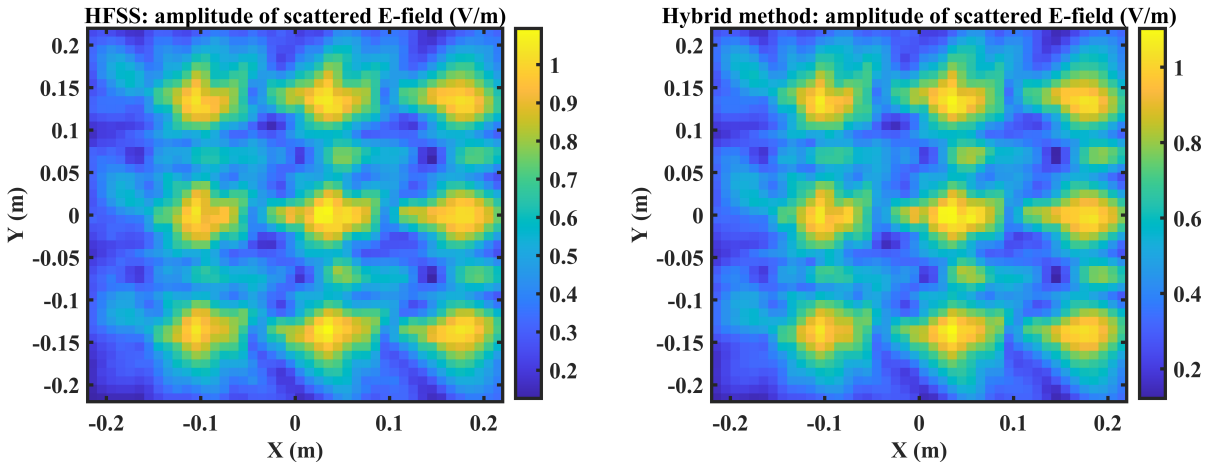

Figure 3.3.4: Amplitude of scattered E-field at C-band excited by a 40^o incident V-pol plane wave on a plane $1cm$ below the night wheat plants solved from (a) HFSS and (b) the hybrid method.

3.4.1 Simulation Setup

The hybrid method is built based on a realistic field configuration that includes both plant structures and gaps within the vegetation canopy. Despite the rapid improvement in the computing technology, the size of the field that can be simulated is still limited by the computation resources. Theoretically, the larger the field size is, the better the simulation result would have. However, a too large vegetation field is actually not necessary, as the scattered fields decay as they propagate outward based on the energy conservation. This indicates that the interaction between two plants

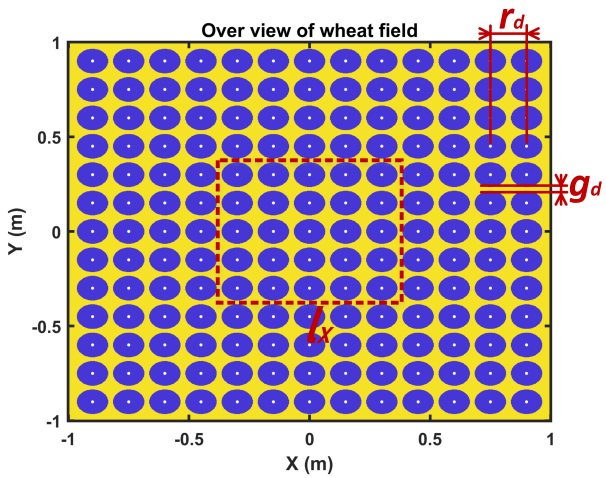

Figure 3.4.1: Top view of the wheat field consisted of 169 plants with row and column spacing $r_d = 14cm$, gap spacing $g_d = 1cm$ and the radius of the circumscribing cylinder $R = 6.5cm$. The square red dash line indicate the reception area of size l_x.

is negligible when they are separated up to a certain distance and thus we can use a finite field to investigate the vegetation effects on microwave. It should also be noted that the field size should be large enough to avoid the edge effects caused by the field truncation. The suitable field size can be determined through a convergence test of l_x, which will be shown in the result section.

The top view of the simulated wheat field, consisting of 169 wheat plants, are shown in Fig. 3.4.1, where each blue circle represents a single wheat plant enclosed by a cylinder of radius $R = 6.5\ cm$. The row and column spacing are both random variables that are assumed to follow Gaussian distribution. Their means values respectively are $r_d = 14\ cm$ and $c_d = 14\ cm$, and the corresponding gap spacing in row and column direction equal to $g_d = 1\ cm$. Different standard deviation will be used to generate the wheat plant positions. The same wheat field of size $1.82\ m \times 1.82\ m$ is used in the L- and S-band simulations, and the corresponding electrical size are $8.6\lambda \times 8.6\lambda$ at L-band and $19.4\lambda \times 19.4\lambda$ at S-band. A wheat field of $29\lambda \times 29\lambda$ with 81 plants is simulated at C-band. We first generate four wheat plants with different structure, and calculate and store the corresponding T-matrices. The T-matrices only need to be calculated once and can be repeatedly used in the following simulations. In each realization of the Monte Carlo simulations, the 4 different wheat plants are randomly placed in the grid positions to form a new wheat field

and the full-wave simulation is performed using the hybrid method. 42668921 After that, the transmission of microwave is obtained through

$$T = \frac{1}{A} \iint_A \frac{\bar{S}^{tot}(\bar{r}) \cdot (-\hat{z})}{\bar{S}^{inc}(\bar{r}) \cdot (-\hat{z})} d\bar{r} \tag{3.21}$$

which is the normalized transmitted power over a reception area of size A at the bottom plane of the wheat field and $\bar{S}$ is the Poynting vector. The final transmission is calculated from an ensemble average over the N realizations.

$$t = \frac{1}{N} \sum_{n=1}^{N} T_n. \tag{3.22}$$

The transmission calculated is the fraction of power transmitted by the plane wave that reaches below the vegetation. The effects of the gaps and the plant structure on the microwave are illustrated by comparing the scattered fields at the bottom plane with different plant heights. The transmission at different regions are also calculated and compared to demonstrate the importance of coherent multiple scattering.

3.4.2 Physical Iterative Method

The wave propagation in the vegetation is a random scattering problem where the scatterers are randomly positioned. The random positioning creates random phases of the scattered fields and causes fluctuations on the wave propagation. In the random scattering problem, only the statistical behavior of the waves are of interest. In the traditional Monte Carlo simulations, as illustrated in Fig. 3.4.2, the exact Maxwell solutions of each realization are solved first and then the final solutions are obtained through the ensemble average over results of all realizations. Specifically, the matrix equations resulting from the FLE is in the form of $\overline{\overline{K}}\bar{A} = \bar{b}$, which is solved iteratively using the generalized minimal residual method (GMRES). The iteration stops when the relative error is sufficiently small $\|\overline{\overline{K}}\bar{A}_i - \bar{b}\|/\|\bar{b}\| < \epsilon_r$, where $\bar{A}_i$ is the solution of the i-th GMRES iteration. Physically, each iteration of GMRES can be understood as one order of multiple scattering among different plants. As we will show in the result section, the exact final scattered fields have

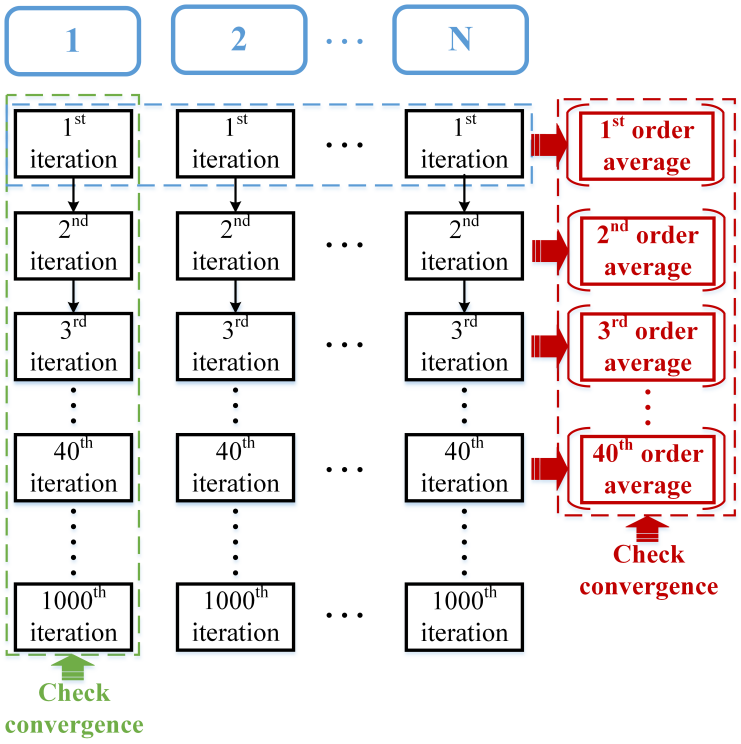

Figure 3.4.2: Diagram of physical iterative method for calculating the statistical average over realizations.

strong variations due to the non-uniform distribution of the scatterers. However, the transmission is obtained based on an averaging over a reception area as indicated in (3.21). We can expect that the fluctuation of the scattered fields will be smoothed out by the averaging and consequently the transmission will converge faster than the scattered fields.

To verify the concept of the physical iterative method, we simulate a wheat field at L-band with 169 plants that are 70 cm long. The convergence of the model field coefficient $\bar{A}$ along with the order of multiple scattering (GMRES iteration) is plotted in Fig. 3.4.3 using the blue line. The red and the yellow curves, respectively, represent the relative error of the scattered fields within the reception area and the relative error of the transmission calculated at each iteration. The benchmark is the solution with an accuracy of $\epsilon_r = 1 \times 10^{-8}$ which is computed from 900 iterations of multiple scattering. We can see that the coefficient $\bar{A}$ converges faster than the electric fields as one model function represents fields on many points, and the transmission T has a larger convergence rate than $\bar{A}$ due to the averaging over the reception area. Because we are interested in

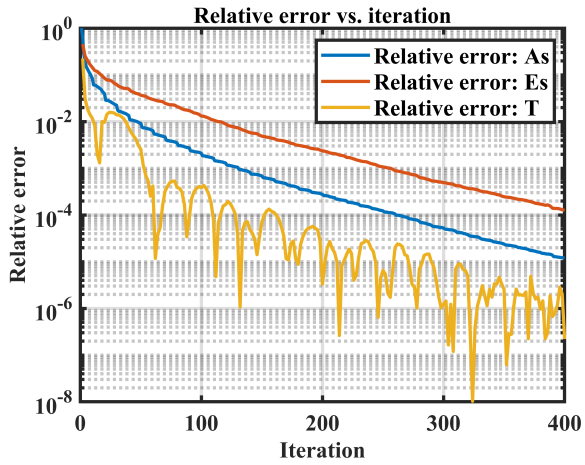

Figure 3.4.3: Convergence of the model field coefficient $\bar{A}$, scattered fields, and transmission T over the order of the multiple scattering.

the transmission accuracy of no more than 1×10^{-3}, the GMRES algorithm can be terminated at the 50-th iteration rather than continue to iterate until the exact field solutions are obtained at the 900-th iteration. This demonstrates that the exact field solutions are not necessary for the adequate precision in the calculation of T in each realization and a faster convergence rate can be achieved through the averaging of fields over area. The same idea can be applied to the averaging over different realizations to further improve the convergence of t.

In the traditional method, the iterations to find the exact solution of Maxwell equations for each realization are completed before performing averaging over realizations to obtain the final results. In the physical iterative method , we can alternate between making iterations and averaging realizations by taking average over realizations after a certain number of iterations until the averaged results converge. As shown in Fig. 3.4.2, in one iteration of the physical iterative method, we first calculate one iteration of multiple scattering and takes averaging over area to obtain T_{1st}^n for all realizations, where the subscript denotes the order of multiple scattering and the superscript $n \in [1, N]$ is the index of realization. Then we average over realizations to obtain $t_1 = \langle T_{1st} \rangle$. The physical iteration iterates until the $t_i = \langle T_{ith} \rangle$ converge. Ten realizations of Monte Carlo simulations are performed to test the physical iterative method and the relative errors of t over the number of iterations are plotted in Fig. 3.4.4. The result shows that the physical iterative method

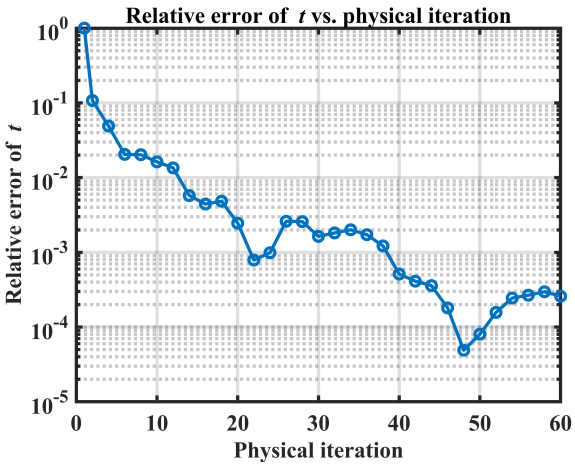

Figure 3.4.4: Convergence of t over the physical iteration, the t is based on a 10 realization average.

only requires 40 iterations to obtain t with an accuracy of 1×10^{-3}, which is 20 times faster than the traditional approach.

The improvement made by the physical iterative method is based on two different averaging in calculating the transmission. The first one is the averaging of fields over area, which is unique for calculating the transmission. For example, the calculation of backscattering and forward scattering do not require such a field averaging process. The second one is the inherent averaging over multiple realizations required for Monte Carlo simulations of multiple scattering in random media. The idea of averaging over realization is applicable for most of the Monte Carlo simulation that is looking for the statistical behavior of certain parameter.

3.5 Result and Discussion

In this section, the full-wave based results calculated from the hybrid method, including the field solutions and transmission of one single realization, are analyzed to demonstrate the vegetation effects on the microwave. The final transmission obtained from the Monte Carlo simulation are compared with those estimated from the RTE.

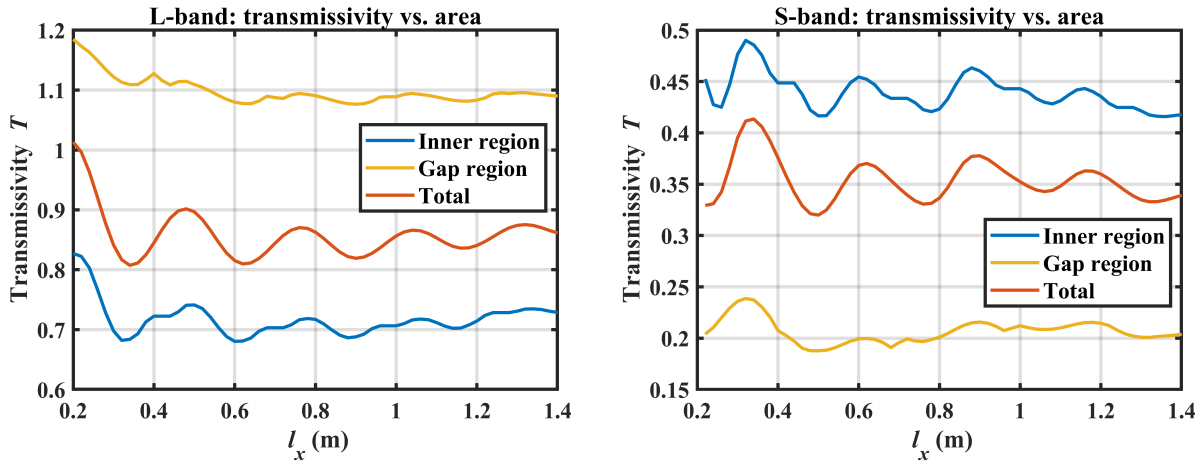

(a) (b)

Figure 3.5.1: Transmission of one realization at inner, gap, and total region vary with the size of reception area: (a) L-band and (b) S-band.

3.5.1 Transmission at Different Regions

The reception area is a square region at the bottom of the wheat field denoted by the red dash lines with size l_x as shown in Fig. 3.4.1. The inner regions and the gap regions are indicated, respectively, by the blue and yellow color. The transmissions at different regions of wheat with $l_c = 42\ cm$ at L- and S-bands are plotted as a function of l_x in Fig. 3.5.1. The convergence of transmissions along with l_x shows that T is independent of the numerical parameter l_x as expected. The total transmission indicated by the red line decreases from around 0.88 to 0.34 as frequency changes from L-band to S-band. It is interesting to note that the transmissivity at L-band in the gap region is greater than 1, which is about 0.36 higher than that of the inner region. However, an opposite trend is observed at S-band, where the inner region has a larger transmission than the gap region. This is because the coherent addition of scattered fields can be either constructive or destructive depending on their phases. This phenomenon cannot be captured using the RTE as it ignores the phase information and assumes the addition of intensities. Consequently, the RTE predicts the same transmission in the inner regions and the gap regions. The distinct transmissions at different regions based on the full-wave simulations demonstrate that the non-uniform distributions of the scatterers have important effects on the transmission.

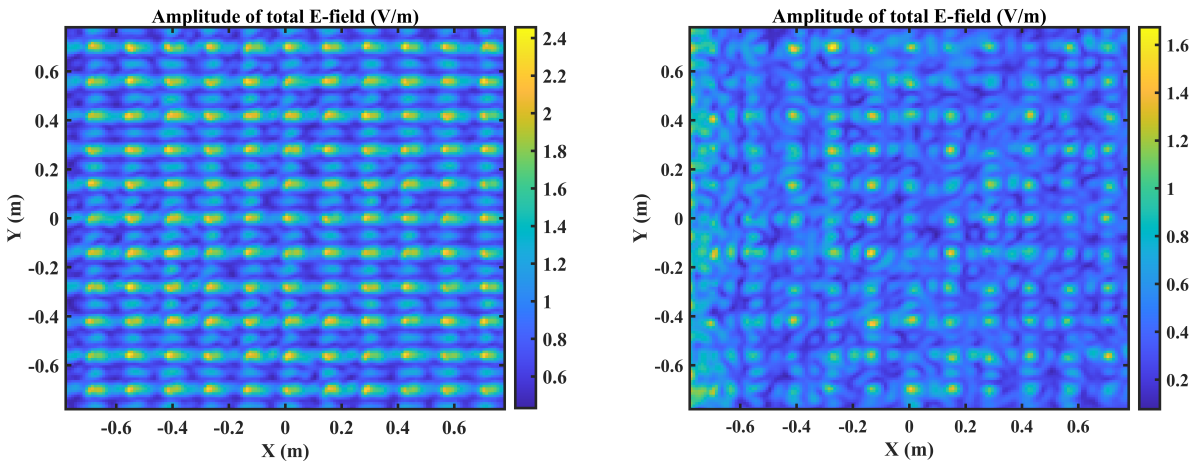

(a) (b)

Figure 3.5.2: Amplitude of total $\bar{E}$-field at S-band excited by a V-pol incident plane wave on a plane $1cm$ below the wheat field: (a) wheat height $h = 14cm$ and (b) wheat height $h = 70cm$.

Fig. 3.5.2 shows the scattered fields at the bottom plane of wheat with two different heights. The excitation field is a vertical polarized plane wave at S-band. The height of the wheat in Fig. 3.5.2 (a) is $14\ cm$ corresponding to a small VWC. In this case, the multiple scattering among different plants are relatively weak compared with the cluster scattering caused by the plant structure. Consequently there are strong field fluctuations at the center of each wheat plant. Moreover, a semi-periodic pattern is also observed in the scattered fields at the bottom plane as the wheat plants are placed at the grid positions. The pattern will be made less visible by the stronger multiple scattering among different plants if the wheat height is increased to $70\ cm$ as shown in Fig. 3.5.2(b). This indicates that multiple scattering among plants can make the scattered fields more random and consequently lead to a decrease in the difference between the transmission at the inner and outer region. The results illustrate the importance of using full-wave simulations to capture different multiple scattering effects within the vegetation layer.

3.5.2 Gap Effects on Transmission

Wheat fields with different gap spacing are simulated to investigate how the gaps affect the transmission. In the following simulations, the column spacing is fixed at 14 cm with a constant 1 cm

Table 3.5.1: Statistics of random gap spacing g_d.

Case	Mean (cm)	Std. (cm)	Range (cm)
1	2.0	0.23	$[1.0, 3.0]$
2	3.0	0.35	$[1.5, 4.5]$

gap, while the row spacing r_d is increased from 14 to 17 cm in a step size of 1 cm. The corresponding gap spacing in the row direction increases from 1 to 4 cm. The full-wave calculated transmissions are listed in Table 3.5.2. The relations between the transmissions and the gap spacing are different depending on the wheat height and frequency. While the L-band transmission for tall wheat increases with gap spacing and the S-band transmission for medium height wheat decreases with it, the transmissions of other cases vary with the gap spacing within 4.0%. The results also show that the transmissions of all the tree different frequencies decrease with the wheat height. The different trends of transmission in terms of g_d demonstrate that the multiple scattering is a complicate process that requires the full-wave simulation to fully capture the gap effects. Nevertheless, the gap effects are less significant than those of the wheat height.

Table 3.5.2: Transmissions of wheat fields with different gap spacing g_d.

Wheat height	Band	Gap spacing g_d (cm)			
		1	2	3	4
14 (cm)	L	0.942	0.942	0.948	0.946
	S	0.777	0.777	0.740	0.749
	C	0.742	0.764	0.754	0.769
42 (cm)	L	0.857	0.865	0.874	0.882
	S	**0.348**	**0.359**	**0.298**	**0.265**
	C	0.366	0.377	0.386	0.398
70 (cm)	L	**0.771**	**0.810**	**0.849**	**0.864**
	S	0.155	0.161	0.183	0.192
	C	0.169	0.160	0.155	0.147

The effects of randomized gap spacing on the transmission are also studied by two sets of simulations, which the gaps in the row direction are randomly generated. The statistics of the gaps are listed in Table 3.5.1, where the mean gap spacing are respectively 2 cm and 3 cm, the variation

ranges are equal to their mean values, and they both follow a quasi-normal distribution within their variation ranges. The results are shown in Table 3.5.3. The results show that the randomized gap spacing do not change the transmission for all the three frequencies. This is because the spacing between the cylinders within a single plant is much smaller than the gap spacing, so the plant structure is the dominant factor of the multiple scattering effects. As a result, the variations in gaps have almost no effects on the transmission.

Table 3.5.3: Transmissions of wheat fields with random g_d.

Freq. (GHz)	L: 1.41		S: 3.20		C: 6.90	
$\langle g_d \rangle$ (cm)	2.0	3.0	2.0	3.0	2.0	3.0
14 (cm)	0.941	0.947	0.775	0.727	0.770	0.768
42 (cm)	0.864	0.872	0.357	0.303	0.377	0.390
70 (cm)	0.808	0.845	0.160	0.181	0.161	0.157

3.5.3 Comparison of Transmission

In this section, the transmissions calculated using the hybrid method are compared with those estimated from the RTE. In the hybrid method, the vegetation canopy is modelled by a realistic wheat field, where each wheat plant consists of 8 dielectric cylinders, the column spacing is 14 cm and the row spacing is $r_d = 16\ cm$. Thus the number of cylinder per unit area is $n_a = 357$. However, in the RTE, the positions of the cylinders are assumed to be statistical homogeneous within the vegetation layer and the wheat field is further approximated as a layered medium with an effective propagation constant based on the independent scattering assumption. The effective extinction coefficient is calculated from

$$\kappa_e = n_0\Big(\langle \sigma_a \rangle + \langle \sigma_s \rangle\Big) \tag{3.23}$$

where n_0 is the number of scatterer per unit volume and is related to n_a through $n_a = n_0/d$, in which d is the thickness of the vegetation layer and is equal to the length of the cylinder; σ_s and σ_a respectively are the scattering and absorption cross section of a single cylinder obtained from op-

tical theorem based on ICA, and $\langle \cdot \rangle$ indicates the ensemble average over the cylinder's orientation angle (θ_c, ϕ_c). Based on the same set of parameters, Fig. 3.5.3 shows the transmissivities of microwave through the wheat fields as a function VWC at three different frequencies calculated using the RTE model and the hybrid method. The transmissivities calculated using the hybrid method are much larger than those computed from the RTE at all the frequencies. For the cases with VWC greater than 1.50 kg/m^2, the transmission obtained from the RTE are almost zero at both the S- and C- bands, while considerable transmissions are still observed using the hybrid method. The approximations made in the RTE, including the homogeneous distribution assumption on the scatterers' position, the incoherent addition of intensity and the ICA approximation in calculating the κ_e, are all responsible for the overestimation of the attenuation. Moreover, the full-wave results show that the attenuation caused by the vegetation layer has a weaker frequency dependence than that of the RTE model. The similar transmissivities calculated using the hybrid method at the S- and C-bands show that the attenuation caused by the vegetation layer will stop increasing as the frequency increases. The considerable transmissions at the S- and C-bands indicate that it would be possible to use the multi-channel signals to further improve the L-band surface parameter retrieval algorithms, such as soil moisture.

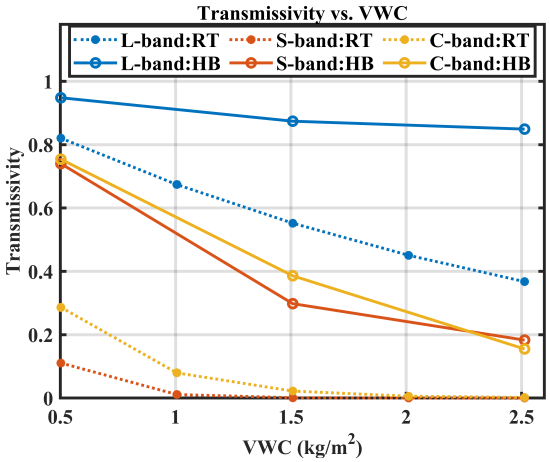

Figure 3.5.3: Transmission of microwave through wheat field calculated using the hybrid method and the RTE model vary with VWC.

3.6 Summary

In this chapter, full-wave simulations of a vegetation field with many plants are performed using the two-step hybrid method to investigate the vegetation effects on microwaves at L-, S- and C-bands. The hybrid method is implemented with parallel computing to meet the large memory demand required at the S- and C-band. The computation efficiency is significantly improved by the physical iterative method. The impacts of the gaps and plant structure on microwave transmission are illustrated by the comparison of transmission at different regions. The simulation results show that the attenuation caused by the vegetation layer will saturate as the frequency increases and the corresponding frequency dependence is much weaker than that predicted by the RTE model. The results suggest that the S- and C-bands measurements could be used to support L-band surface parameter retrieval algorithms, such as soil moisture.

Appendix

In this appendix, we provide the detailed derivation and discussion about the Aroldi iteration used in the GMRES iterative method. Arnoldi process is a Gram-Schmidt-style iteration for transforming a matrix to Hessenberg form. If A is Hermitian, the Hessenberg matrix becomes tridiagonal, the Arnoldi iteration become Lanczos iteration. The Arnoldi is the analogue of Gram-Schmidt for similarity transformations to Hesseberg form rather than QR factorization.

3.A Arnoldi Iteration

A complete reduction of A to Hessenberg form by orthogonal similarity transformation might be written as

$$A = QHQ^H \tag{3.24}$$

where H is the complete Hesseberg matrix of size $m \times m$ and $Q = [q_1, q_2, ..., q_n] \in C^{m \times m}$ is an orthonormal matrix. Let $\tilde{H}_n$ be the $(n+1) \times n$ upper-left section of H, which is also a Hessenberg matrix

$$\tilde{H}_n = \begin{bmatrix} h_{11} & h_{12} & \cdots & h_{1n} \\ h_{21} & h_{22} & & \vdots \\ & \ddots & & \vdots \\ & & h_{n,n-1} & h_{n,n} \\ & & & h_{n+1,n} \end{bmatrix} \tag{3.25}$$

Let Q_n be the first n column of Q_n

$$Q_n = [q_1,\ ...,\ q_n] \tag{3.26}$$

Then we have

$$AQ_n = Q_{n+1}\tilde{H}_n \tag{3.27}$$

where $A \in C^{m\times m}$, $Q_n \in C^{m\times n}$, $Q_{n+1} \in C^{m\times(n+1)}$, and $\tilde{H}_n \in C^{(n+1)\times n}$. The resulting matrix AQ_n is of size $m \times n$. In detail, the nth column of the equation is

$$Aq_n = h_{1n}q_1 + ... + h_{nn}q_n + h_{n+1,n}q_{n+1} \tag{3.28}$$

which means q_{n+1} satisfies an $n+1$ term recurrence relation involving itself and the previous Krylov vectors. Then the q_{n+1} of Q_n can be computed from

$$q_{n+1} = \frac{1}{h_{n+1,n}}\left(Aq_n - \sum_{i=1}^{n} h_{i,n}q_i\right) \tag{3.29}$$

which is known as Arnoldi iteration. The basis vector $\{q_i\}$ are generated by A and b

$$K_n = \left\{b, Ab, ..., A^{n-1}b\right\} \in sapn\left\{q_1, q_2, ..., q_n\right\} \tag{3.30}$$

Since q_i are orthonormal, the Arnoldi process is the systematic construction of orthonormal basis for successive Krylov subspaces.

$$AQ_n = Q_{n+1}\tilde{H}_n \tag{3.31}$$

Note that $Q_n^H Q_{n+1}$ is a rectangular matrix of size $n \times (n+1)$ with the diagnoal component being 1, thus

$$Q_n^H Q_{n+1}\tilde{H}_n :\ n \times n\ Hessenberg\ matrix \tag{3.32}$$

From $AQ_n = Q_{n+1}\tilde{H}_n$, we have the following identities

$$Q_n^H A Q_n = Q_n^H Q_{n+1} \tilde{H}_n = H_n \tag{3.33}$$

which shows that H_n is a projection of A on to K_n based on Q_n. It can be interpreted as the representation in the basis $\{q_1,\ ...,\ q_n\}$of the orthogonal projection of A onto K_n.

Algorithm 2 Arnoldi Iteration

b = arbitrary, $q_1 = b/||b||$

for n=1,2,3... **do**

v = Aq_n

for j=1 to n **do**

h_{jn} = $q_j^H v$

$v = v - h_{jn} q_j$

end for

$h_{n+1,n} = ||v||$

$q_{n+1} = v/h_{n+1,1}$

end for

CHAPTER 4

Full-wave Simulation of Forest

The full-wave simulation of forest is realized by the first time using the two-step hybrid method with two critical issues being successfully resolved in this chapter. First, the inherent restrictions set by the matrix inversion-based approach for calculating the T-matrix of one single plant is removed by revealing the general relation among the T-matrix, the plane wave scattered field coefficient, and the far-field. The Fourier type of transformation enable us to calculate the T-matrix element independently, and thus a far-field based method, applicable for plant of arbitrary size and structure, is built. Second, the memory challenge of the hybrid method is eliminated by adopting the iterative solutions for solving the Foldy-Lax equations (FLE). The proposed methods are validated with FEKO by comparing the field solutions of scattering from three eight meters tall trees. After that, the full-wave Monte Carlo simulations of forest are performed to investigate the tree effects on microwave propagation and the potential of using L-band signal to retrieve soil moisture over the forested area.

4.1 Introduction

The recent studies [41–49] have shown that the L-band microwave signal is able to penetrate through the forest canopy and is potentially used to retrieve the soil moisture in the forest area. This requires an accurate modeling of wave propagation in the forest based on the full-wave simulation. In this chapter, the tree effects on microwave propagation in forest is investigated using the newly developed two-step hybrid method. Although the method has been successfully apply

to simulate wheat field, it can be not directly be used to simulate the forest as the size of tree is much larger than that of crop. While the typical corp height is within 2 meters, the tree can grow up to 20-meter tall with long branches extending out from the trunk. The increase in size creates two challenges for the Hybrid method.

The first challenge is the matrix inversion-based approach for calculating the T-matrix of single plant fails, when the plant has a large electrical size and a complicated structure. This method requires a carefully selection of the incident angles such that all the sufficient information of the scatterer are captured within the corresponding scattering coefficients. In addition, the number of incident waves to be simulated is equal to the number of the modes used in the T-matrix. The reason that the matrix inversion method works for wheat is because a simple stem only structure is used to model the wheat and thus a uniform sampling of the incident angle is good enough for the T-matrix extraction. To overcome this issue, a general relation is discovered in this paper which shows that T-matrix is the coefficient of the Fourier series of the scattered field coefficient. Based on that, a far-field based approach is developed for calculating the T-matrix of one single tree.

The second challenge is the memory demand for solving the closed-form FLE as it increases dramatically with the number of modes used in the T-matrix. For example, the T-matrix of eight meters tall tree contains 20,000 modes and the total unknown for modeling 15 trees is 300,000, thus it requires 1341 GB for storing the resulting Foldy-Lax matrix, which is unaffordable even implemented with parallel computing. This issue is resolved by adopting the physical iterative solution for considering the multiple scattering among different plants, which eliminates the need for direct solution of the FLE.

Due to the limitation of the computation resource, the branches only tree are simulated in this chapter. To consider the tree structure, three different types of components, including the trunk, the primary and secondary branches, are modelled using the dielectric cylinders of different sizes. In the first step, the full-wave simulations of a single tree are performed using the Multilevel Fast Multipole (MLFMM) solver provide by the commercial software of FEKO. The resulting far-field solutions are used to calculate the T-matrix of a single tree. The multiple scattering between the

trunk and branches within a tree are illustrated by comparing the scattered field to those of a single trunk. In the second step, the calculated T-matrix is combined with the FL equations to consider the interaction among different plants. Instead of solving the close-form FL equations directly, a physical iterative solution is adopted to reduce the memory demand for considering the multiple scattering effects. The hybrid method are validated with FEKO by comparing the solution of scattering from three eight meters tall trees. Full-wave simulations of forest with different tree density and height are carried out to investigate the potential of retrieving soil moisture in the forest area using L-band microwave.

4.2 Tree Structure and Forest Configuration

Despite the dramatic advancement of computing power during the last few decades, the capability of the numerical solver is still limited and the full-wave simulation of a single tree (see Fig.4.2.1(a)) including all the branches and leaves is still a very challenge issue, especially when the tree is tall. It is known that the major cause of the absorption is the water contained in the vegetation. Given the fact that most of the water are stored in the trunk and branches, so we do not consider the leaves when modeling the tree. Specifically, three different types of components are included in the tree structure, which are the trunk, the primary and secondary branches. Although a realistic structure can be used in the hybrid method as the numerical solver is employed to perform the single plant full-wave simulation, all the components are modelled using the dielectric cylinders of different size to make the result comparable to the classical RTE model. A 5-meter tall tree is plotted in Fig.4.2.1(b). In the future, the realistic plant structure can be used to further improve the simulation. The full-wave simulation of the branch only tree can be done using the Multilevel Fast Multipole (MLFMM) solver of FEKO. In the hybrid method, each individual plant is treated as a single scatterer and can be enclosed by a cylindrical surface (see Fig. 4.2.1(b)) such that its response can be characterized using VCW based T-matrix.

The hybrid method is built based on a realistic field configuration that can capture both the tree

(a)

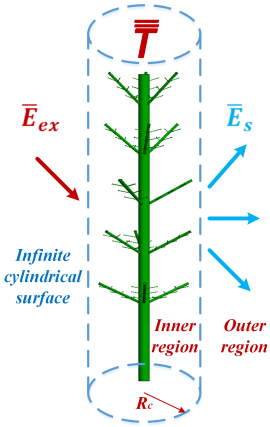

(b)

Figure 4.2.1: (a) Real pine tree, (b) branch only tree model.

structures and the gaps among different trees. The top view of the forest to be simulated is shown in Fig.4.2.2, which is a circular area of radius R. Each small circle denotes one single tree and its radius R_c is the smallest circle that can fully enclose the corresponding tree. The positions of the trees are randomly generated within the circular area and the number of trees is determined by a density parameter. Since each tree is treated as one single scatterer in the hybrid method, we should make sure they are not overlapped with each other when generating their positions. Based on the field configuration, the full-wave simulation of the forest are performed using the hybrid method in two steps.

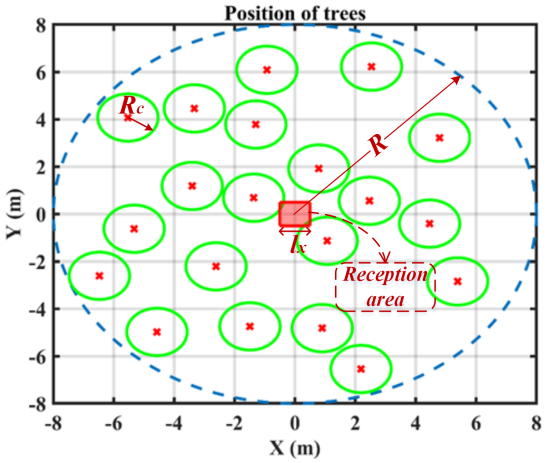

Figure 4.2.2: Top view of forest.

4.3 Hybrid Method for Forest Simulation

4.3.1 T-matrix and Scattered Field Coefficient

The T-matrix is a general approach for describing the response of one single scatterer and is first proposed in [50] based on the spherical wave. The T-matrix concept is extended to cylindrical coordinate in our research to characterize the response of one single plant based on the VCW expansions using the full-wave solutions obtained from the numerical solver. To construct the T-matrix, an infinite cylindrical surface is used to enclose a single plant such that the space is divided into two regions. While the plant is in the inner region, the outer region is the empty space as shown in Fig. 4.2.1(b). Based on the model expansion theory, all the field in the cylindrical coordinate can be expanded in terms of VCW. Specifically, the scattered field in the outer region can be expressed as

$$\bar{E}^s(r) = \sum_n \int dk_z \Big[a_n^{SM}(k_z)\bar{M}_n(k_z,\bar{r}) + a_n^{SN}(k_z)\bar{N}_n(k_z,\bar{r}) \Big] \tag{4.1}$$

where $\bar{M}_n(k_z,\bar{r})$ and $\bar{N}_n(k_z,\bar{r})$ are the outgoing VCW, and $a_n^{SM}(k_z)$ and $a_n^{SN}(k_z)$ are their corresponding expansion coefficients. The outgoing VCW are defined as [37]

$$\bar{M}_n(k_z,\bar{r}) = \Big[\hat{\rho}\frac{in}{\rho}H_n^{(1)}(k_\rho\rho) - \hat{\phi}k_\rho H_n^{(1)'}(k_\rho\rho) \Big] \exp(ik_z z)\exp(in\phi) \tag{4.2}$$

$$\bar{N}_n(k_z,\bar{r}) = \Big[\hat{\rho}\frac{ik_\rho k_z}{k}H_n^{(1)'}(k_\rho\rho) - \hat{\phi}\frac{nk_z}{k\rho}H_n^{(1)}(k_\rho\rho) + \hat{z}\frac{k_\rho^2}{k}H_n^{(1)}(k_\rho\rho) \Big] \exp(ik_z z)\exp(in\phi). \tag{4.3}$$

where $\bar{r} = \hat{\rho}\rho + \hat{\phi}\phi + \hat{z}z$ is the position vector in cylindrical coordinate, $k_\rho = \sqrt{k^2 - k_z^2}$ is the propagation constant in the $\hat{\rho}$ direction, n is the order of harmonic in $\hat{\phi}$ direction, the $H_n^{(1)}(k_\rho\rho)$ is the Hankel function of first kind and $H_n^{(1)'}(k_\rho\rho)$ is the corresponding first order derivative. The excitation field in both regions can be expanded as

$$\bar{E}^{ex}(\bar{r}) = \sum_n \int dk_z \Big[a_n^{EM}(k_z)Rg\bar{M}_n(k_z,\bar{r}) + a_n^{EN}(k_z)Rg\bar{N}_n(k_z,\bar{r}) \Big] \tag{4.4}$$

where $Rg\bar{M}_n(k_z,\bar{r})$ and $Rg\bar{N}_n(k_z,\bar{r})$ are the incoming VCW and their expressions are obtained, respectively, by replacing the $H_n^{(1)}(k_\rho\rho)$ in (4.2) and (4.3) with Bessel function $J_n(k_\rho\rho)$. The corresponding scattering and excitation coefficients are denoted respectively as $a_n^{SM}(k_z)$, $a_n^{SN}(k_z)$ and $a_n^{EM}(k_z)$, $a_n^{EN}(k_z)$. They are related through the T-matrix as

$$a_n^{SM}(k_z) = \sum_{n'} \int dk_z' \Big[T_{nn'}^{MM'}(k_z,k_z') a_{n'}^{EM}(k_z') + T_{nn'}^{MN'}(k_z,k_z') a_{n'}^{EN}(k_z') \Big] \tag{4.5}$$

$$a_n^{SN}(k_z) = \sum_{n'} \int dk_z' \Big[T_{nn'}^{NM'}(k_z,k_z') a_{n'}^{EM}(k_z') + T_{nn'}^{NN'}(k_z,k_z') a_{n'}^{EN}(k_z') \Big] \tag{4.6}$$

This is the definition of the VCW based T-matrix. If the T-matrix of one scatterer is known and the excitation is given, then the corresponding scattered field coefficients can be calculated from (4.5) and (4.6). Then the resulting scattered field is obtained using (4.1).

Let the excitation be a plane wave given as

$$\bar{E}^{ex}(\bar{r}) = (\hat{v}_i E_{vi} + \hat{h} E_{hi}) \exp(ik\hat{k}_i \cdot \bar{r}) \tag{4.7}$$

where $\bar{r}$ is the position vector, k is the propagation constant, $\hat{k}_i$ is the propagation vector, $\hat{v}_i$ and $\hat{h}_i$, respective, are the vertical and horizontal polarization vector of the incident direction (θ_i,ϕ_i), E_{vi} and E_{hi} are their corresponding amplitudes. The triplet $(\hat{k}_i,\hat{v}_i,\hat{h}_i)$ forms an orthonormal unit system and they are defined as

$$\hat{k}_i = \sin\theta_i\cos\phi_i\hat{x} + \sin\theta_i\sin\phi_i\hat{y} + \cos\theta_i\hat{z} \tag{4.8}$$

$$\hat{v}_i = \cos\theta_i\cos\phi_i\hat{x} + \cos\theta_i\sin\phi_i\hat{y} - \sin\theta_i\hat{z} \tag{4.9}$$

$$\hat{h}_i = -\sin\phi_i\hat{x} + \cos\phi_i\hat{y}. \tag{4.10}$$

The VCW coefficients of the plane wave are known as [37]

$$
\begin{aligned}
a_{n'}^{EM}(k_z') &= E_{hi}\frac{i^{n'+1}\exp(-in'\phi_i)}{k_{i\rho}}\delta(k_z'-k_{iz}) \\
a_{n'}^{EN}(k_z') &= E_{vi}\frac{i^{n'+2}\exp(-in'\phi_i)}{k_{i\rho}}\delta(k_z'-k_{iz})
\end{aligned}
\tag{4.11}
$$

where δ is the Dirac delta function. Substitutions of (4.11) into (4.5) and (4.6) and the cancelation of integration over k_z' with the delta function give

$$
a_n^{SM}(k_z,k_{z_i}') = \sum_{n'}\left[E_{hi}T_{nn'}^{MM'}(k_z,k_{zi}') + iE_{vi}T_{nn'}^{MN'}(k_z,k_{zi}')\right]\frac{i^{n'+1}}{k_{i\rho}}\exp(-in'\phi_i) \tag{4.12}
$$

$$
a_n^{SN}(k_z,k_{zi}') = \sum_{n'}\left[E_{hi}T_{nn'}^{NM'}(k_z,k_{zi}') + iE_{vi}T_{nn'}^{NN'}(k_z,k_{zi}')\right]\frac{i^{n'+1}}{k_{i\rho}}\exp(-in'\phi_i) \tag{4.13}
$$

By applying an H-pol ($E_{vi}=0, E_{hi}=1$) and a V-pol ($E_{vi}=1, E_{hi}=0$) plane wave, respectively, to (4.12) and (4.13), we get 4 set of equations that relate the T-matrix element to the scattering field coefficient

$$
\begin{aligned}
a_{n,h}^{SM}\left(k_z,k_{z_i}'\right) &= \sum_{n'}E_{hi}T_{nn'}^{MM}\left(k_z,k_{zi}'\right)\frac{i^{n'+1}}{k_{i\rho}}\exp\left(-in'\phi_i\right) \\
a_{n,h}^{SN}\left(k_z,k_{z_i}'\right) &= \sum_{n'}E_{hi}T_{nn'}^{NM}\left(k_z,k_{zi}'\right)\frac{i^{n'+1}}{k_{i\rho}}\exp\left(-in'\phi_i\right) \\
a_{n,v}^{SM}\left(k_z,k_{z_i}'\right) &= \sum_{n'}iE_{vi}T_{nn'}^{MN'}\left(k_z,k_{zi}'\right)\frac{i^{n'+1}}{k_{i\rho}}\exp\left(-in'\phi_i\right) \\
a_{n,v}^{SN}\left(k_z,k_{z_i}'\right) &= \sum_{n'}iE_{vi}T_{nn'}^{NN'}\left(k_z,k_{zi}'\right)\frac{i^{n'+1}}{k_{i\rho}}\exp\left(-in'\phi_i\right)
\end{aligned}
\tag{4.14}
$$

where the polarization of the excitation field is indicated by the subscript v and h. Note that the two cylindrical waves $\bar{M}_n(k_z,r)$ and $\bar{N}_n(k_z,r)$ are actually corresponding to the H-pol and V-pol respectively. By combining the notation together, (4.14) can be written in a compact form as

$$
a_{n,\beta'}^{S\beta}(k_z,k_{z_i}') = \sum_{n'}E_{\beta'}C_{\beta'}T_{nn'}^{\beta\beta'}(k_z,k_{zi}')\frac{i^{n'+1}}{k_{i\rho}}\exp(-in'\phi_i) \tag{4.15}
$$

where $\beta = M, N$ denotes the polarization, the prime superscript indicates the source, and $C_{\beta'} = i$, when $\beta' = N$ (V-pol), $C_{\beta'} = 1$, when $\beta' = M$ (H-pol). Equation (4.15) reveals that the T-matrix element of $T_{nn'}^{\beta\beta'}(k_z, k'_{zi})$ is the coefficient of the Fourier series of plane wave scattered field coefficient $\alpha_{n,\beta'}^{S\beta}(k_z, k'_{zi})$ in terms of ϕ_i. Multiplying both sides with $\int d\phi_i \exp(in'\phi_i)$ and using the orthogonality of the exponential function,

$$\int d\phi \exp(in\phi_i) \exp(in'\phi_i) = 2\pi\delta_{nn'} \tag{4.16}$$

the T-matrix can be calculated using the scattered field coefficient from

$$T_{nn'}^{\beta\beta'}(k_z, k'_{zi}) = \frac{k_{i\rho}}{2\pi} \frac{i^{-(n'+1)}}{E_{\beta'} C_{\beta'}} \int_0^{2\pi} a_{n,\beta'}^{S\beta}(k_z) \exp(in'\phi_i) d\phi_i. \tag{4.17}$$

The significance of (4.17) is that it enable us to compute the T-matrix element by element and removes the inherent constrain set by the matrix inversion-based approach for calculating the T-matrix.

4.3.2 Far-field Based T-matrix Extraction

It is important to notice that the expansion coefficients in (4.1) are independent of distance. Given the $a_n^{S\beta}(k_z)$, the corresponding scattered field are known regardless of the distance. Conversely, $a_n^{S\beta}(k_z)$ can be obtained either from the near-field or the far-field. The near-field based approach for calculating the $a_n^{S\beta}(k_z)$ using the Huygens principle and the VCW expansions of the Dyadic Green's function has been presented in Chapter 2. The far-field based method for extracting the T-matrix will be presented here.

In the far-field region, the Hankel function can be approximated as

$$\begin{aligned} \lim_{z\to\infty} H_n^{(1)}(z) &\approx \sqrt{\frac{2}{\pi z}} \exp(i(z - \frac{n\pi}{2} - \frac{\pi}{4})) \\ \lim_{z\to\infty} H_n^{(1)}(z) &\approx i\sqrt{\frac{2}{\pi z}} \exp(i(z - \frac{n\pi}{2} - \frac{\pi}{4})) \end{aligned} \tag{4.18}$$

Substitute (4.18) into (4.2) and (4.3), we can get the far-field approximations of the VCW

$$\lim_{\rho\to\infty} \bar{M}_n(k_z,\bar{r}) = -\hat{\phi} i k_\rho \sqrt{\frac{2}{\pi k_\rho \rho}} \exp(i(k_\rho\rho - \frac{n\pi}{2} - \frac{\pi}{4})) \exp(ik_z z) \exp(in\phi) \tag{4.19}$$

$$\lim_{\rho\to\infty} \bar{N}_n(k_z,\bar{r}) = \Big[-\hat{\rho}\frac{k_\rho k_z}{k} + \hat{z}\frac{k_\rho^2}{k} \Big] \sqrt{\frac{2}{\pi k_\rho \rho}} \exp(i(k_\rho\rho - \frac{n\pi}{2} - \frac{\pi}{4})) \exp(ik_z z) \exp(in\phi) \tag{4.20}$$

where the $\bar{M}_n(k_z,\bar{r})$ only has $\hat{\phi}$ component and the $\bar{N}_n(k_z,\bar{r})$ has $\hat{\rho}$ and $\hat{z}$ component. With the far-field approximations, the scattered field in the far-field region becomes

$$\begin{aligned} \bar{E}^s(r) = \sum_n \int dk_z \Big[a_n^{SM}(k_z)(-\hat{\phi}k_\rho i) + a_n^{SN}(k_z)([-\hat{\rho}k_z + \hat{z}k_\rho]\frac{k_\rho}{k}) \Big] \\ \times \sqrt{\frac{2}{\pi k_\rho \rho}} \exp(i(k_\rho\rho - \frac{n\pi}{2} - \frac{\pi}{4})) \exp(ik_z z) \exp(in\phi). \end{aligned} \tag{4.21}$$

By applying the stationary phase approximation to (4.21), the far-field can be simplified as

$$\begin{aligned} \bar{E}^s(r) = \sum_n \Big[a_n^{SN}(k\cos\theta)([-\hat{\rho}\cos\theta + \hat{z}\sin\theta]k\sin\theta) + a_n^{SM}(k\cos\theta)(-i\hat{\phi}k\sin\theta) \Big] \\ \times \exp(in\phi) i^{-n} \int dk_z \sqrt{\frac{2}{\pi k_\rho \rho}} \exp(i(k_\rho\rho - \frac{\pi}{4})) \exp(ik_z z). \end{aligned} \tag{4.22}$$

The detailed derivation of the stationary phase approximation can be found in the Appendix 4.A. Note that $\hat{\phi} = \hat{h}$ and $\hat{v} = \hat{\rho}\cos\theta - \hat{z}\sin\theta$, the scattered far-field become

$$\begin{aligned} \bar{E}^s(r) = -k\sin\theta \sum_n \exp(in\phi) \Big[(i\hat{h}) a_n^{SM}(k\cos\theta) + (\hat{v}) a_n^{SN}(k\cos\theta) \Big] \\ \times i^{-n} \int dk_z \sqrt{\frac{2}{\pi k_\rho \rho}} \exp\Big(i\Big(k_\rho\rho - \frac{\pi}{4} \Big) \Big) \exp(ik_z z) \end{aligned} \tag{4.23}$$

It is also notice that the last term in (4.23) is the far-field approximation of the free the space

Green's function which is known as

$$\frac{\exp(ikr)}{r} = \frac{i}{2}\lim_{\rho\to\infty}\int dk_z \sqrt{\frac{2}{\pi k_\rho \rho}}\exp(i(k_\rho\rho - \frac{\pi}{4}))\exp(ik_z z). \tag{4.24}$$

The detailed derivation of (4.24) can be found in the Appendix 4.B. Using (4.24), the far-field is related to the VCW coefficient through

$$\bar{E}_s(r) = \frac{\exp(ikr)}{r} 2k\sin\theta \sum_n i^{1-n}\exp(in\phi)\left[a_n^{SM}(k\cos\theta)(i)\hat{h} + a_n^{SN}(k\cos\theta)\hat{v}\right] \tag{4.25}$$

In the far field, the scattered field is related to the incident field through the scattering amplitude $f_{\beta\beta'}(k_s, k_i)$

$$\begin{bmatrix} E_{vs} \\ E_{hs} \end{bmatrix} = \frac{\exp(ikr)}{r} \begin{bmatrix} f_{vv}(k_s,k_i) & f_{vh}(k_s,k_i) \\ f_{hv}(k_z,k_i) & f_{hh}(k_s,k_i) \end{bmatrix} \begin{bmatrix} E_{vi} \\ E_{hi} \end{bmatrix} \tag{4.26}$$

By equating (4.23) and (4.26), the scattered field coefficients are related to the far-field amplitude

$$\begin{aligned} 2k\sin\theta\sum_n i^{1-n}\exp(in\phi)\, a_n^{SN}(k\cos\theta) &= f_{vv}(k_s,k_i)\,E_{vi} + f_{vh}(k_s,k_i)\,E_{hi} \\ 2k\sin\theta\sum_n i^{1-n}\exp(in\phi)\, a_n^{SM}(k\cos\theta)(i) &= f_{hv}(k_s,k_i)\,E_{vi} + f_{hh}(k_s,k_i)\,E_{hi} \end{aligned} \tag{4.27}$$

Applying an H-pol ($E_{vi} = 0, E_{hi} = 1$) and a V-pol ($E_{vi} = 1, E_{hi} = 0$) plane wave excitation to (4.27), and integrating both side with $\exp(in\phi)$, we can obtain

$$\begin{aligned} a_{n,h}^{SN}(k\cos\theta) &= \frac{1}{4\pi k\sin\theta i^{1-n}}\int d\phi\exp(-in\phi)f_{vh}(\phi,\theta) \\ a_{n,h}^{SM}(k\cos\theta) &= \frac{1}{4\pi k\sin\theta i^{2-n}}\int d\phi\exp(-in\phi)f_{hh}(\phi,\theta) \\ a_{n,v}^{SN}(k\cos\theta) &= \frac{1}{4\pi k\sin\theta i^{1-n}}\int d\phi\exp(-in\phi)f_{vv}(\phi,\theta) \\ a_{n,v}^{SM}(k\cos\theta) &= \frac{1}{4\pi k\sin\theta i^{2-n}}\int d\phi\exp(-in\phi)f_{hv}(\phi,\theta) \end{aligned} \tag{4.28}$$

Similarly, (4.28) can be expressed in a compact form as

$$a_{n,\beta'}^{S\beta}(k\cos\theta) = \frac{1}{4\pi k\sin\theta i^{1-n}C_\beta}\int d\phi\exp(-in\phi)f_{\beta\beta'}(\phi,\theta) \tag{4.29}$$

where $C_\beta = 1$, when $\beta = N$ (V-pol), $C_\beta = i$, when $\beta = M$ (H-pol). This states that the scattered field coefficient is the coefficient of Fourier series of the far-field in term of ϕ. Combination of (4.15) and (4.29) gives

$$T_{nn'}^{\beta\beta'}(k_z,k'_{zi}) = \frac{1}{i^{n'-n}C_\beta C_{\beta'}}\frac{1}{8\pi^2}\frac{\sin\theta_i}{\sin\theta}\int_0^{2\pi}d\phi e^{-in\phi}\int_0^{2\pi}d\phi_i e^{in'\phi_i}f_{\beta\beta'}(k_s,k_i) \tag{4.30}$$

It indicates that the T-matrix elements are the Fourier coefficients of the double Fourier series of the far-field in terms of ϕ and ϕ_i. With (4.30), we can calculate the T-matrix element-wisely by using the far-field amplitudes. Since the far-field are always directly available in the most of the commercial solver and do not require the surface integration to obtain the scattered field coefficient, thus the far-field approach is more efficient than the near-field based approach.

4.3.3 Iterative Solution of FL Equations

The second step of the hybrid method is to combine the T-matrix with the FLE to consider the multiple scattering among different trees through

$$\bar{E}_q^{ex}(\bar{r}) = \bar{E}_q^{inc}(\bar{r}) + \sum_{p=1,p\neq q}^{N_t}\bar{G}_{qp}\overline{\overline{T}}_p\bar{E}_p^{ex}(\bar{r}) \tag{4.31}$$

where N_t is the number of trees, $\bar{G}_{qp}$ is the free space green function representing the propagation from tree p to q, and the $\bar{E}_q^{ex}(\bar{r})$ denotes the final excitation acting on the qth tree. The FLE states that the final excitation field $\bar{E}_q^{ex}(\bar{r})$ acting on the qth tree is the incident field plus the final scattered field $\bar{E}_p^{sc}(\bar{r})$ of all other trees except itself. In (4.31), the final scattered field is expressed in terms of T-matrix as $\bar{E}_p^{sc}(\bar{r}) = \overline{\overline{T}}_p E_p^{ex}(\bar{r})$ and thus a self-consistent equation is formed with the $\bar{E}_p^{ex}(\bar{r})$ being the only unknown.

By using the VCW expansions and the translational addition theorem, a set of linear equations are obtained for solving the final unknown excitation coefficients. Previously, the closed-form equations are solved directly using the numerical method of GMRES to obtain the final solution. However, this becomes impractical for forest simulation as the number of unknowns is on the order of $O(N_t^2 N_T^2)$, where N_T is the number of modes used in the T-matrix. To avoid the memory challenge, the FLE can be solved iteratively based on the physical scattering process such that we do not need to store the FLE matrix. The iterative process starts from the first order scattered field which is excited by the incident field only and can be obtained from

$$\bar{E}_q^{s(1)}(\bar{r}) = \overline{\overline{T}}_q \bar{E}^{inc}(\bar{r}) \tag{4.32}$$

where the order in the superscript indicates the number of time that the field is scattered. The higher order scattered field is then obtained from the lower order using the recurrent iteration

$$\bar{E}_q^{s(n)}(\bar{r}) = \overline{\overline{T}}_q \sum_{p=1, p\neq q}^{N_t} \overline{\overline{G}}_{qp} \bar{E}_p^{s(n-1)}(\bar{r}) \tag{4.33}$$

which states that the total exciting field acting on qth scatterer is the sum of the $(n-1)th$ scattered field from all other scatterer. The scattered field will decay as the order increase and the iteration can be terminated when the higher order scattered field is negligible. The total scattered field is then calculated from

$$\bar{E}^s(\bar{r}) = \sum_q^{N_t} \sum_n^{N_{it}} \bar{E}_q^{s(n)}(\bar{r}) \tag{4.34}$$

where N_{it} is the total number of the physical iteration. The iterative solution is preferable when the density of the scatterer is small and the solution will converge in a few iterations as we will show in the result section.

4.3.4 Inner Field Extraction

It is important to notice that the T-matrix is only valid for scattered field in the outer region and thus can not be applied to compute the inner region scattered field. The scattered field of each plant in its inner region can be obtained using the plane wave transformation and the superposition principle. The solutions solved from the FLE express the final excitation field acting on each scatterer in terms of VCW. Using the plane wave expansion of the VCW which are known as

$$Rg\bar{M}_n(k_z,\bar{r}) = \frac{k_\rho}{2\pi i^{n+1}} \int d\phi_k \exp(i\bar{k}\cdot\bar{r})\hat{h}(\theta_k,\phi_k)\exp(in\phi_k) \tag{4.35}$$

$$Rg\bar{N}_n(k_z,\bar{r}) = \frac{k_\rho}{2\pi i^{n+2}} \int d\phi_k \exp(i\bar{k}\cdot\bar{r})\hat{v}(\theta_k,\phi_k)\exp(in\phi_k) \tag{4.36}$$

we can transform (4.1) into

$$\bar{E}^{ex}(\bar{r}) = \int dk_z \int d\phi_k \Big[C_h(\theta_k,\phi_k)\hat{h}(\theta_k,\phi_k) + C_v\left(\theta_k,\phi_k\right)\hat{v}\left(\theta_k,\phi_k\right)\Big]\exp(in\phi_k)\exp(i\bar{k}\cdot\bar{r}) \tag{4.37}$$

which expresses the final excitation field as a linear combination of the plane wave from different angle (θ_k,ϕ_k), C_h and C_v are the corresponding plane wave coefficients and they are related to the VCW coefficients as

$$C_h\left(\theta_k,\phi_k\right) = \sum_n a_n^{EM}\left(k_z\right)\left(\frac{k_\rho}{2\pi i^{n+1}}\right) \tag{4.38}$$

$$C_v\left(\theta_k,\phi_k\right) = \sum_n a_n^{EN}\left(k_z\right)\left(\frac{k_\rho}{2\pi i^{n+2}}\right) \tag{4.39}$$

Using the linearlity of the electromagnetic field and the supperposition principle, the corresponding inner region scattered field excited by (4.37) can be obtained from

$$\bar{E}^s_{q,in}(\bar{r}) = \int dk_z \int d\phi_k C_\beta(\theta_k,\phi_k)\bar{E}^{s,\beta}_{q,in}(\bar{r}) \tag{4.40}$$

where $\bar{E}^{s,\beta}_{q,in}(\bar{r})$ is the scattered field of the tree excited by the β-pol plane wave from (θ_k, ϕ_k) and are already computed in the first step when calculating the T-matrix. By using the T-matrix and (4.40), the scattered field in both the inner and outer regions can be obtained which is important for calculating the microwave transmission.

4.4 Method Validation

In this section, we validate the far-field based approach by calculating the T-matrix of a eight meters tall tree and the accuracy of the hybrid method is tested with FEKO by solving the scattering from three eight meters tall trees. The excitation field is a vertically (V-pol) or horizontally (H-pol) polarized plane wave from the direction of $\phi_i = 0^o, \theta_i = 40^o$, at L-band 1.41 GHz, which is the operation frequency and the incident angle of NASA Soil Moisture Active Passive (SMAP) mission [6]. Three type of components, the trunk, the primary and secondary branches, are considered in the tree model. Their sizes and numbers are listed in Table 4.4.1. While the trunk is a vertical cylinder, the orientation angles $(\phi_{B_1}, \theta_{B_1})$ of the primary branches are randomly generated with a uniform distribution of $\phi_{B_1} \in [0^o, 360^o]$ and $\theta_{B_1} \in [0^o, 90^o]$. Three eight meters tall trees generated based on these parameters are shown in Fig.4.4.3.

Table 4.4.1: Size and number of tree components: trunk (Tr), primary branch (B_1), and secondary branch (B_2)

Tree	2m			5m			8m		
	Tr	B_1	B_2	Tr	B_1	B_2	Tr	B_1	B_2
Num.	1	12	72	1	15	90	1	18	108
Len. (m)	2	0.3	0.2	5	0.8	0.2	8	1.0	0.3
Dia. (cm)	10	4.0	1.0	16	4.0	1.0	25	4.0	1.0

4.4.1 T-matrix of Single Tree

First, we perform full-wave simulations of a eight meters tall tree using the FEKO to obtain the scattered far-field from which the corresponding T-matrix is calculated using (4.30). The VCW based T-matrix has two free variables n and k_z which range from $-\infty$ to $+\infty$ in theory. In practise, they are truncated at a maximum value that ensures the convergence of the scattered field. The maximum number of mode in the $\hat{\phi}$ direction is related to the R_c as $N_n^{max} = 2kR_c$. The continuous integration over k_z is truncated at k_z^{max} and is approximated using a N_θ uniform sampling within $[-k_z^{max}, k_z^{max}]$. In this paper, the T-matrix only consider propagating waves as the evanescent waves are negligible so $k_z^{max} = k_0$. The N_θ is chose based on the convergence test. Consequently, the total number of mode used in the T-matrix is $N_m = 2(2kR_c + 1)N_\theta$. The far-field based T-matrix (4.30) requires a continuous integration over ϕ_i which is very expensive as it needs the full-wave simulation for each sampled ϕ_i. To improve the simulation efficiency, the Legendre quadrature is applied to the ϕ_i integration and the resulting number of sampling is $N_{\phi_i} = 2n'$ which is 5 time less than $10n'$ which is the sampling number required by a uniform sampling.

To justify the truncation we made in the number of modes and validate the accuracy of the T-matrix, the scattered field of an eight meters tall tree on a vertical z-line on the enclosing cylinder is plotted in Fig. 4.4.1(a). We can see despite a small mismatch on one of the peak that caused by the sharp scattering from branch, the scattered field obtained from the T-matrix agree very closely with the FEKO solution. As the evanescent waves are largely caused by the tree trunk and decay exponentially in the $\hat{\rho}$ direction, so they are negligible on the enclosing cylindrical surface where $\rho = 1m$ and is about 4λ away from the trunk. That is the reason why we can exclude the evanescent waves in the T-matrix. The scattered field over a horizontal x-line is also plotted in Fig. 4.4.1(b) which shows that the scattered field decay as ρ increases. This imply that when the separate distance between two trees is greater than a certain value ρ_{max}, their interactions are negligible. Consequently, the area of the forest stand to be simulated can be truncated at $R = \rho_{max}$. That is the reason for the simulated forest stand is circular area of radius $R = 8m$. The good agreements of the field solutions validate the accuracy of the far-field based T-matrix.

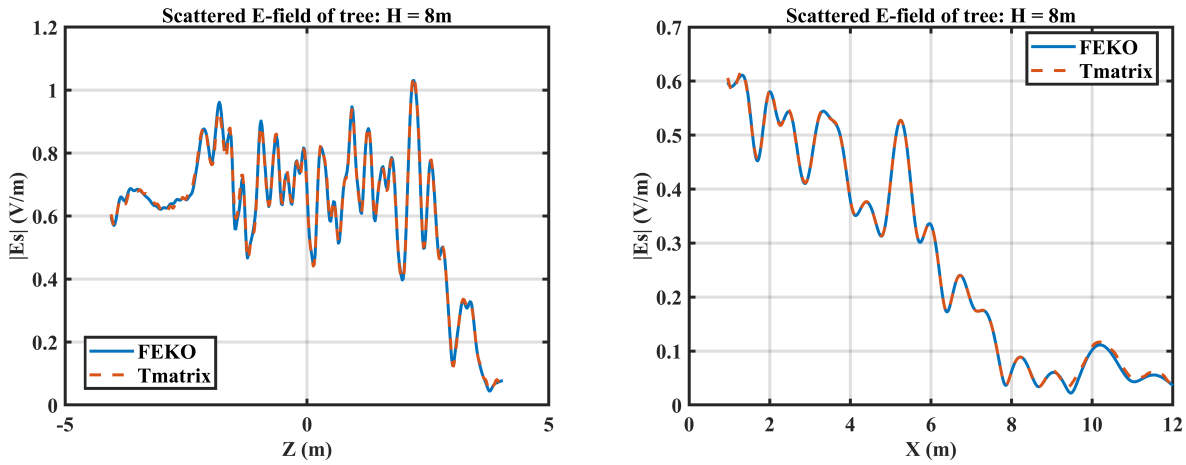

(a) (b)

Figure 4.4.1: Amplitudes of scattered E-field of a single eight meters tall tree at L-band excited by a 40^o incident V-pol plane wave on (a) a vertical z-line with $x = 1m$ and $y = 0m$, and (b) a horizontal x-line with $z = -4.05m$ and $y = 0m$.

To demonstrate the multiple scattering effects caused by the tree structure, we also plot the scattered field of the trunk only tree in Fig. 4.4.2 using both the FEKO and the ICA based T-matrix. Since the tree is eight meters tall and much larger than the wave length at L-band which is $\lambda = 0.21m$, the ICA approximation generally has a good agreement with the full-wave results obtained from the FEKO. The difference between the ICA and FEKO are caused by the exclusion of the top and bottom surface of the cylinder in the ICA. That is why the ICA works poorer at the two end than in the middle of the trunk. In Fig. 4.4.2(a), the scattered field vary smoothly along the vertical line as there is no multiple scattering of one single trunk. In contrast, the field in Fig. 4.4.1(a) fluctuate rapidly as there are strong multiple scattering among the trunk and branches within the same tree. By comparing the field plotted in Fig. 4.4.1(b) and 4.4.2(b), we can see the multiple scattering due to the tree structure also change the scattered field at the bottom plane which has a direct impact on calculating the microwave transmissivity. Moreover, the strong field fluctuation will also affect the field distribution in the tree such that impact the absorption of the tree. In the next section, forest of the trunk only tree will also be simulated to further investigate the impact of the tree structure on the microwave transmissivity.

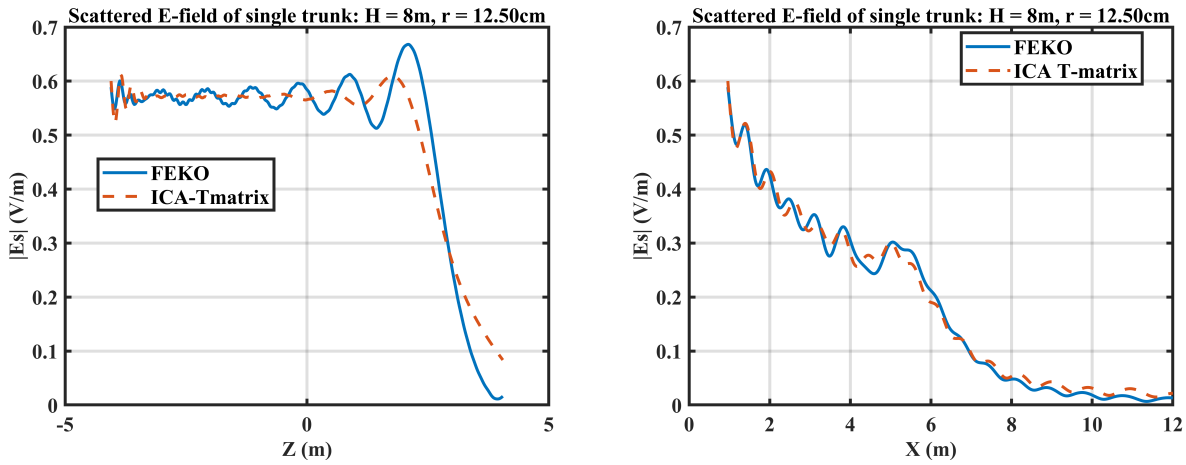

(a) (b)

Figure 4.4.2: Amplitudes of scattered E-field of a single eight meters tall trunk at L-band excited by a 40^o incident V-pol plane wave on (a) a vertical z-line with $x = 1m$ and $y = 0m$, and (b) a horizontal x-line with $z = -4.05m$ and $y = 0m$.

4.4.2 Full-wave Simulation of 3 Trees at L-band

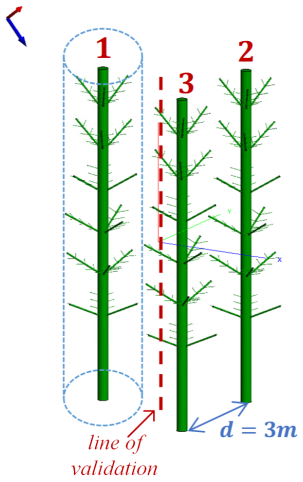

Figure 4.4.3: Scattering from three eight meters tall trees are solved using the hybrid method and the FEKO, the radius of the circumscribing cylinder $R_c = 1.0m$, distance between the centers of 2 circumscribing cylinders $d = 3.0m$.

Second, we validate the iterative solutions of the FLE by solving the scattering from three eight meters tall trees as shown in Fig.4.4.3. The iterative solutions of the scattered E-field along the z-axis from $-4m$ to $4m$ are plotted in Fig. 4.4.4(a). The amplitude of the scattered field decreases dramatically with the order of scattering and is on the order of 10^{-6} at the 10-th iteration. Thus the

iterative process can be terminated at $N_{it} = 10$. The hybrid method solutions are obtained by summing up the 10 order of solutions and are compared with the FKEO solutions in Fig. 4.4.4(b). The good agreements of the near-field solutions validate the accuracy of the physical iterative method. The fast convergence is achieved because the density of the scatterer is small and more iterations may require for a larger number of scatterer. Since the hybrid method treats each single tree composed of many components, rather than a individual branch or trunk, as a individual scatterer and the typical density of tree ρ_t in the forest is within $[0.07, 0.15]$, so the number of scatterer is always small. For example, the number of tree within a circular area of $R = 8m$ with $\rho_t = 0.15$ is 30, which is much smaller than that of the crop. Thus a fast convergence can always be achieved by the physical iterative process when simulating the forest.

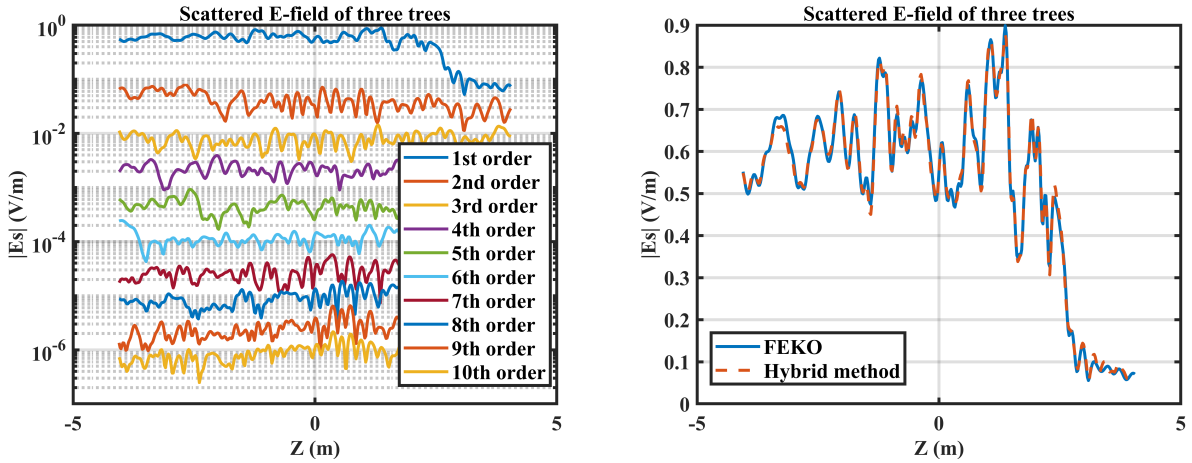

(a) (b)

Figure 4.4.4: (a) Iterative solutions of Foldy-Lax equations of scattering from three eight meters tall trees and (b) Scattered field of three eight meters tall trees along the z-axis range from $-4m$ to $4m$.

The field on the plane 5 cm below the tree calculated from the two methods are also plotted in Fig.4.4.5. Despite a small discontinuity between the fields in the inner and the outer regions, the hybrid method results match well with those calculated from the FEKO which validates the wave transformation approach for extracting the inner region field. Moreover, the coherent wave approach enables the hybrid method to model the field variations caused by the multiple scattering due to both the tree structures and spatial variations of the tree positions. Consequently, the non-

uniform transmission within the forest can be captured and is much more accurate than the classical incoherent RTE which can only uses a constant τ to characterize the wave propagation.

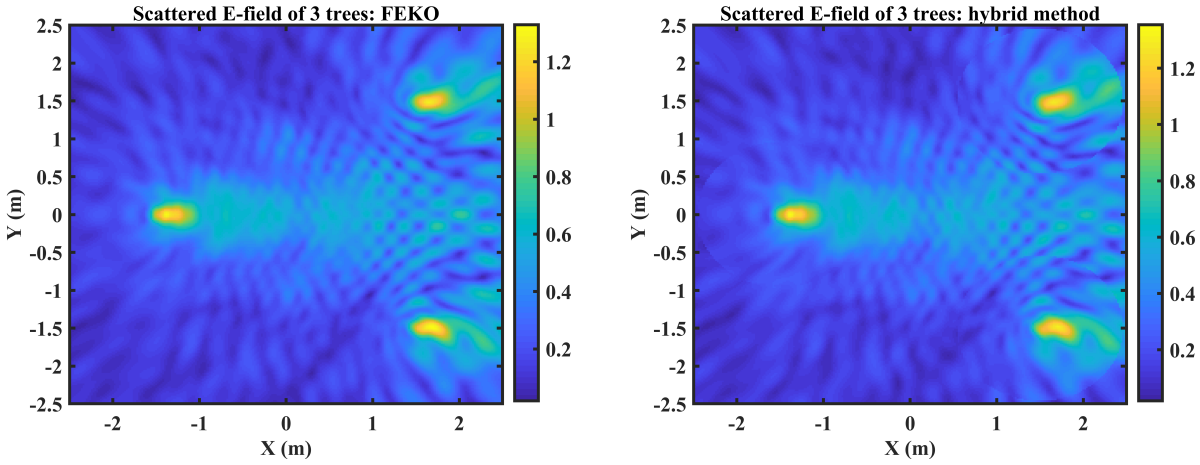

(a) (b)

Figure 4.4.5: Amplitude of scattered E-field at L-band excited by a 40^o incident V-pol plane wave on a plane $5cm$ below the 3 trees solved from (a) the FEKO and (b) the hybrid method.

4.5 Full-wave Simulation of Forest

In this section, we apply the hybrid method to investigate the microwave transmissivity at L-band over the forested area by performing full-wave Monte Carlo simulations of a 200 m^2 large forest stand with different tree densities and tree heights. The top view of the forest is shown in Fig. 4.2.2 with a radius $R = 8m$. The T-matrix of a single tree is first calculated based on the full-wave solutions obtained from the FKEO. The T-matrix is stored and can be repeatedly used in different realizations of the Monte Carlo simulation. Te reusability of the T-matrix is an important advantage of the hybrid method. For each realization, the positions of the trees are randomly generated within the circular area to form a different forest. Based on that, the hybrid method is applied to perform the full-wave simulation. Then the transmissivity of the microwave is obtained by calculating the normalized transmitted power over a reception area through

$$T = \frac{1}{A}\iint_A \frac{\bar{S}^{tot}(\bar{r})\cdot(-\hat{z})}{\bar{S}^{inc}(\bar{r})\cdot(-\hat{z})}d\bar{r} \tag{4.41}$$

where $\bar{S}$ is the Poynting vector and A is a square reception area of size l_x at the bottom of the forest as shown in Fig.4.2.2. The final transmissivity is obtained by the ensemble average over T computed from N_r realizations using

$$t = \frac{1}{N_r} \sum_{i=1}^{N_r} T_i \tag{4.42}$$

In the following, we first perform the convergence tests to determine the numerical parameters of the size of reception area l_x and the number of realization N_r. After that, we will apply the hybrid method to study the effects of the tree height and the tree density on the microwave transmission in the forested area.

4.5.1 Convergence Test

Wave propagation in the forest is a random scattering process and the microwave transmissivity T is a random variable. In microwave remote sensing application, only the mean value of T is of interest and is studied based on the Monte Carlo simulations. Generally, the randomness of T is proportional to the tree height, thus the convergence tests are performed over the tallest forest (H=8m) considered in this paper to determine the numerical parameters of l_x and N_r.

We first test convergence of transmissivity over the size of the reception area A. The T as defined in (3.21) is a normalized value that will converge to a value for a large enough area A. Since a limited size of forest is simulated, the reception area is thus located at the center region as shown in Fig. 4.2.2 to avoid the edge effects caused by the truncation of the forest. The L-band transmissivitive of the eight meters tall forest vary with A are plotted in Fig. 4.5.1. We can see the t of different tree densities converge as the area increases indicating that the simulated area is large enough to obtain a converged transmisivity. Considering that we need to minimize the edge effect, it is preferable to keep A as small as possible while maintaining the convergence of t. Thus the size of the reception area is chose to be $A = 4m^2$ and the corresponding size is $l_x = 2m$.

Next we carry out the convergence tests of t over the number of realization N_r. The transmis-

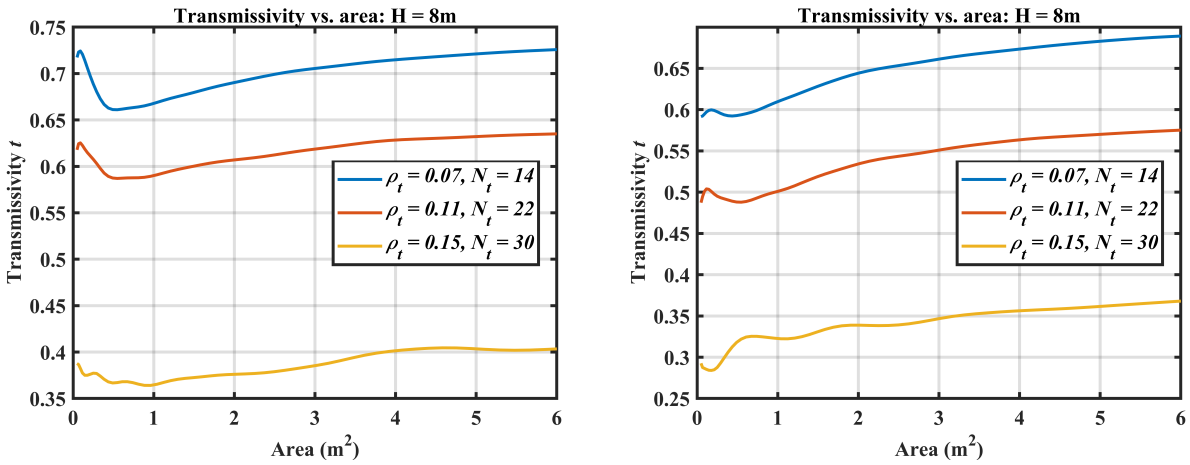

Figure 4.5.1: Convergence tests of the L-band transmissivities t over the size of reception area A for different tree densities (a) H-pol and (b) V-pol.

sivities of 3 different tree densities are plotted against with N_r in Fig. 4.5.2. While the t of the two sparser case converge at $N_r = 10$, it takes 7 more realizations for the denser case to converge. This make sense as a denser forest has stronger multiple scattering, thus result a larger fluctuation on T between different realizations. Consequently, it requires more realizations for a denser forest to obtain the converged t. To demonstrate the importance of selecting the reception area, we also plot the t obtained from 3 different reception area vary with N_r in Fig. 4.5.3. We can see the t based on a larger reception area has a smaller fluctuation. Because T as defined in (4.41) is normalized value and will converge to a large enough reception area. In Monte Carlo simulations, the T is obtained by averaging transmissivity over N_r realizations of area l_x^2. Then the total area used in computing T is $A = N_r l_x^2$. Thus if a larger reception area l_x^2 is used in each realization, then fewer realizations are needed for obtaining the converged results which is demonstrated by results shown in Fig. 4.5.3. Based on the testing results, the number of realization used in the following simulations is $N_r = 20$.

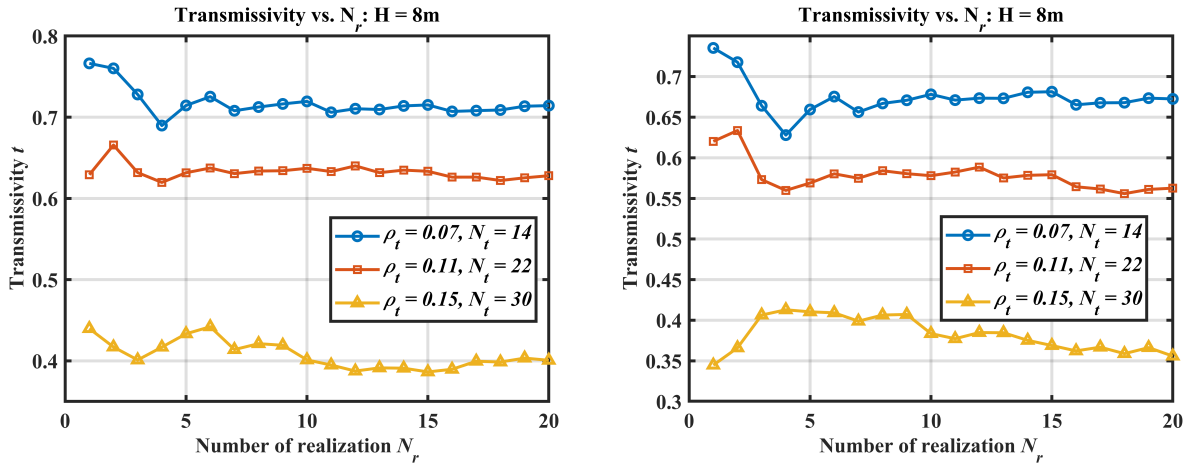

(a) (b)

Figure 4.5.2: Convergence tests of the L-band transmissivities t over the number of realization N_r for different tree densities (a) H-pol and (b) V-pol.

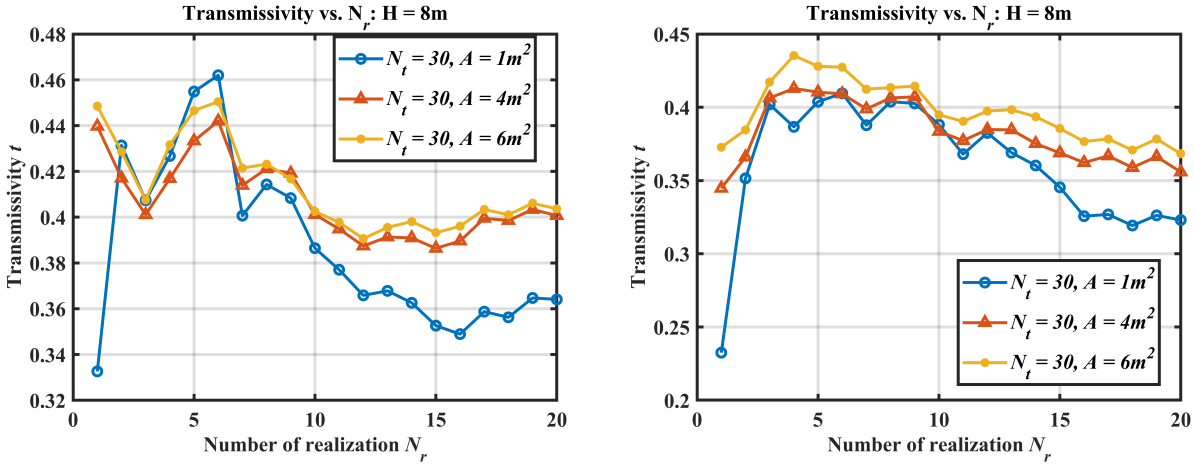

(a) (b)

Figure 4.5.3: Convergence tests of the L-band transmissivities t over the number of realization N_r for different size of reception area (a) H-pol and (b) V-pol.

4.5.2 Transmissivity vs. Tree Height

After determining the numerical parameters, we perform Monte Carlo simulations of forests with three different heights to investigate its impact on the microwave transmissitivty. The positions of the trees are generated based on the eight meters tall tree and the same positions are used for forest of three different heights as listed in the Table 4.4.1. To demonstrate the importance of full-wave simulation, the transmissivities are compared with those calculated from the RTE using

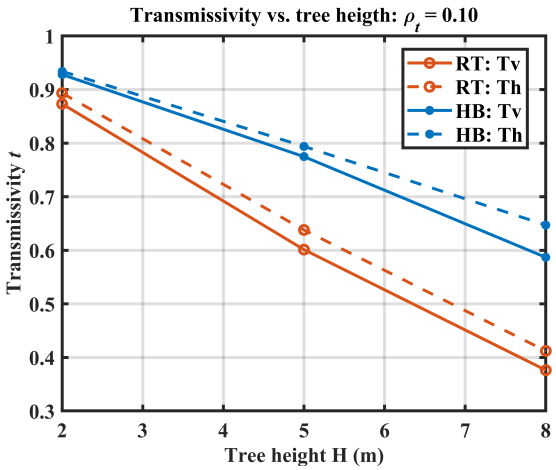

Figure 4.5.4: The L-band microwave transmissivities at forested area with tree density of $\rho_t = 0.10$ vary with tree height.

the same parameters. In RTE, the positions of the scatterers within the forest are assumed to be statistical homogeneous in space. Thus the forest canopy is approximated as a layered medium and the transmissivity is estimated from

$$t_R = \exp(-\kappa_e sec(\theta_i) d) \tag{4.43}$$

where d is the thickness of the vegetation layer, θ_i is the incident angle, and κ_e is the effective extinction coefficient. The κ_e describes the power attenuation rate per unit distance in the forest. The expression for extinction coefficient is

$$\kappa_e = \sum_j n_j^0 \Big(\langle \sigma_j^a \rangle + \langle \sigma_j^s \rangle \Big) \tag{4.44}$$

where n_j^0 is number of j-th component per m^3, σ_j^s and σ_i^a are the corresponding scattering and absorption cross sections, and $\langle \cdot \rangle$ is the ensemble average on the orientation angle (θ_j^c, ϕ_j^c). Since all the components are modelled as dielectric cylinders, their σ_j^s and σ_j^a are calculated analytically based on the ICA using the optical theorem [37]. The transmissivities of different tree height calculated from the two methods including both the V-pol and H-pol results are plotted in Fig.4.5.4. While a similar trend that t decreases with H is observed for both methods, the hybrid method

results are much larger than those of RTE. For instance, the full-wave based V-pol transmissivity for eight meters tall forest is about 0.59 which is 55% higher than 0.38 predicted by the RTE. As the approximations made in the RTE become more erroneous as the tree height increase, their difference also becomes larger as tree becomes higher.

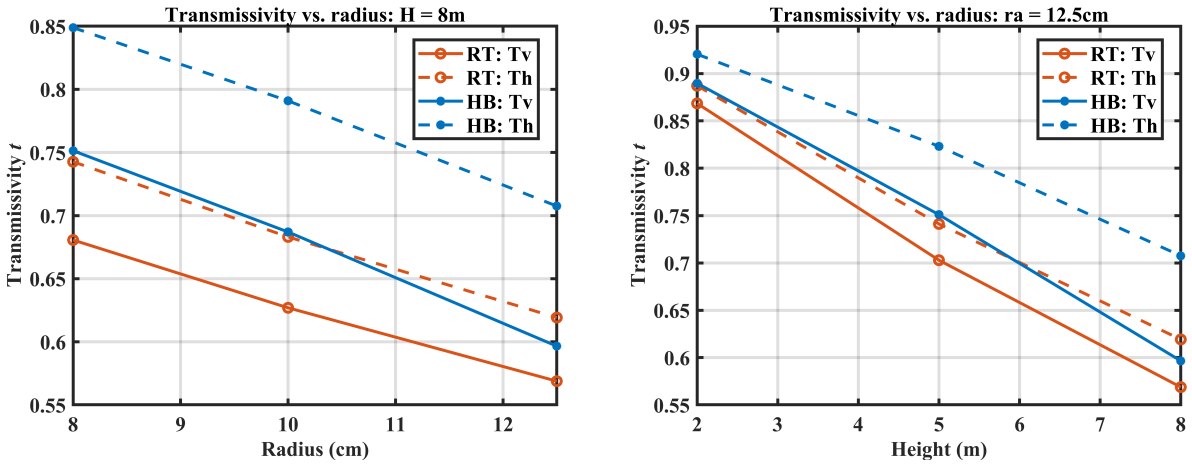

(a) (b)

Figure 4.5.5: The L-band microwave transmissivities of trunk only forest change with the (a) radius of tree trunk and (b) height of tree trunk.

The absorption caused by the vegetation layer are mainly due to the water contained in the vegetation and most of the water in a tree are stored in the tree trunk. Thus it is of interest to study the impact of the size of the tree trunk. In the previous simulations, the radius of tree trunk increases with tree height so we can not separate their impacts on the microwave transmissivity. In the following, we simulate forest with trunk only tree to investigate how the radius and height of tree trunk change the t. The T-matrix is obtained from the ICA approximation. Fig. 4.5.5(a) plots transmissivity as a function of the radius including both the full-wave and RT based results. We can see the hybrid method results are greater than those of the RT which is consistent with our previous observation. The full-wave based t also show a higher sensitivity to the change of the radius as there is 15 percents change in the full-wave calculated V-pol t when the radius increases from $8cm$ to $12.5cm$, while the change in RT based t is 10 percents. The transmissivity versus tree height with $r_a = 12.5cm$ are plotted in Fig. 4.5.5(b). We can see the the difference between t calculated

from the two method for 8m tall case are much smaller than that of in Fig. 4.5.4. This indicates that the exclusion of the branches in the RTE model significantly increase the transmissivity, while the hybrid method gives the similar results. These results show that both the radius and height of tree trunk has a significant impact on the t, which demonstrates that the absorption are closely related to the volume or the size of the tree trunk. This is consistent with the fact that the microwave transmissivity decreases with the vegetation water content.

4.5.3 Transmissivity vs. Tree Density

In this section, we simulate forests of different tree densities to investigate how the tree density effect the transmissivity. The simulations are performed for forest of 5m- and 8m-tall tree using both the V-pol and H-pol plane wave. The tree density varies from 0.07 to 0.15 and the corresponding number of tree ranges from 14 to 30. The microwave transmissivities obtained from the hybrid method and the RTE model are plotted in Fig.4.5.6. The two methods both predict that the H-pol transmission is greater that that of the V-pol. This makes sense as the attenuation is predominantly caused by the vertical tree trunk. The full-wave based transmissivities is significantly greater than those of RTE. This is because the homogenization approximation made in the RTE is only valid for a dense vegetation canopy and is not applicable for forest whose scatterer has a great spatial variation. The effective propagation constant used in RTE to characterize the wave propagation imply that there is constant attenuation in all the space. However, this contradicts to the fact that there is no attenuation in the free space and only the vegetation cause the absorption. The failure of capturing the gap spacing result an underestimation of the microwave transmission. Only the full-wave approach can model the free space propagation as it includes both the amplitude and phase of the wave. The results are consistent with the observations reported in [41, 51] which both state that the L-band microwave is sensitive for the soil moisture over the forested area.

Next, we simulate the trunk only forest to investigate the impact of the branches on the transmissivity. The T-matrix of the trunk only tree are obtained from the ICA approximation. Fig. 4.5.7 plots the t as a function of density for both the trunk only case and the trunk with two type branches

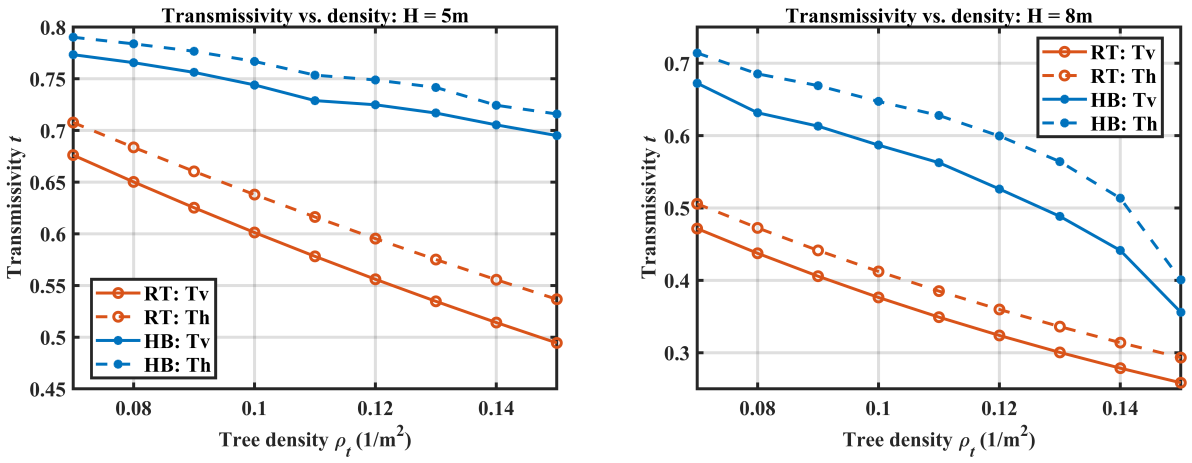

(a) (b)

Figure 4.5.6: The L-band microwave transmissivities change with tree density with tree height of (a) H = 5m and (b) H = 8m.

case. We can see the V-pol transmissivities of the two cases are similar when the tree density is small, they diverge when $\rho_t = 0.14$. At the same time, we can the difference between the H-pol transmissivity is much higher that those of V-pol. This may be due to the fact that most of the branches are horizontally oriented and thus they are less sensitivity to the V-pol plane wave. That is also the reason why the H-pol transmissivity of the trunk only case is much larger than that of the trunk with branches case. This implies that while the H-pol generally has higher transmissivity that V-pol, but there are more sensitivity to the branch scattering.

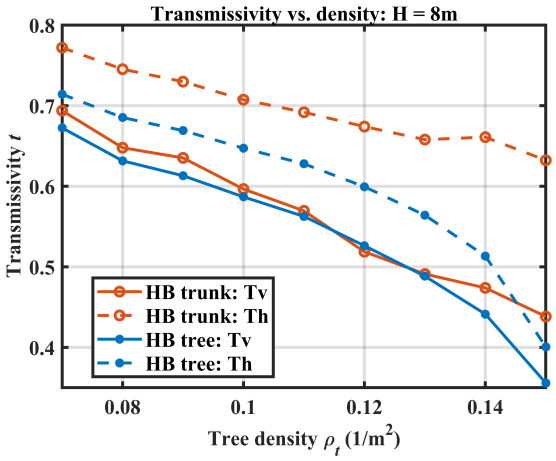

Figure 4.5.7: The L-band microwave transmissivities of eight meters tall forest change with tree density.

4.6 Summary

In this chapter, the hybrid method is applied to perform full-wave simulations of forest at L-band. To overcome the issue in calculating the T-matrix of one tree, the general relation between the T-matrix elements and the plane wave scattered field coefficients is first revealed. Based on that, a Fourier transform based approach is developed for extracting the T-matrix. The new method is more general than the matrix inversion based approach, as the number of the plane wave used in calculating the T-matrix is independent of its size. In addition, the Fourier type transformation enable us to calculate the T-matrix element independently rather than simultaneously. Thus it is applicable for plant of arbitrary size and shape. Following new discovery, a far-field based T-matrix extraction method is developed using the large argument approximation of the Hankel function and the far-field approximation of the free space green's function. The far-field based method is more efficient than the near-field based approach especially when the size of the plant is large, as it does not require the surface integration to obtain the scattered field coefficient. It is also more convenient as the far-field is available in most of the commercial software and can be directly used to calculate the T-matrix. The memory challenge of the hybrid method is successfully resolved by adopting the physical iterative solution for solving the FL equations. The proposed methods are validated with FEKO by comparing the solution of scattering from three eight meters tall trees. Full-wave simulations of forest with different tree density and height are carried out to investigate the potential of retrieving soil moisture in the forest area using L-band microwave.

Appendix

In the following appendices, we provide the key derivations that are critical for the far-field based T-matrix extraction. They are the stationary phase approximation, the cylindrical wave expansion of the free space scalar Green's function, and the plane wave and cylindrical wave transformation for the inner field calculation.

4.A Stationary Phase Approximation

The cylindrical wave form a complete basis and the scalar scattered field can be expressed as

$$E_s(r) = \sum_n \int dk_z a_n^s(k_z) H_n^{(1)}(k_\rho \rho) \exp(ik_z z) \exp(in\phi) \tag{4.45}$$

where $H_n^{(1)}(k_\rho\rho)$ are the Hankel function of first kind representing the outgoing wave and $a_n^s(k_z)$ are corresponding scattered field coefficients. The large argument approximation of $H_n^{(1)}(k_\rho\rho)$ is

$$\lim_{\rho\to\infty} H_n^{(1)}(k_\rho\rho) = \sqrt{\frac{2}{\pi k_\rho \rho}} \exp(ik_\rho\rho) \exp(-i\frac{n}{2}\pi) \exp(-\frac{i\pi}{4}). \tag{4.46}$$

In the far-field region, the scattered field (4.45) can be approximated as

$$\lim_{\rho\to\infty} E_s(r) = \sum_n e^{in\phi} \int dk_z a_n^s(k_z) \sqrt{\frac{2}{\pi k_\rho \rho}} \exp(ik_\rho\rho) \exp\left(-i\frac{n}{2}\pi\right) \exp\left(-\frac{i\pi}{4}\right) \exp(ik_z z) \tag{4.47}$$

The phase term of the integration in (4.46) is

$$f = k_\rho \rho + k_z z = \sqrt{k^2 - k_z^2}\rho + k_z z \tag{4.48}$$

which varies rapidly with k_z when $r = (\rho, z)$ is large. Then the integration over k_z can be calculated using the stationary phase approximation. The stationary point can be found by taking derivative of f over k_z and set it to be 0

$$\frac{df}{dk_z} = -\frac{k_z}{\sqrt{k^2 - k_z^2}}\rho + z = 0 \tag{4.49}$$

Note that $\rho = r\sin\theta,\ z = r\cos\theta$, and substitute them into (4.49), we get

$$-\frac{k_z}{\sqrt{k^2 - k_z^2}} r\sin\theta + r\cos\theta = 0 \tag{4.50}$$

Rearrange and solve for k_z

$$\cos\theta\sqrt{k^2 - k_z^2} \quad = \quad k_z \sin\theta \tag{4.51}$$

Then the stationary point is

$$k_z = k\cos\theta \tag{4.52}$$

With the stationary approximation, the scattered field in the far-field region is simplified as

$$\lim_{\rho\to\infty} E_s(r,\theta,\phi) = \sum_n e^{in\phi} a_n^s (k\cos\theta)\exp(-i\frac{n}{2}\pi)\int dk_z \sqrt{\frac{2}{\pi k_\rho \rho}}\exp(i(k_\rho\rho - \frac{i\pi}{4}))\exp(ik_z z) \tag{4.53}$$

The integration over k_z in (4.53) can be related to plane wave using the cylindrical wave expansion of green's function as shown in the next section.

4.B Cylindrical Wave Expansion of Green's Function

The plane wave expansion of scalar green function is

$$\frac{\exp(ikr)}{4\pi r} = \frac{1}{(2\pi)^3}\iiint dk_x dk_y dk_z \frac{\exp\left(i\bar{k}\cdot\bar{r}\right)}{k_x^2+k_y^2+k_z^2-k^2} \tag{4.54}$$

Using the transformation of $x=\rho\cos\phi, y=\rho\sin\phi$ and $k_x=k_\rho\cos\phi_k, k_y=k_\rho\sin\phi_k$, the phase term becomes

$$\bar{k}\cdot\bar{r} = k_\rho\left(\cos\phi_k x+\sin\phi_k y\right)+k_z z = k_\rho\rho\cos\left(\phi_k-\phi\right)+k_z z \tag{4.55}$$

Then the RHS of (4.54) can be written in a cylindrical form as

$$\int d\bar{k}\frac{\exp\left(i\bar{k}\cdot\bar{r}\right)}{k_x^2+k_y^2+k_z^2-k^2} = \int dk_z\int_0^\infty dk_\rho k_\rho\int_0^{2\pi} d\phi_k \frac{\exp\left(ik_\rho\rho\cos\left(\phi_k-\phi\right)\right)}{k_\rho^2+k_z^2-k^2}\exp\left(ik_z z\right) \tag{4.56}$$

When the order is integer and the Bessel function is

$$J_n(x) = \frac{1}{2\pi}\int_0^{2\pi}\exp i\left(x\sin\tau-n\tau\right)d\tau \tag{4.57}$$

If $n=0$ and let $\tau=\phi_k+\pi/2$, then

$$\sin\left(\phi_k+\pi/2\right) = \sin\phi_k\cos\left(\pi/2\right)+\cos\phi_k\sin\left(\pi/2\right) = \cos\phi_k \tag{4.58}$$

which gives

$$J_0(x) = \frac{1}{2\pi}\int_0^{2\pi}\exp i\left(x\sin\tau\right)d\tau = \frac{1}{2\pi}\int_0^{2\pi}\exp\left(ix\cos\phi_k\right)d\phi_k \tag{4.59}$$

Then the integration over ϕ_k can be simplified as

$$\int_0^{2\pi} d\phi_k \exp\left(ik_\rho \rho \cos\left(\phi_k - \phi\right)\right) = 2\pi J_0\left(k_\rho \rho\right) \tag{4.60}$$

Using (4.60), the integration in (4.56) becomes

$$\int d\bar{k} \frac{\exp\left(i\bar{k}\cdot\bar{r}\right)}{k_x^2 + k_y^2 + k_z^2 - k^2} = 2\pi \int dk_z \exp\left(ik_z z\right) \int_0^\infty dk_\rho k_\rho \frac{J_0\left(k_\rho \rho\right)}{k_\rho^2 + k_z^2 - k^2} \tag{4.61}$$

Note that $H_n^{(1)}\left(x\right) = J_n\left(x\right) + iY_n\left(x\right)$ and $H_n^{(2)}\left(x\right) = J_n\left(x\right) - iY_n\left(x\right)$, then

$$J_0\left(k_\rho \rho\right) = \frac{1}{2}\left[H_0^{(1)}(k_\rho \rho) + H_0^{(2)}\left(k_\rho \rho\right)\right] \tag{4.62}$$

when n is integer, $J_{-n}\left(x\right) = \left(-1\right)^n J_n\left(x\right)$ and $Y_{-n}\left(x\right) = \left(-1\right)^n Y_n\left(x\right)$. Then the integration over k_ρ can be rewritten as

$$\int_0^\infty dk_\rho k_\rho \frac{J_0\left(k_\rho \rho\right)}{k_\rho^2 + k_z^2 - k^2} = \frac{1}{2}\int_0^\infty dk_\rho k_\rho \frac{H_0^{(1)}\left(k_\rho \rho\right)}{k_\rho^2 + k_z^2 - k^2} + \frac{1}{2}\int_0^\infty dk_\rho k_\rho \frac{H_0^{(2)}\left(k_\rho \rho\right)}{k_\rho^2 + k_z^2 - k^2} \tag{4.63}$$

From the reflection formulas of the Hankel function $H_n^{(1)}\left(-z\right) = \left(-1\right)^n H_n^{(2)}\left(z\right)$, we have

$$H_0^{(2)}\left(-k'_\rho \rho\right) = -H_0^{(1)}\left(k'_\rho \rho\right) \tag{4.64}$$

In the second term of (4.63), let $k_\rho = -k'_\rho, dk_\rho = -dk'_\rho$, and using $H_0^{(2)}(-k'_\rho \rho) = -H_0^{(1)}(k'_\rho \rho)$ then

$$\begin{aligned}
& \frac{1}{2}\int_0^\infty dk_\rho k_\rho \frac{H_0^{(2)}\left(k_\rho \rho\right)}{k_\rho^2 + k_z^2 - k^2} \\
= \; & \frac{1}{2}\int_0^{-\infty} dk'_\rho k'_\rho \frac{H_0^{(2)}\left(-k'_\rho \rho\right)}{k_\rho'^2 + k_z^2 - k^2} \;\; \# \; k_\rho = -k'_\rho, dk_\rho = -dk'_\rho \\
= \; & \frac{1}{2}\int_0^{-\infty} dk'_\rho k'_\rho \frac{-H_0^{(1)}\left(k'_\rho \rho\right)}{k_\rho'^2 + k_z^2 - k^2} \;\; \# \; H_0^{(2)}\left(-k'_\rho \rho\right) = -H_0^{(1)}\left(k'_\rho \rho\right)
\end{aligned}$$

So the integration over k_ρ becomes

$$\begin{aligned}\int_0^\infty dk_\rho k_\rho \frac{J_0(k_\rho\rho)}{k_\rho^2+k_z^2-k^2} &= \frac{1}{2}\int_0^\infty dk_\rho k_\rho \frac{H_0^{(1)}(k_\rho\rho)}{k_\rho^2+k_z^2-k^2} + \frac{1}{2}\int_{-\infty}^0 dk_\rho k_\rho \frac{H_0^{(1)}(k_\rho\rho)}{k_\rho^2+k_z^2-k^2} \\ &= \frac{1}{2}\int_{-\infty}^\infty dk_\rho k_\rho \frac{H_0^{(1)}(k_\rho\rho)}{k_\rho^2+k_z^2-k^2}\end{aligned}$$

Note that the denominator is $k_\rho^2-(k^2-k_z^2)$ and the integration kernel is singular when $k_\rho = \pm\sqrt{k^2-k_z^2}$. The singularity can be removed by applying the Cauchy' theorem on the upper plane, which gives

$$\frac{1}{2}\int_{-\infty}^\infty dk_\rho k_\rho \frac{H_0^{(1)}(k_\rho\rho)}{k_\rho^2-(k^2+k_z^2)} = 2\pi i Res\left(k_\rho = \sqrt{k^2-k_z^2}\right) \tag{4.65}$$

where Res is the residue of the integration and is given as $Res(k_{\rho 0}) = f(k_\rho)(k_\rho - k_{\rho 0})$

$$\begin{aligned}Res\left(k_\rho = \sqrt{k^2-k_z^2}\right) &= k_\rho \frac{H_0^{(1)}(k_\rho\rho)}{k_\rho^2-(k^2-k_z^2)}\left(k_\rho - \sqrt{k^2-k_z^2}\right) \\ &= k_\rho \frac{H_0^{(1)}(k_\rho\rho)}{\left(k_\rho+\sqrt{k^2-k_z^2}\right)\left(k_\rho-\sqrt{k^2-k_z^2}\right)}\left(k_\rho - \sqrt{k^2-k_z^2}\right) \\ &= \frac{H_0^{(1)}(k_\rho\rho)}{2}\end{aligned}$$

Then integration over k_ρ can be simplified as

$$\frac{1}{2}\int_0^\infty dk_\rho k_\rho \frac{J_0(k_\rho\rho)}{k_\rho^2+k_z^2-k^2} = \frac{\pi i}{2}H_0^{(1)}(k_\rho\rho) \tag{4.66}$$

By applying all the transformation provided above, we can get the cylindrical wave expansion of scalar green function

$$\begin{aligned}
\frac{\exp(ikr)}{4\pi r} &= \frac{1}{(2\pi)^3}\int d\bar{k}\frac{\exp\left(i\bar{k}\cdot\bar{r}\right)}{k_x^2+k_y^2+k_z^2-k^2} \\
&= \frac{1}{(2\pi)^3}\left[2\pi\int dk_z\exp(ik_z z)\int_0^\infty dk_\rho k_\rho\frac{J_0(k_\rho\rho)}{k_\rho^2+k_z^2-k^2}\right] \\
&= \frac{1}{(2\pi)^3}\left[2\pi\int dk_z\exp(ik_z z)\frac{\pi i}{2}H_0^{(1)}(k_\rho\rho)\right] \\
&= \frac{i}{8\pi}\int dk_z\exp(ik_z z)H_0^{(1)}(k_\rho\rho)
\end{aligned} \tag{4.67}$$

The above derivation gives the cylindrical wave expansion of the scalar green function

$$\frac{\exp(ikr)}{r} = \frac{i}{2}\int dk_z\exp(ik_z z)H_0^{(1)}(k_\rho\rho) \tag{4.68}$$

4.C Cylindrical Wave and Plane Wave Transformation

The solutions of Maxwell equations can be expressed differently in different coordinates. For example, it is convenient to express field in terms of cylindrical wave in cylindrical coordinate. In spherical coordinate, it is better to expressed them in spherical wave. The plane wave is the most common or easiest way to express field in the Cartesian coordinate. A solution of Maxwell equation is the solution that obey the partial differential equation and the corresponding boundary condition. The solution is independent of coordinate, so the field solution in one coordinate can be transformed to the other one, and vice versa. In this section, we derive the transformation of plane wave to cylindrical wave and vice versa.

2D scalar plane wave and scalar cylindrical wave

The scalar wave equation is

$$\left(\nabla^2+k^2\right)\psi(\bar{r}) = 0 \tag{4.69}$$

where the ∇^2 operator are defined differently in different coordinates. In 2D Cartesian coordinate, it becomes

$$\left(\frac{\partial^2}{\partial x^2}+\frac{\partial^2}{\partial y^2}+k^2\right)\psi\left(\bar{r}\right)=0 \tag{4.70}$$

The plane wave solution is known as

$$\psi\left(x,y\right)=\exp\left(ik_x x+ik_y y\right) \tag{4.71}$$

where $k_x=k_\rho\cos\phi_k, k_y=k_\rho\sin\phi_k$ are the wave number in x and y direction, $k_\rho=k\sin\theta_k$ is the wave number in the $\hat{\rho}$ direction, and ϕ_k is the incident direction. The 2D scalar plane wave is defined using one variable ϕ_k. In 2D cylindrical coordinate, the scalar wave equation is

$$\left[\frac{1}{\rho}\frac{\partial}{\partial\rho}\left(\rho\frac{\partial}{\partial\rho}\right)+\frac{1}{\rho^2}\frac{\partial^2}{\partial\phi^2}+k^2\right]\psi\left(\bar{r}\right)=0 \tag{4.72}$$

The wave solution can be expressed in terms of cylindrical wave function

$$\psi\left(\rho,\phi\right)=J_n\left(k\rho\right)\exp\left(in\phi\right) \tag{4.73}$$

The basis function in different coordinates are inter changeable and can be done through the wave transformation. With the transformation of $x=\rho\cos\phi, y=\rho\sin\phi$, we can express the phase term in cylindrical coordinate

$$k_x x+k_y y=k_\rho\rho\left[\cos\phi_k\cos\phi+\sin\phi_k\sin\phi\right]=k_\rho\rho\cos\left(\phi-\phi_k\right) \tag{4.74}$$

The scalar 2D plane wave from ϕ_k can be expressed in cylindrical coordinate as

$$\exp\left(ik_x x+ik_y y\right)=\exp\left(ik_\rho\rho\cos\left(\phi-\phi_k\right)\right) \tag{4.75}$$

which is periodic in ϕ. It can be expressed in terms of Fourier series as

$$\exp\left(ik_\rho \rho \cos\left(\phi - \phi_k\right)\right) = \sum_n c_n \exp\left(in\phi\right) \tag{4.76}$$

where c_n is the Fourier coefficient calculated from

$$c_n = \frac{1}{2\pi}\int_0^{2\pi} f\left(x\right)\exp\left(-in\phi\right)d\phi = \frac{1}{2\pi}\int_0^{2\pi}\exp\left(ik_\rho \rho\cos\left(\phi-\phi_k\right)\right)\exp\left(-in\phi\right)d\phi \tag{4.77}$$

Let $\phi' = \phi - \phi_k, d\phi' = d\phi,\ \phi = \phi' + \phi_k, \phi' \in [0, 2\pi] - \phi_k$, then

$$c_n = \frac{1}{2\pi}\exp\left(-in\phi_k\right)\int_0^{2\pi}\exp\left(ik_\rho\rho\cos\phi'\right)\exp\left(-in\phi'\right)d\phi' \tag{4.78}$$

Note that Bessel function is defined as

$$J_n\left(x\right) = \frac{1}{2\pi}\int_0^{2\pi}\exp\left[i\left(x\sin\tau - n\tau\right)\right]d\tau \tag{4.79}$$

We can let $\phi' = \phi - \frac{\pi}{2}$, then $\cos\phi' = \cos\left(\phi - \frac{\pi}{2}\right) = \sin\phi$ and

$$\int_0^{2\pi}\exp\left(ik_\rho\rho\cos\phi'\right)\exp\left(-in\phi'\right)d\phi' = \exp\left(in\frac{\pi}{2}\right)\int_0^{2\pi}\exp\left(ik_\rho\rho\sin\phi\right)\exp\left(-in\phi\right)d\phi \tag{4.80}$$

Using (4.79), we get

$$\int_0^{2\pi}\exp\left(ik_\rho\rho\cos\phi'\right)\exp\left(-in\phi'\right)d\phi' = 2\pi i^n J_n\left(k_\rho\rho\right) \tag{4.81}$$

Then the coefficient of the Fourier series is related to the cylindrical wave as

$$c_n = \frac{1}{2\pi}\exp\left(-in\phi_k\right)2\pi i^n J_n\left(k_\rho\rho\right) = J_n\left(k_\rho\rho\right)\exp\left(-in\phi_k\right)i^n \tag{4.82}$$

Using the above expression, the plane wave is related to cylindrical wave by using the Fourier transform in $\hat{\phi}$ direction through

$$\exp\left(ik_x x + ik_y y\right) = \sum_n J_n\left(k_\rho \rho\right) \exp\left(-in\phi_k\right) i^n \exp\left(in\phi\right) \tag{4.83}$$

To transform the cylindrical wave to plane wave, we can multiply both sides by $\exp\left(in'\phi_k\right)$ and integrate over ϕ_k, which gives

$$\begin{aligned}
& \int_0^{2\pi} d\phi_k \exp\left(in'\phi_k\right) \exp\left(ik_x x + ik_y y\right) \\
= & \int_0^{2\pi} d\phi_k \exp\left(in'\phi_k\right) \left[\sum_n J_n\left(k_\rho \rho\right) \exp\left(-in\phi_k\right) i^n \exp\left(in\phi\right)\right] \\
= & \sum_n J_n\left(k_\rho \rho\right) \exp\left(in\phi\right) i^n \int_0^{2\pi} d\phi_k \exp\left(in'\phi_k\right) \exp\left(-in\phi_k\right) \\
= & 2\pi J_{n'}\left(k_\rho \rho\right) \exp\left(in'\phi\right) i^{n'} \ \# \, delta \ function
\end{aligned}$$

Rearranging the other term in RHS to LHS, we get

$$J_n\left(k_\rho \rho\right) \exp\left(in\phi\right) = \frac{1}{2\pi} \int_0^{2\pi} d\phi_k \exp\left(in\phi_k\right) i^{-n} \exp\left(ik_x x + ik_y y\right) \tag{4.84}$$

which is the 2D plane wave expansion of 2D cylindrical wave.

In summary, the transformation between 2D scalar cylindrical wave and plane wave is

$$\exp\left(ik_x x + ik_y y\right) = \sum_n \left[J_n\left(k_\rho \rho\right) \exp\left(-in\phi_k\right) i^n\right] \exp\left(in\phi\right) \tag{4.85}$$

$$J_n\left(k_\rho \rho\right) \exp\left(in\phi\right) = \frac{1}{2\pi} \int_0^{2\pi} d\phi_k \exp\left(in\phi_k\right) \left[i^{-n} \exp\left(ik_x x + ik_y y\right)\right] \tag{4.86}$$

Mathematically, the plane wave to cylindrical wave can be interpreted as: the cylindrical wave is the coefficient of the Fourier transform of plane wave in $\hat{\phi}$ direction. On the other hand, the transformation of cylindrical wave to plane wave could be understood as the inverse Fourier transformation of plane wave $\psi\left(\phi_k\right) = \exp\left(ik_x x + ik_y y\right)$ in ϕ_k or the cylindrical wave is the sum of

plane wave form different ϕ_k angle, the plane wave spectrum of the cylindrical wave is

$$F\left(\phi_k\right) = i^{-n} \exp\left(in\phi_k\right) \tag{4.87}$$

3D scalar plane wave and scalar cylindrical wave

In 3D cylindrical coordinate, the scalar wave equation is

$$\left[\frac{1}{\rho}\frac{\partial}{\partial\rho}\left(\rho\frac{\partial}{\partial\rho}\right) + \frac{1}{\rho^2}\frac{\partial^2}{\partial\phi^2} + k^2\right]\psi\left(\bar{r}\right) = 0 \tag{4.88}$$

The 3D scalar incoming and outgoing cylindrical waves are defined as

$$Rg\psi_n\left(k_z, \bar{r}\right) = J_n\left(k_\rho\rho\right)\exp\left(in\phi\right)\exp\left(ik_z z\right) \tag{4.89}$$

$$\psi_n(k_z, \bar{r}) = H_n^{(1)}(k_\rho\rho)\exp(in\phi)\exp(ik_z z) \tag{4.90}$$

where J_n is the Bessel function and $H_n^{(1)}$ is the Hankel function of the first kind with the convention of $\exp\left(ikr\right)$. Using the 2D transformation of cylindrical wave to plane wave (4.84), we have

$$Rg\psi_n\left(k_z, \bar{r}\right) = \frac{1}{2\pi}\int_0^{2\pi} d\phi_k \exp\left(in\phi_k\right) i^{-n} \exp\left(ik_x x + ik_y y + ik_z z\right) \tag{4.91}$$

Then the 3D plane wave is related to the 3D scalar cylindrical wave through

$$\exp\left(ik_x x + ik_y y + ik_z z\right) = \sum_n J_n\left(k_\rho\rho\right)\exp\left(-in\phi_k\right) i^n \exp\left(in\phi\right)\exp\left(ik_z z\right)$$

In summary, the plane wave can be expanded as a Fourier series of $\exp(in\phi_k)$ where ϕ_k is the angle of k in $\hat{\phi}$ direction

$$\exp\left(i\bar{k}\cdot\bar{r}\right) = \sum_n C_n \exp\left(-in\phi_k\right) \tag{4.92}$$

The corresponding coefficient is the 3D cylindrical wave function

$$C_n = J_n\left(k_\rho \rho\right) \exp\left(in\phi\right) \exp\left(ik_z z\right) i^n = Rg\psi_n\left(k_z, \bar{r}\right) i^n \tag{4.93}$$

On the other hand, the cylindrical wave can be expanded in terms of plane wave

$$Rg\psi_n\left(k_z, \bar{r}\right) = \frac{1}{2\pi} \int_0^{2\pi} d\phi_k \exp\left(in\phi_k\right) i^{-n} \exp\left(i\bar{k} \cdot \bar{r}\right) \tag{4.94}$$

The plane wave spectrum of the cylindrical wave is

$$F_n\left(\phi_k\right) = \exp\left(in\phi_k\right) i^{-n} \tag{4.95}$$

3D vector plane wave and vector cylindrical wave

The vector cylindrical wave (VCW) functions are defined as

$$\begin{aligned} Rg\bar{L}_n\left(k_z, \bar{r}\right) &= \nabla Rg\psi_n\left(k_z, \bar{r}\right) & (4.96)\\ Rg\bar{M}_n\left(k_z, \bar{r}\right) &= \nabla \times \left[\hat{z} Rg\psi_n\left(k_z, \bar{r}\right)\right] & (4.97)\\ Rg\bar{N}_n\left(k_z, \bar{r}\right) &= \frac{1}{k} \nabla \times Rg\bar{M}_n\left(k_z, \bar{r}\right) & (4.98) \end{aligned}$$

With the transformation of scalar plane wave to cylindrical wave, we can get

$$\begin{aligned} \nabla \times \left[\hat{z} \exp\left(i\bar{k} \cdot \bar{r}\right)\right] &= \nabla \times \left[\hat{z} \sum_n Rg\psi_n\left(k_z, \bar{\bar{r}}\right) \exp\left(-in\phi_k\right) i^n\right] & (4.99)\\ &= \sum_n \nabla \times \left[\hat{z} Rg\psi_n\left(k_z, \bar{\bar{r}}\right)\right] \exp\left(-in\phi_k\right) i^n & (4.100)\\ &= \sum_n Rg\bar{M}_n\left(k_z, \bar{r}\right) \exp\left(-in\phi_k\right) i^n & (4.101) \end{aligned}$$

which relates the vector plane wave (VPW) to the VCW. Note that $\nabla \times (\bar{a}\phi) = \nabla\phi \times \bar{a} + \phi\nabla \times \bar{a}$, then the LHS of (4.99) is

$$\nabla \times \left[\hat{z} \exp\left(i\bar{k} \cdot \bar{r}\right)\right] = \nabla \exp\left(i\bar{k} \cdot \bar{r}\right) \times \hat{z} = \exp\left(i\bar{k} \cdot \bar{r}\right) i\bar{k} \times \hat{z} \tag{4.102}$$

The horizontal polarization is defined as

$$\hat{h} = \frac{\hat{z} \times \hat{k}}{\left|\hat{z} \times \hat{k}\right|} = \frac{1}{\sin\theta_k} \hat{z} \times \hat{k}$$

Then $\hat{k} \times \hat{z} = -\hat{h} \sin\theta_k$, so the LHS is

$$\nabla \times \left[\hat{z} \exp\left(i\bar{k} \cdot \bar{r}\right)\right] = -\exp\left(i\bar{k} \cdot \bar{r}\right) ik \sin\theta_k \hat{h} \tag{4.103}$$

Equaling the two equations of (4.99) and (4.103), we obtain

$$\exp\left(i\bar{k} \cdot \bar{r}\right) \hat{h}\left(\theta_k, \phi_k\right) = \frac{i}{k_\rho} \sum_n R g \bar{M}_n\left(k_z, \bar{r}\right) \exp\left(-in\phi_k\right) i^n \tag{4.104}$$

which relates the H-pol plane wave to VCW. Take curl of both side of (4.104), we can get the V-pol plane wave

$$LHS = \nabla \times \left[\exp\left(i\bar{k} \cdot \bar{r}\right) \hat{h}\right] = \exp\left(i\bar{k} \cdot \bar{r}\right) i\bar{k} \times \hat{h} = -ik\hat{v} \exp\left(i\bar{k} \cdot \bar{r}\right) \tag{4.105}$$

where $\hat{v} = \hat{h} \times \hat{k}$ is used in the third step and the triplet $\left(\hat{v}, \hat{h}, \hat{k}\right)$ form a orthonormal unit system. The corresponding RHS is

$$\begin{aligned} RHS &= \frac{i}{k_\rho} \sum_n \nabla \times R g \bar{M}_n\left(k_z, \bar{r}\right) \exp\left(-in\phi_k\right) i^n & (4.106) \\ &= \frac{i}{k_\rho} \sum_n kR g \bar{N}_n\left(k_z, \bar{r}\right) \exp\left(-in\phi_k\right) i^n & (4.107) \end{aligned}$$

Then VCW expansions of the V-pol plane wave is

$$\exp\left(i\bar{k}\cdot\bar{r}\right)\hat{v}\left(\theta_k,\phi_k\right)=-\frac{1}{k_\rho}\sum_n RgN_n\left(k_z,\bar{r}\right)\exp\left(-in\phi_k\right)i^n \tag{4.108}$$

The two equations (4.104) and (4.108) transform the VPW to VCW.

The transformation of VPW to VCW can be considered as taking the Fourier transformation of plane wave in the ϕ_k direction.

$$\exp\left(i\bar{k}\cdot\bar{r}\right)\hat{h}\left(\theta_k,\phi_k\right) = \sum_n C_n^h\exp\left(-in\phi_k\right),\ C_n^h=\frac{i^{n+1}}{k_\rho}RgM_n\left(k_z,\bar{r}\right) \tag{4.109}$$

$$\exp\left(i\bar{k}\cdot\bar{r}\right)\hat{v}\left(\theta_k,\phi_k\right) = \sum_n C_n^v\exp\left(-in\phi_k\right),\ C_n^v=\frac{i^{n+2}}{k_\rho}RgN_n\left(k_z,\bar{r}\right) \tag{4.110}$$

The Fourier coefficients are the VCW which are the function of θ_k, n and r. and they are independent of ϕ_k. To transform the VCW back to VPW, we can multiply both side $\exp\left(in'\phi_k\right)$ and integrate ϕ_k

$$\int d\phi_k\exp\left(in'\phi_k\right)\exp\left(i\bar{k}\cdot\bar{r}\right)\hat{h}=\frac{i}{k_\rho}\sum_n RgM_n\left(k_z,\bar{r}\right)\int d\phi_k\exp\left(in'\phi_k\right)\exp\left(-in\phi_k\right)i^n \tag{4.111}$$

$$\int d\phi_k\exp\left(in'\phi_k\right)\exp\left(i\bar{k}\cdot\bar{r}\right)\hat{v}=-\frac{1}{k_\rho}\sum_n RgN_n\left(k_z,\bar{r}\right)\int d\phi_k\exp\left(in'\phi_k\right)\exp\left(-in\phi_k\right)i^n \tag{4.112}$$

With the orthogonality of the $\exp\left(in\phi_k\right)$

$$\int d\phi_k\exp\left(in'\phi_k\right)\exp\left(-in\phi_k\right)=2\pi\delta_{nn'} \tag{4.113}$$

The transformation of VCW to VPW is obatained as

$$RgM_n\left(k_z,\bar{r}\right) = \frac{k_\rho}{2\pi i^{n+1}}\int d\phi_k\exp\left(in\phi_k\right)\exp\left(i\bar{k}\cdot\bar{r}\right)\hat{h}\left(\theta_k,\phi_k\right) \tag{4.114}$$

$$RgN_n\left(k_z,\bar{r}\right) = \frac{k_\rho}{2\pi i^{n+2}}\int d\phi_k\exp\left(in\phi_k\right)\exp\left(i\bar{k}\cdot\bar{r}\right)\hat{v}\left(\theta_k,\phi_k\right) \tag{4.115}$$

where $k_\rho = k\sin\theta_k, k_z = k\cos\theta_k$ and $\hat{v}\left(\theta_k,\phi_k\right)$ and $\hat{h}\left(\theta_k,\phi_k\right)$ are vertical and horizontal polarizations

$$\widehat{k}\left(\theta_k,\phi_k\right) = \sin\theta_k\cos\phi_k\widehat{x} + \sin\theta_k\sin\phi_k\widehat{y} + \cos\theta_k\widehat{z} \tag{4.116}$$

$$\widehat{v}\left(\theta_k,\phi_k\right) = \cos\theta_k\cos\phi_k\widehat{x} + \cos\theta_k\sin\phi_k\widehat{y} - \sin\theta_k\widehat{z} \tag{4.117}$$

$$\widehat{h}\left(\theta_k,\phi_k\right) = -\sin\phi_k\widehat{x} + \cos\phi_k\widehat{y} \tag{4.118}$$

If the center of the cylindrical wave is at $\bar{r}_q$, then

$$Rg\overline{M}_n\left(k_z,\overline{rr_q}\right) = \frac{k\sin\theta_k}{2\pi i^{n+1}}\int_0^{2\pi} d\phi_k \exp\left(in\phi_k\right)\widehat{h}\left(\theta_k,\phi_k\right)\exp\left(i\overline{k}\cdot\left(\overline{r}-\overline{r}_q\right)\right) \tag{4.119}$$

$$Rg\overline{N}_n\left(k_z,\overline{rr_q}\right) = \frac{k\sin\theta_k}{2\pi i^{n+2}}\int_0^{2\pi} d\phi_k \exp\left(in\phi_k\right)\widehat{v}\left(\theta_k,\phi_k\right)\exp\left(i\overline{k}\cdot\left(\overline{r}-\overline{r}_q\right)\right) \tag{4.120}$$

Given θ_k, the VCW can be expressed as plant waves from many different ϕ_k.

In summary, the transfomation between the 3D VPW and the 3D VCW are

$$\exp\left(i\bar{k}\cdot\bar{r}\right)\hat{v}\left(\theta_k,\phi_k\right) = \sum_n \frac{i^{n+1}}{k_\rho} Rg\bar{M}_n\left(k_z,\bar{r}\right)\exp\left(-in\phi_k\right) \tag{4.121}$$

$$\exp\left(i\bar{k}\cdot\bar{r}\right)\hat{h}\left(\theta_k,\phi_k\right) = \sum_n \frac{i^{n+2}}{k_\rho} Rg\bar{N}_n\left(k_z,\bar{r}\right)\exp\left(-in\phi_k\right) \tag{4.122}$$

$$Rg\bar{M}_n\left(k_z,\bar{r}\right) = \frac{k_\rho}{2\pi i^{n+1}}\int d\phi_k \exp\left(in\phi_k\right)\exp\left(i\bar{k}\cdot\bar{r}\right)\hat{h}\left(\theta_k,\phi_k\right) \tag{4.123}$$

$$Rg\bar{N}_n\left(k_z,\bar{r}\right) = \frac{k_\rho}{2\pi i^{n+2}}\int d\phi_k \exp\left(in\phi_k\right)\exp\left(i\bar{k}\cdot\bar{r}\right)\hat{v}\left(\theta_k,\phi_k\right) \tag{4.124}$$

CHAPTER 5

Conclusion

5.1 Summary

In this dissertation, a two-step hybrid method is developed for full-wave simulation of vegetation driven by the need of microwave remote sensing of soil moisture. The full-wave based simulation significantly improve the accuracy of modeling wave propagation in vegetation as it considers both the phase and the amplitude of the electromagnetic field. Therefore, the hybrid method is able to capture the multiple scattering caused by the plant structure and the gap spacing among different plants. The microwave transmissivity predicted by the hybrid method is significantly higher than those obtained from the classical radiative transfer model (RTE), which is consistent with measurement data reported in [41, 42]. This indicates that (1) it is potential to use the L-band signal to retrieve soil moisture over forested area or area with large vegetation water content, and (2) the higher frequency channel such as S- and C-band can also be utilized to retrieve the Earth information.

The hybrid method is built based on a realistic vegetation field that can model both the plant structures and gap spacing among different plants within the vegetation layer. Based on that, the full-wave simulation of a large vegetation field is performed using the hybrid method in two steps. In the first step, the full-wave simulations of one single plant are performed using the numerical solver from which the corresponding single plant T-matrix is calculated. The employment of the numerical solver significantly expand the modeling capability as it enables the hybrid method

to simulate plant of arbitrary shapes which is not feasible by the analytical method. The full-wave based T-matrix characterize the scattering of one single plant using the vector cylindrical wave (VCW) expansions and captures the multiple scattering due to the plant structures. In the second step, the multiple scattering among different plants are considered analytically using the T-matrix and the Foldy-Lax multiple equations. With the translational addition theorem and the VCW expansions, a closed-from equation are obtained for solving the final scattered field. The employment of the analytical solution enable the hybrid method to simulate a large vegetation field which is otherwise impossible to be solved using the numerical method. The wave multiple scattering approach includes both the phase and amplitude of the field and thus is able to capture the gap spacing amount different plants. The combination of the numerical and analytical method has made the full-wave simulation of a large vegetation field be possible for the first time. The work presented in each chapter is summarized as follows.

In Chapter 2, the detailed derivation of the near-field based T-matrix extraction method and the FLE multiple scattering equations are presented. The full-wave simulations of one single wheat plant are performed using a FEM based numerical solver HFSS. The corresponding single wheat T-matrix is then calculated based on the near-field using the Huygens principle and the VCW expansions of the Dyadic Green's function. The hybrid method is validated with HFSS by solving scattering from 4 wheat plants.

In Chapter 3, the hybrid method is applied to perform full-wave simulation of wheat field at L-, S-, and C-band. A physical iterative method for Monte Carlo simulations is developed and implemented with MPI to meet the large memory demand required at the higher frequency. The impact of the plant structure and the gap spacing on the microwave transmissivity are demonstrated by comparing transmission at different regions. The simulation results show that the attenuation caused by the vegetation layer will saturate as the frequency increases and the corresponding frequency dependence is much weaker than that predicted by the RTE model. The results suggest that the S- and C-bands measurements could be used to support L-band surface parameter retrieval algorithms, such as soil moisture.

In Chapter 4, the hybrid method is applied to perform full-wave simulation of forest at L-band. A general relation is first discovered showing that T-matrix is the coefficient of the Fourier series of the scattered field coefficient. Based on that, a far-field based approach applicable for scatterer of arbitrary shape and size is developed for calculating the T-matrix of one single tree. The dependencies of the solutions on tree heights and tree densities are illustrated. The results show that the full-wave based transmissivities are much larger than those obtained from the RTE model suggesting that it is possible to retrieve soil moisture over the forested area.

5.2 Future Works

Despite the advancements that have been made in this dissertation, we are still in the early stage of performing the full-wave simulation of vegetation. There are addition works can be done to further improve the hybrid method. First, we can include the evanescent waves in the T-matrix so that it is also applicable for scenarios when the evanescent waves are dominant in the multiple scattering process. In order to extract T-matrix with evanescent waves, the dipole source rather than the plane wave excitation should be used in the full-wave simulations. Only the near-field based approach can be applied to calculate the coefficient of the evanescent waves as they do not exist in the far-field. Second, as limited by the capability of the numerical solver, we are currently unable to simulate a whole realistic tree that including all the small branches and leaves. One possible solution is to decompose the tree into many components. For instance, a tree can be modeled as one component of trunk with primary branches pluses multiple components of small branches with leaves. Then the total T-matrix of one single tree is approximated as the coherent addition of the T-matrices of all the components. The advantage of this solution is that it considers the scattering of the leaves and branches. The trade off is the multiple scattering between different components are ignored. Third, the solution of the Foldy-Lax equations can be further speed up using the Fast Fourier Transform (FFT). The idea is to use the indirect transformation to realize the interaction between the scatterers based on the intermediate canonical grid point. For example,

the interaction between plant p and q can be accomplished by first transforming the cylindrical wave centered at r_q to the nearest canonical grid point $r_q o$. Then transform them to the grid point $r_p 0$ that closest to the target plant r_p. Finally, transform them from $r_p o$ to r_p. The transformation between the 2D canonical grids can be speed up using the 2D FFT. The transformation between the cylindrical wave order can also speed up using 1D FFT. Fourth, the hybrid method can be applied to study corn field, wheat fields, and soybean etc. with realistic structures and field setup. The full-wave based results can be compared with the classical RTE model to investigate importance of the phase information in the the multiple scattering process. The results can also be compared with the SMAPVEX data to improve the accuracy of soil moisture retrieval.

5.3 Contributions

The worked presented in this dissertation has been published or submitted in the following journal and conference papers.

5.3.1 Journal Papers

1. **W. Gu**, L. Tsang, A. Colliander, and S.H. Yueh, "Hybrid Method for Full-wave Simulations of Forests at L-band", submitted, IEEE Access, 2022.

2. L. Tsang, T.H. Liao, R. Gao, H. Xu, **W. Gu**, and J. Zhu, "Theory of Microwave Remote Sensing of Vegetation Effects,SoOP and Rough Soil surface backscattering," Remote Sensing, vol. 14, no. 15, p. 3640, 2022.

3. **W. Gu**, L. Tsang, A. Colliander, and S.H. Yueh, "Multifrequency Full-wave Simulations of Vegetation using A Hybrid Method," IEEE Transactions on Microwave Theory and Techniques, vol. 70, no. 1, pp. 275–285, 2021.

4. **W. Gu**, L. Tsang, A. Colliander, and S.H. Yueh, "Wave Propagation in Vegetation Field Using a Hybrid Method," IEEE Transactions on Antennas and Propagation, vol. 69, no. 10,

pp. 6752–6761, 2021.

5. **W. Gu**, H. Xu, and L. Tsang, "A Numerical Kirchhoff Simulator for GNSS-R Land Applications," Progress in electromagnetics research, vol. 164, pp. 119–133, 2019.

5.3.2 Conference Papers

1. **W. Gu** and L. Tsang, "Multi-frequencies Full-wave Simulations of Wave Propagation in Vegetation for Remote Sensing of Soil Moisture," in 2021 IEEE International Symposium on Antennas and Propagation and USNC-URSI Radio Science Meeting (APS/URSI). IEEE, 2021, pp. 1113–1114.

2. **W. Gu**, L. Tsang, A. Colliander, and S. Yueh, "Multi-frequency NMM3D Simulations of Wave Propagation in Vegetation for Remote Sensing of Soil Moisture," in 2021 IEEE International Geoscience and Remote Sensing Symposium IGARSS. IEEE, 2021, pp. 3534–3536.

3. **W. Gu** and L. Tsang, "Vegetation Effects for Remote Sensing of Soil Moisture Using NMM3D Full-wave Simulation," in 2020 IEEE International Symposium on Antennas and Propagation and North American Radio Science Meeting. IEEE, 2020, pp. 1095–1096.

4. **W. Gu**, L. Tsang, A. Colliander, and S. Yueh, "Full-wave Simulations of Scattering in Vegetation for Microwave Remote Sensing of Soil Moisture," in IGARSS 2020-2020 IEEE International Geoscience and Remote Sensing Symposium. IEEE, 2020, pp. 4704–4706.

5. J. Zhu, L. Tsang, H. Xu, and **W. Gu**, "A Patch Model Based on Numerical Solutions of Maxwell Equations for GNSS-R Land Applications," in IGARSS 2019-2019 IEEE International Geoscience and Remote Sensing Symposium. IEEE, 2019, pp. 8719–8721.

Bibliography

[1] Water Science School, "A comprehensive study of the natural water cycle," *https://www.usgs.gov/special-topics/water-science-school*, 2019.

[2] Y. H. Kerr, P. Waldteufel, J.-P. Wigneron, J. Martinuzzi, J. Font, and M. Berger, "Soil moisture retrieval from space: The soil moisture and ocean salinity (smos) mission," *IEEE transactions on Geoscience and remote sensing*, vol. 39, no. 8, pp. 1729–1735, 2001.

[3] F. T. Ulaby, D. G. Long, W. J. Blackwell, C. Elachi, A. K. Fung, C. Ruf, K. Sarabandi, H. A. Zebker, and J. Van Zyl, *Microwave radar and radiometric remote sensing*. University of Michigan Press Ann Arbor, MI, USA, 2014, vol. 4, no. 5.

[4] Y. H. Kerr, "Soil moisture from space: Where are we?" *Hydrogeology journal*, vol. 15, no. 1, pp. 117–120, 2007.

[5] H. M. Barré, B. Duesmann, and Y. H. Kerr, "Smos: The mission and the system," *IEEE transactions on geoscience and remote sensing*, vol. 46, no. 3, pp. 587–593, 2008.

[6] D. Entekhabi, E. G. Njoku, P. E. O'Neill, K. H. Kellogg, W. T. Crow, W. N. Edelstein, J. K. Entin, S. D. Goodman, T. J. Jackson, J. Johnson, J. Kimball, J. R. Piepmeier, R. D. Koster, N. Martin, K. C. McDonald, M. Moghaddam, S. Moran, R. Reichle, J. C. Shi, M. W. Spencer, S. W. Thurman, L. Tsang, and J. Van Zyl, "The soil moisture active passive (smap) mission," *Proceedings of the IEEE*, vol. 98, no. 5, pp. 704–716, 2010.

[7] A. Merzouki, H. McNairn, and A. Pacheco, "Mapping soil moisture using radarsat-2 data and local autocorrelation statistics," *IEEE Journal of Selected Topics in Applied Earth Observations and Remote Sensing*, vol. 4, no. 1, pp. 128–137, 2011.

[8] E. G. Njoku, T. J. Jackson, V. Lakshmi, T. K. Chan, and S. V. Nghiem, "Soil moisture retrieval from amsr-e," *IEEE transactions on Geoscience and remote sensing*, vol. 41, no. 2, pp. 215–229, 2003.

[9] K. Kellogg, P. Hoffman, S. Standley, S. Shaffer, P. Rosen, W. Edelstein, C. Dunn, C. Baker, P. Barela, Y. Shen, A. M. Guerrero, P. Xaypraseuth, V. R. Sagi, C. V. Sreekantha, N. Harinath, R. Kumar, R. Bhan, and C. V. H. S. Sarma, "Nasa-isro synthetic aperture radar (nisar) mission," in *2020 IEEE Aerospace Conference*, 2020, pp. 1–21.

[10] L. Kilic, C. Prigent, F. Aires, J. Boutin, G. Heygster, R. T. Tonboe, H. Roquet, C. Jimenez, and C. Donlon, "Expected performances of the copernicus imaging microwave radiometer (cimr)

for an all-weather and high spatial resolution estimation of ocean and sea ice parameters," *Journal of Geophysical Research: Oceans*, vol. 123, no. 10, pp. 7564–7580, 2018.

[11] R. D. De Roo, Y. Du, F. T. Ulaby, and M. C. Dobson, "A semi-empirical backscattering model at l-band and c-band for a soybean canopy with soil moisture inversion," *IEEE Transactions on Geoscience and Remote Sensing*, vol. 39, no. 4, pp. 864–872, 2001.

[12] L. L. Foldy, "The multiple scattering of waves. i. general theory of isotropic scattering by randomly distributed scatterers," *Physical review*, vol. 67, no. 3-4, p. 107, 1945.

[13] L. Tsang, M. C. Kubacsi, and J. A. Kong, "Radiative transfer theory for active remote sensing of a layer of small ellipsoidal scatterers," *Radio Science*, vol. 16, no. 03, pp. 321–329, 1981.

[14] R. H. Lang and J. S. Sidhu, "Electromagnetic backscattering from a layer of vegetation: A discrete approach," *IEEE Transactions on Geoscience and Remote Sensing*, vol. GE-21, no. 1, pp. 62–71, 1983.

[15] A. H. Sihvola, *Electromagnetic mixing formulas and applications*. Iet, 1999, no. 47.

[16] A. Ishimaru, *Electromagnetic wave propagation, radiation, and scattering: from fundamentals to applications*. John Wiley & Sons, 2017.

[17] L. Tsang, J. A. Kong, K. Ding, and C. Ao, *Scattering of electromagnetic waves: numerical simulations*. John Wiley & Sons, 2004, vol. 25.

[18] A. Schuster, "Radiation through a foggy atmosphere," *The astrophysical journal*, vol. 21, p. 1, 1905.

[19] S. H. Yueh, J. A. Kong, J. K. Jao, R. T. Shin, and T. Le Toan, "Branching model for vegetation," *IEEE Transactions on Geoscience and Remote Sensing*, vol. 30, no. 2, pp. 390–402, 1992.

[20] H. Huang, S. Kim, L. Tsang, X. Xu, T. Liao, T. J. Jackson, and S. H. Yueh, "Coherent model of l-band radar scattering by soybean plants: Model development, evaluation, and retrieval," *IEEE Journal of Selected Topics in Applied Earth Observations and Remote Sensing*, vol. 9, no. 1, pp. 272–284, 2016.

[21] G. Zhang, L. Tsang, and Z. Chen, "Collective scattering effects of trees generated by stochastic lindenmayer systems," *Microwave and Optical Technology Letters*, vol. 11, no. 2, pp. 107–111, 1996.

[22] Y. C. Lin and K. Sarabandi, "A monte carlo coherent scattering model for forest canopies using fractal-generated trees," *IEEE Transactions on Geoscience and Remote Sensing*, vol. 37, no. 1, pp. 440–451, 1999.

[23] T. Liao, S. Kim, S. Tan, L. Tsang, C. Su, and T. J. Jackson, "Multiple scattering effects with cyclical correction in active remote sensing of vegetated surface using vector radiative transfer theory," *IEEE Journal of Selected Topics in Applied Earth Observations and Remote Sensing*, vol. 9, no. 4, pp. 1414–1429, 2016.

[24] Y. Oh, Y. M. Jang, and K. Sarabandi, "Full-wave analysis of microwave scattering from short vegetation: an investigation on the effect of multiple scattering," *IEEE Transactions on Geoscience and Remote Sensing*, vol. 40, no. 11, pp. 2522–2526, 2002.

[25] Y. Oh and J. Hong, "Moment method/monte carlo simulation of the microwave backscatter of wet-land rice fields," in *2007 IEEE International Geoscience and Remote Sensing Symposium*. IEEE, 2007, pp. 69–72.

[26] F. Montomoli, G. Macelloni, M. Brogioni, and A. Toccafondi, "Investigation on the validity region of analytical models simulating scattering from vegetation elements," in *2012 IEEE International Geoscience and Remote Sensing Symposium*. IEEE, 2012, pp. 5161–5164.

[27] D. Liao, "On the validity of an analytical solution for characterizing backscattering from tree trunks for fopen sensing at p -band," *IEEE Transactions on Antennas and Propagation*, vol. 65, no. 10, pp. 5639–5644, 2017.

[28] H. Huang, L. Tsang, E. G. Njoku, A. Colliander, T. Liao, and K. Ding, "Propagation and scattering by a layer of randomly distributed dielectric cylinders using monte carlo simulations of 3d maxwell equations with applications in microwave interactions with vegetation," *IEEE Access*, vol. 5, pp. 11 985–12 003, 2017.

[29] H. Huang, L. Tsang, A. Colliander, and S. H. Yueh, "Propagation of waves in randomly distributed cylinders using three-dimensional vector cylindrical wave expansions in foldy–lax equations," *IEEE Journal on Multiscale and Multiphysics Computational Techniques*, vol. 4, pp. 214–226, Dec 2019.

[30] A. K. Fung, "Scattering from a vegetation layer," *IEEE Transactions on Geoscience Electronics*, vol. 17, no. 1, pp. 1–6, 1979.

[31] U. F. T., K. Sarabandi, K. Mcdonald, M. Whitt, and M. C. Dobson, "Michigan microwave canopy scattering model," *International Journal of Remote Sensing*, vol. 11, no. 7, pp. 1223–1253, 1990.

[32] D. R. Brunfeldt and F. T. Ulaby, "Microwave emission from row crops," *IEEE Transactions on Geoscience and Remote Sensing*, vol. GE-24, no. 3, pp. 353–359, 1986.

[33] K. Sarabandi, A. Tavakoli, and F. T. Ulaby, "Propagation in a two-dimensional periodic random medium with inhomogeneous particle distribution," *IEEE Transactions on Antennas and Propagation*, vol. 40, no. 10, pp. 1175–1186, 1992.

[34] A. Tavakoli, K. Sarabandi, and F. Ulaby, "Horizontal propagation through periodic vegetation canopies," *IEEE Transactions on antennas and propagation*, vol. 39, no. 7, pp. 1014–1023, 1991.

[35] N. R. Leonor, R. F. S. Caldeirinha, T. R. Fernandes, J. Richter, and M. Al-Nuaimi, "A discrete ret model for millimeter-wave propagation through vegetation," *IEEE Transactions on Antennas and Propagation*, vol. 66, no. 4, pp. 1985–1998, 2018.

[36] C. Utku and R. Lang, "Effective scatterer approximation for mean field modeling with application to vegetation," *Waves in Random and Complex Media*, vol. 18, no. 1, pp. 65–90, 2008.

[37] L. Tsang, J. A. Kong, and K. Ding, *Scattering of electromagnetic waves: theories and applications*. John Wiley & Sons, 2004, vol. 27.

[38] E. G. Njoku, T. J. Jackson, V. Lakshmi, T. K. Chan, and S. V. Nghiem, "Soil moisture retrieval from amsr-e," *IEEE Transactions on Geoscience and Remote Sensing*, vol. 41, no. 2, pp. 215–229, 2003.

[39] U. Narayan, V. Lakshmi, and E. G. Njoku, "Retrieval of soil moisture from passive and active l/s band sensor (pals) observations during the soil moisture experiment in 2002 (smex02)," *Remote Sensing of Environment*, vol. 92, no. 4, pp. 483–496, 2004.

[40] W. Gu, L. Tsang, A. Colliander, and S. H. Yueh, "Wave propagation in vegetation field using a hybrid method," *IEEE Transactions on Antennas and Propagation*, vol. 69, no. 10, pp. 6752–6761, 2021.

[41] A. Colliander, M. H. Cosh, V. R. Kelly, S. Kraatz, L. Bourgeau-Chavez, P. Siqueira, A. Roy, A. Konings, N. Holtzman, S. Misra *et al.*, "Smap detects soil moisture under temperate forest canopies," *Geophysical Research Letters*, vol. 47, no. 19, p. e2020GL089697, 2020.

[42] E. Ayres, A. Colliander, M. Cosh, J. Roberti, S. Simkin, and M. Genazzio, "Validation of smap soil moisture at terrestrial national ecological observatory network (neon) sites show potential for soil moisture retrieval in forested areas," *IEEE Journal of Selected Topics in Applied Earth Observations and Remote Sensing*, vol. 14, pp. 10 903–10 918, 2021.

[43] L. Tsang, T.-H. Liao, R. Gao, H. Xu, W. Gu, and J. Zhu, "Theory of microwave remote sensing of vegetation effects, soop and rough soil surface backscattering," *Remote Sensing*, vol. 14, no. 15, p. 3640, 2022.

[44] W. Gu, H. Xu, and L. Tsang, "A numerical kirchhoff simulator for gnss-r land applications," *Progress in electromagnetics research*, vol. 164, pp. 119–133, 2019.

[45] W. Gu and L. Tsang, "Vegetation effects for remote sensing of soil moisture using nmm3d full-wave simulation," in *2020 IEEE International Symposium on Antennas and Propagation and North American Radio Science Meeting*. IEEE, 2020, pp. 1095–1096.

[46] W. Gu and L. Tsang, "Multi-frequencies full-wave simulations of wave propagation in vegetation for remote sensing of soil moisture," in *2021 IEEE International Symposium on Antennas and Propagation and USNC-URSI Radio Science Meeting (APS/URSI)*. IEEE, 2021, pp. 1113–1114.

[47] W. Gu, L. Tsang, A. Colliander, and S. Yueh, "Full-wave simulations of scattering in vegetation for microwave remote sensing of soil moisture," in *IGARSS 2020-2020 IEEE International Geoscience and Remote Sensing Symposium*. IEEE, 2020, pp. 4704–4706.

[48] W. Gu, L. Tsang, A. Colliander, and S. Yueh, "Multi-frequency nmm3d simulations of wave propagation in vegetation for remote sensing of soil moisture," in *2021 IEEE International Geoscience and Remote Sensing Symposium IGARSS*. IEEE, 2021, pp. 3534–3536.

[49] J. Zhu, L. Tsang, H. Xu, and W. Gu, "A patch model based on numerical solutions of maxwell equations for gnss-r land applications," in *IGARSS 2019-2019 IEEE International Geoscience and Remote Sensing Symposium*. IEEE, 2019, pp. 8719–8721.

[50] P. Waterman, "New formulation of acoustic scattering," *The journal of the acoustical society of America*, vol. 45, no. 6, pp. 1417–1429, 1969.

[51] C. Vittucci, P. Ferrazzoli, Y. Kerr, P. Richaume, L. Guerriero, R. Rahmoune, and V. Laurin, "Smos retrieval over forests: Exploitation of optical depth and tests of soil moisture estimates," *Remote sensing of environment*, vol. 180, pp. 115–127, 2016.